



**University of Ferrara**

---

ENGINEERING DEPARTMENT

Doctoral research course in Engineering Science - XXIX Cycle

Coordinator: **Prof. Stefano Trillo**

**SOUND RADIATION AND SOUND TRANSMISSION IN  
BUILDING STRUCTURES: NUMERICAL MODELLING AND  
EXPERIMENTAL VALIDATION**

Candidate:

**Andrea Santoni**

Doctoral Advisor:

**Prof. Patrizio Fausti**

Co-advisor:

**Dr. Stefan Schoenwald**

---

**Years 2014–2016**

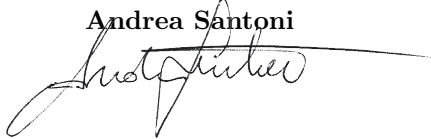
# SOUND RADIATION AND SOUND TRANSMISSION IN BUILDING STRUCTURES: NUMERICAL MODELLING AND EXPERIMENTAL VALIDATION

Years 2014–2016

DISSERTATION SUBMITTED TO THE ENGINEERING DEPARTMENT OF THE UNIVERSITY OF  
FERRARA IN PARTIAL FULFILMENT OF THE REQUIREMENTS FOR THE DEGREE OF  
DOCTOR OF PHILOSOPHY IN ENGINEERING

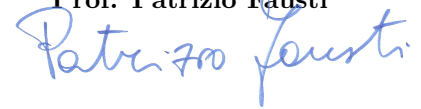
Candidate:

**Andrea Santoni**



Doctoral Advisor:

**Prof. Patrizio Fausti**



Co-advisor:

**Dr. Stefan Schoenwald**



Dissertation evaluated and approved for the Public Defense by referees:

**Prof. John Laurence Davy**

RMIT University Melbourne, Australia

**Prof. Dr. Ulrich Schanda**

Rosenheim University of Applied Sciences, Germany

**Dr. Bart Van Damme**

Empa - Swiss Federal Laboratories for Material Science  
and Technology, Switzerland

# Abstract

The research activities undertaken during these three years have been mainly focused on the investigation of sound radiation and sound transmission in building elements, in order to develop efficient and reliable models, that may represent helpful tools during the design process. Prediction methods represent a valuable resource to acoustician, engineers, and architects, to optimize the acoustic performance of building elements, in order to accomplish a good acoustic comfort inside living spaces. A particular attention has been paid to the input data necessary to implement these models, developing procedures for their experimental determination, and numerical approximation.

The radiation efficiency is an important acoustic descriptor, frequency dependent, that characterises the capability of a vibrating structure to radiate sound, and it is required as input data in many prediction models. Its computation within the building acoustic frequency range – 50 – 5000 Hz – by using boundary element or finite element methods would require a huge computational effort. While several analytical or approximated formulations have been proposed, by different authors, to evaluate the radiation efficiency of isotropic elements, orthotropic structures have not been investigated as thoroughly. In this dissertation different models specifically developed to evaluate the radiation efficiency of orthotropic building structures, such as cross-laminated timber (CLT) plates, are presented. They are based on different assumptions, and allow for a wide range accuracy within the investigated frequency range. Even though CLT panels' dynamics is sometimes investigated by using high order theories, like in structural analysis for example, in the vibro-acoustic investigations presented in this dissertation, they have been treated as thin orthotropic plates, under the assumption of small displacements. The nature of the external excitation strongly influences the radiation behaviour, therefore either a mechanical force or an incident sound field have been considered acting on the plate surface. Reliable input data, necessary to implement the proposed models, are of fundamental importance to obtain accurate results. A non-destructive experimental procedure, based on wave analysis, has been developed, in order to evaluate the direction dependent dynamic stiffness properties of orthotropic structures. The prediction models for orthotropic panels are finally validated with the experimental radiation efficiency evaluated for a CLT plate.

---

A standard procedure to experimentally determine the radiation efficiency of a structure is not currently available. Since this acoustic descriptor is not directly measurable, it has to be evaluated from other quantities, such as the total radiated sound power, and the mean square velocity of the vibrating surface. Two methods to evaluate the radiated sound power, based on different assumption, have been compared, highlighting advantages and limitations. The influence of the spatial sampling, i.e. the number of measurement positions and their distribution on the plate surface, on the mean square velocity, and thus on the radiation efficiency, has been investigated.

Acoustically excited building elements are usually analysed in terms of sound transmission loss. It is computed from the transmission coefficient, defined as the ratio of the sound power incident on the excited surface, to the sound power transmitted through the partition and radiated in the receiving side. Sound transmission through different materials can be modelled by means of the transfer matrix method. The transmission loss of a CLT panel has been evaluated modelling the structure as an equivalent orthotropic thin plate. The results are validated with experimental data.

Further, a general model to predict sound transmission through multi-layer elements considering the presence of mechanical connections has been developed within the transfer matrix framework. The model, based on the decoupled approach, takes into account airborne and structure-borne transmission paths as independent additive contributions. The model can be applied to layers of different nature: elastic solid, orthotropic thin plate, fluid, and poroelastic. The different radiation mechanisms associated to excitations of different nature play a key role in this approach. A homogenisation technique, specifically developed for masonry brick wall but generally valid for any kind of wall, has been proposed to obtain the equivalent elastic properties of the partition, that one has to know in order to implement the transfer matrix method. The elastic properties of an equivalent homogeneous element are derived by means of a numerical procedure, based on a minimisation algorithm, as a function of the measured transmission loss. The decoupled model is finally validated with the experimental transmission loss measured on an External Thermal Insulation Composite System (*ETICS*), constituted by a masonry wall clad with high-density mineral wool slabs. Moreover, its applicability to lightweight structures, such as double-wall systems, is verified.

# Riassunto

L'attività di ricerca svolta durante questi tre anni si è focalizzata principalmente sulla radiazione e trasmissione acustica nelle partizioni degli edifici, con l'obiettivo di sviluppare dei modelli di calcolo efficienti e affidabili, per offrire strumenti utili per la progettazione. I modelli previsionali rappresentano sicuramente una preziosa risorsa per i progettisti, per l'ottimizzazione delle prestazioni acustiche degli elementi edilizi necessaria per il raggiungimento di un comfort acustico ottimale all'interno degli ambienti di vita. Particolare attenzione è stata dedicata ai dati di input necessari all'implementazione dei questi modelli, sviluppando sia metodi sperimentali per la loro determinazione, che procedure numeriche di approssimazione.

L'efficienza di radiazione è un importante descrittore, necessario come dato di input nella maggior parte dei modelli di calcolo; questo parametro caratterizza la capacità di una struttura di convertire l'energia vibrazionale in energia sonora nel fluido circostante. La determinazione di questo parametro, nel range di frequenze solitamente investigato in acustica edilizia: 50 – 5000 Hz, utilizzando codici di calcolo agli elementi, o ai contorni finiti, richiederebbe uno sforzo computazionale notevole. Infatti, diversi autori hanno presentato formulazioni analitiche o approssimate per valutare l'efficienza di radiazione di strutture omogenee isotrope. Tuttavia, le strutture ortotrope non sono state studiate così approfonditamente. In questa dissertazione sono presentati due diversi modelli di calcolo, appositamente sviluppati per determinare l'efficienza di radiazione di strutture edilizie ortotrope, come i pannelli in legno cross-laminato (CLT). I due diversi approcci presentati si basano su ipotesi differenti e offrono un diverso grado di accuratezza. Il comportamento dinamico dei pannelli in CLT viene spesso analizzato utilizzando teorie di ordine superiore, per esempio per nella progettazione strutturale, tuttavia, per le analisi vibro-acustiche sviluppate in questo progetto di ricerca, sono stati assimilati a una piastra sottile ortotropa, sotto l'ipotesi di piccoli spostamenti. I meccanismi di radiazione sonora da parte di una struttura vibrante sono fortemente influenzati dalla natura della forzante che induce il campo vibrazionale. Pertanto, sono stati considerati sia l'azione di una forzante meccanica agente sul pannello, sia un campo acustico incidente. Utilizzare dei dati di input affidabili per l'implementazione dei modelli è fondamentale per ottenere dei risultati accurati. È stata sviluppata una procedura speri-

---

mentale non-distruttiva per determinare la rigidezza flessionale dinamica di una piastra ortotropa, in funzione della direzione di propagazione dell'onda vibrazionale. I modelli previsionali per una piastra ortotropa sono stati validati attraverso i dati sperimentali ottenuti da misurazioni su pannelli in CLT. Al momento non esiste una procedura standardizzata per la determinazione sperimentale dell'efficienza di radiazione. Questo descrittore acustico non è direttamente misurabile, ma deve essere determinato da altre grandezze: la potenza sonora irradiata e la velocità di vibrazione media del pannello. Sono state confrontate due diverse metodologie per valutare sperimentalmente la potenza sonora irradiata, evidenziandone i vantaggi e le limitazioni. È stata analizzata inoltre l'influenza del campionamento spaziale, cioè del numero di posizioni di misura e della loro distribuzione sulla superficie della piastra, sulla velocità media e conseguentemente sull'efficienza di radiazione. Le strutture eccitate da un campo acustico incidente sono generalmente analizzate in termini di isolamento acustico, invece che radiazione sonora. L'isolamento acustico viene calcolato in funzione del coefficiente di trasmissione, definito come il rapporto tra la potenza sonora incidente sulla superficie eccitata e la potenza sonora irradiata nell'ambiente ricevente. La trasmissione sonora attraverso diversi materiali può essere modellata con il metodo delle matrici di trasferimento. Questo metodo è stato implementato per determinare l'isolamento acustico fornito da un pannello in CLT, modellato come una piastra sottile ortotropa e validando i risultati confrontandoli con i dati ottenuti sperimentalmente.

È stato sviluppato un modello generale, implementato con il metodo delle matrici di trasferimento, per simulare la trasmissione sonora attraverso delle strutture multistrato, tenendo in considerazione la presenza di connessione meccaniche. Il modello, basato sull'approccio disaccoppiato, calcola la trasmissione sonora per via aerea e la trasmissione per via strutturale come contributi indipendenti e additivi. Il modello può essere applicato a strati di diversa natura: solidi elastici, piastre sottili ortotrope, fluidi e materiali poroelastici. I diversi meccanismi di radiazione sonora, associati al tipo di eccitazione esterna, giocano un ruolo chiave in questo approccio. Viene proposta una tecnica di omogeneizzazione, sviluppata per pareti in muratura, ma potenzialmente applicabile a qualunque partizione, per determinazione delle proprietà meccaniche, necessarie per una corretta modellazione dell'elemento con il metodo delle matrici di trasferimento. Le caratteristiche elastiche di un solido omogeneo equivalente sono ricavate in funzione dell'isolamento acustico sperimentale attraverso un algoritmo di minimizzazione. Infine, il modello disaccoppiato, basato sul metodo delle matrici di trasferimento, è validato attraverso i risultati sperimentali di isolamento acustico misurati su un sistema *ETICS*: External Thermal Insulation Composite System; costituito da una parete in muratura, rivestita con pannelli di lana minerale. Inoltre, ne è stata verificata l'applicabilità a strutture leggere come contropareti in cartongesso e elementi a doppia lastra metallici.

# List of Symbols

## General symbols

$\mathbf{D}$	global transfer matrix: multilayer element with semi-infinite fluid termination	
$\mathbf{I}_{ij}, \mathbf{J}_{ij}$	coupling matrices between layers $i - j$	
$\mathbf{T}_{\text{layer}_i}$	transfer matrix of $i^{\text{th}}$ medium	
$\nabla^2$	laplacian operator	
$\nabla^4$	biharmonic operator	
$\langle \rangle_{s,t}$	time and spatial average	
$i$	imaginary unit: $i^2 = -1$	
$F_0$	point force amplitude	[N]
$F_b$	force exerted by bridges	[N]
$J_1$	first order Bessel's function	
$m, n, p, q$	modal indices	
$n_p$	number of accelerometers	
$S_1$	first order Struve's function	
$V_{S_i}$	vector of the field variables associated with $i^{\text{th}}$ surface	
$Y_{S_i}$	point/line-drive mobility of the surface $S_i$	[m (Ns) <sup>-1</sup> ]

## Frequency, time, and spatial variables

$\mathbf{r}, \bar{\mathbf{r}}$	position vector of points on the plate surface and in the fluid domain	[m]
$\Delta d_{ij}$	distance between $i$ - $j$ transducers	[m]
$\Delta t_{ij}$	time of arrival difference between transducers $i - j$	[s]
$\Delta \varphi_{ij}$	phase shift between transducers $i - j$	[rad.]
$\omega$	angular frequency	[rad./s]
$\omega_{mn}$	natural angular frequency of mode $(m, n)$	[rad./s]
$\phi$	azimuthal angle on the plate's surface	[rad.]
$\theta$	incidence angle to the normal of the plate	[rad.]
$a_i$	equivalent radius of $i^{\text{th}}$ piston source	[m]
$d_{ij}$	distance between $i$ - $j$ piston sources	[m]
$n_r$	normal to the plate surface in the $z > 0$ direction	
$s_i$	equivalent area of $i^{\text{th}}$ piston source	[m <sup>2</sup> ]
$S_T$	total surface area of the receiving room	[m <sup>2</sup> ]
$t$	time	[s]

## List of Symbols

---

$T_{20}$	reverberation time in the receiving room	[s]
$x, y, z$	Cartesian coordinates	[m]

### Vibrational field variables

$\gamma_i$	shear strain in $ij$ -plane $i, j = x, y, z$	
$\langle v^2 \rangle$	mean square velocity of the plate surface	$[(\text{ms}^{-1})^2]$
$\langle v_{mn}^2 \rangle$	mean square velocity of the plate surface associated with mode $(m, n)$	$[(\text{ms}^{-1})^2]$
$\mathcal{A}_{mnpq}$	modal admittance matrix coefficients	
$\mathcal{H}$	Hamiltonian functional	[J]
$\mathcal{L}$	Lagrangian function	[J]
$\mathcal{T}$	kinetic energy	[J]
$\mathcal{V}$	strain energy of bending	[J]
$\mathcal{W}_f$	work associated with the acoustic pressure	[J]
$\mathcal{W}_e$	work done by the external force	[J]
$\bar{w}_i$	complex wave amplitude	
$\psi_{mn}$	shape function of plate's mode $(m, n)$	
$\varepsilon_i$	normal strain along $i$ -direction $i = x, y, z$	
$\varphi_{mn}$	phase shift associated with vibrational mode $(m, n)$	[rad.]
$\xi$	plate longitudinal displacements along $x$ -direction	[m]
$\zeta$	plate longitudinal displacements along $y$ -direction	[m]
$A_i$	real wave amplitude	
$A_{mn}$	participation factor of plate's mode $(m, n)$	
$a_{mn}$	modal coefficients of transverse displacement amplitude	
$f_{e,mn}$	modal external excitation coefficients	
$f_e(x, y, t)$	external exciting force	[N]
$G(r, \bar{r})$	Green's function	
$K_{mnpq}$	modal stiffness matrix coefficients	
$M_{mnpq}$	modal mass matrix coefficients	
$v_i$	complex velocity of $i^{\text{th}}$ piston source	$[\text{ms}^{-1}]$
$v_{S_i, b}^2$	mean square velocity of the surface $S_i$ due to the force action	$[(\text{ms}^{-1})^2]$
$v_{S_i}^2$	mean square velocity of the surface $S_i$	$[(\text{ms}^{-1})^2]$
$w$	plate transverse displacements along $z$ -direction	[m]
$Z_{mnpq}$	modal radiation impedance matrix coefficients	

### Acoustic field variables

$\lambda_t$	trace wavelength	[m]
$\langle p^2 \rangle$	mean square acoustic pressure in the receiving room	$[\text{Pa}^2]$
$\mathcal{R}$	complex reflection coefficient	
$\mathcal{T}$	complex transmission coefficient	
$\sigma$	average radiation efficiency	
$\sigma_a$	airborne radiation efficiency	



## List of Symbols

---

$\sigma_b$	radiation efficiency due to point/line force	
$\sigma_i$	normal stress along $i$ -direction $i = x, y, z$	
$\sigma_r$	resonant radiation efficiency	
$\sigma_{finite}$	finite size radiation efficiency (see $\sigma_{nr}$ )	
$\sigma_{mn}$	modal radiation efficiency of mode $(m, n)$	
$\sigma_{nr}$	non-resonant radiation efficiency	
$\tau_i$	shear stress in $ij$ -plane $i, j = x, y, z$	
$\tau_\infty$	transmission coefficient of an infinitely extended element	
$\tau_{finite}$	finite size transmission coefficient	
$\tau_{tot}$	transmission coefficient considering both airborne and structure-borne contributions	
$k_t$	trace wavenumber	[rad.m <sup>-1</sup> ]
$n_{mn}$	norm of the plate's mode $(m, n)$	
$p$	acoustic pressure distribution in the fluid domain	[Pa]
$p_b$	blocked pressure on the plate surface	[Pa]
$p_i(x, y, z, t)$	exciting incident plane wave	[Pa]
$R$	plate's radiation resistance (real part of $Z$ )	[Pam <sup>-1</sup> ]
$r_r$	ratio of resonant field to non-resonant/near field	
$W_a$	sound power radiated due to airborne excitation	[W]
$W_b$	sound power radiated due to the bridges action	[W]
$W_{mn}$	radiated sound power from vibrational mode $(m, n)$	[W]
$W_{rad}$	total radiated sound power	[W]
$X$	plate's radiation reactance (imaginary part of $Z$ )	[Pam <sup>-1</sup> ]
$Z$	plate's radiation impedance	[Pam <sup>-1</sup> ]
$Z_{ii}$	self radiation impedance of $i^{th}$ piston source	[Pam <sup>-1</sup> ]
$Z_{ij}$	mutual radiation impedance of piston sources $i-j$	[Pam <sup>-1</sup> ]

### Materials and structures characteristics

$\alpha$	tortuosity	
$\kappa$	Mindlin's shear coefficient	
$\Lambda$	viscous characteristic length	[ $\mu$ m]
$\Lambda'$	thermal characteristic length	[ $\mu$ m]
$\lambda_B$	bending wavelength	[m]
$\mu$	dimensionless bending wavenumber: $k_B/k_0$	
$\nu$	Poisson's ratio	
$\nu_{ij}$	elastic constant associate with the plate geometric configuration $i, j = x, y, z$	
$\phi$	open porosity	
$\rho$	material density	[kgm <sup>-3</sup> ]
$\rho_0$	fluid density	[kgm <sup>-3</sup> ]
$\sigma$	airflow resistivity	[sPa/m <sup>-2</sup> ]
$B$	effective torsional stiffness of the plate	[Nm]
$c_0$	wave velocity in fluid medium	[ms <sup>-1</sup> ]
$c_B$	bending wave phase velocity	[ms <sup>-1</sup> ]

## List of Symbols

---

$c_g$	bending group velocity	$[\text{ms}^{-1}]$
$c_L$	quasi-longitudinal wave velocity	$[\text{ms}^{-1}]$
$c_T$	transverse wave velocity	$[\text{ms}^{-1}]$
$D$	bending stiffness of the plate	$[\text{Nm}]$
$D(\phi)$	orthotropic bending stiffness	$[\text{Nm}]$
$E$	Young's modulus of an isotropic material	$[\text{Pa}]$
$E_\phi$	Young's modulus along $\phi$ -direction	$[\text{Pa}]$
$E_i$	Young's modulus associated with $i$ -direction, $i = x, y, z$	$[\text{Pa}]$
$G$	shear modulus of an isotropic material	$[\text{Pa}]$
$G_{ij}$	shear modulus associated with $ij$ plane $i, j = x, y, z$	$[\text{Pa}]$
$G_{z\phi}$	shear modulus in $z - \phi$ plane	$[\text{Pa}]$
$h$	plate thickness	$[\text{m}]$
$I$	plate's mass moment of inertia	$[\text{kg}]$
$k_0$	wavenumber in the fluid domain	$[\text{rad}\cdot\text{m}^{-1}]$
$k_B$	free bending wavenumber	$[\text{rad}\cdot\text{m}^{-1}]$
$k_x$	bending wavenumber component along $x$ -direction	$[\text{rad}\cdot\text{m}^{-1}]$
$k_y$	bending wavenumber component along $y$ -direction	$[\text{rad}\cdot\text{m}^{-1}]$
$k_{mn}$	structural wavenumber	$[\text{rad}\cdot\text{m}^{-1}]$
$L_x, L_y$	plate dimensions	$[\text{m}]$
$n_d(\omega)$	plate's modal density	$[(\text{Hz} \cdot \text{rad})^{-1}]$
$S$	plate's surface	$\text{m}^2$
$V$	plate volume	$[\text{m}^3]$
$Z(\omega, \phi)$	mechanical impedance of the orthotropic thin plate	$[\text{Nsm}^{-1}]$

## Abbreviations

BEM	Boundary Element Method
CLT	Cross-Laminated Timber
ETICS	External Thermal Insulation Composite System
FEM	Finite Element Method
FTMM	Finite Transfer Matrix Method
SEA	Statistical Energy Analysis
TL	Transmission Loss
TMM	Transfer Matrix Method

# Table of Contents

<b>1</b>	<b>Introduction</b>	<b>1</b>
1.1	Predicting sound transmission in buildings . . . . .	2
1.1.1	Sound radiation of rectangular panels: state of the art	3
1.1.2	Sound transmission through multilayer structures . .	5
1.2	Objective of the research . . . . .	7
1.3	Dissertation outline . . . . .	7
<b>2</b>	<b>Background on plate dynamics</b>	<b>9</b>
2.1	Waves in solid media . . . . .	9
2.2	Bending waves in isotropic plates . . . . .	10
2.2.1	Thin plate theory . . . . .	11
2.2.2	Modal approach solution . . . . .	13
2.3	Influence of shear deformation and rotational inertia . . . . .	14
<b>3</b>	<b>Sound radiated from orthotropic plates</b>	<b>17</b>
3.1	Introduction . . . . .	17
3.2	Orthotropic elastic solids . . . . .	18
3.3	Derivation of the basic equations . . . . .	19
3.3.1	In-vacuum vibration . . . . .	19
3.3.2	Plate immersed in a fluid . . . . .	22
3.4	Analytical sound radiation model . . . . .	23
3.4.1	Mass matrix coefficients . . . . .	24
3.4.2	Stiffness matrix coefficients . . . . .	25
3.4.3	Radiation impedance matrix coefficients . . . . .	25
3.4.4	Excitation coefficients . . . . .	26
3.4.5	Vibro-acoustic indicators . . . . .	27
3.5	Influence of fluid loading . . . . .	28
3.5.1	Modal radiation efficiency . . . . .	29
3.5.2	Modal summation approach . . . . .	30
3.6	Resonant and non-resonant modes . . . . .	31
3.7	Average radiation efficiency model . . . . .	35
3.7.1	Near-field and non-resonant contribution . . . . .	38
3.8	Conclusion . . . . .	40

Table of Contents

---

<b>4</b>	<b>Sound radiation efficiency of CLT plates</b>	<b>43</b>
4.1	Introduction . . . . .	43
4.2	Experimental measurements . . . . .	45
4.2.1	Studied structures . . . . .	45
4.2.2	Radiated sound power . . . . .	46
4.2.3	Average vibration velocity . . . . .	49
4.3	Experimental results . . . . .	50
4.3.1	CLT plates' radiation efficiency . . . . .	50
4.3.2	Comparison between diffuse field approach and DCM	52
4.3.3	Average vibration velocity . . . . .	54
4.4	Mechanical characterisation of CLT plate . . . . .	59
4.4.1	Experimental flexural wave analysis . . . . .	59
4.4.2	Experimental results . . . . .	62
4.5	Validation of sound radiation models . . . . .	70
4.6	Plate boundary conditions . . . . .	79
4.7	Conclusion . . . . .	80
<b>5</b>	<b>Sound transmission through building elements</b>	<b>84</b>
5.1	Introduction . . . . .	84
5.2	Transfer matrix method . . . . .	85
5.3	Orthotropic elastic medium . . . . .	87
5.4	Structural bridges . . . . .	89
5.4.1	Modelling structural connections within TMM . . . . .	89
5.4.2	Characterisation of equivalent homogeneous walls . . . . .	94
5.4.3	Experimental validation . . . . .	96
5.5	Conclusion . . . . .	104
<b>6</b>	<b>Conclusion</b>	<b>108</b>
6.1	Overview . . . . .	108
6.2	Future developments . . . . .	111
<b>A</b>	<b>Stiffness Matrix Coefficients</b>	<b>113</b>
<b>B</b>	<b>Radiation Impedance Matrix Coefficients</b>	<b>115</b>
<b>C</b>	<b>Leppington's asymptotic equations</b>	<b>122</b>
<b>D</b>	<b>Transfer and coupling matrices</b>	<b>125</b>
D.1	Fluid medium . . . . .	125
D.2	Solid medium . . . . .	125
D.3	Poroelastic medium . . . . .	126
D.4	Coupling matrices . . . . .	128
D.5	<i>ETICS</i> : Global transfer matrix . . . . .	129
	<b>Bibliography</b>	<b>130</b>

# List of Figures

2.1	Bending waves deformation: differences between Kirchhoff's theory for thin plates a), and Mindlin's theory for thick plates b) . . . . .	15
2.2	Comparison between flexural wave dispersion curves, derived under Kirchhoff's and Mindlin's theory. The normalised wave velocity: $\bar{c} = c/c_L$ is plotted against the normalised wavenumber: $\bar{k} = kh/2\pi$ . Recreated from Ref. [49]. . . . .	16
3.1	Elastic thin orthotropic plate inserted in a infinite rigid baffle, radiating sound energy in a semi-infinite fluid domain $z > 0$ . .	19
3.2	a) self radiation resistance $R$ and reactance $X$ of modes (1, 1) and (2, 2); b) cross radiation resistance $R$ and reactance $X$ of modes (1, 3) – (1, 1) and (1, 1) – (3, 3) . . . . .	29
3.3	Resonant and non-resonant modes represented in the wavenumber space: the shaded area represents the frequency range of the exciting source. Resonant modes are identified in the wavenumber space by points falling within the shaded region. . . . .	32
3.4	Different radiation modes represented in the normalised wavenumber space. a) modes above the coincidence; b) edges modes; c) $y$ -edge modes; d) $x$ -edge modes; d) corners modes. . . . .	33
3.5	Cross-cancellation representation for a) corner mode: $\lambda_x, \lambda_y < \lambda_0$ ; b) edge mode: $\lambda_x \geq \lambda_0$ and $\lambda_y < \lambda_0$ . . . . .	34
3.6	a) Matching between the bending wavelength propagating in the plate and the wavelength of the radiated acoustic wave propagating away from the surface; b) Matching between the incident acoustic wavelength, and the forced trace wavelength propagating in the plate. . . . .	35
4.1	Cross section along the two principle directions of the three investigated CLT plates. . . . .	46
4.2	Experimental set-up diagram: CLT plate mounted into the sound insulation test facility. . . . .	47
4.3	Mounting condition of the investigated CLT plates . . . . .	48

List of Figures

---

4.4	Measurement points distributions: a) grid of 513 points; b) grid of 140 points; d) 27 random points fulfilling EN 10848 requirements; d) grid 425 points excluding boundary regions.	50
4.5	Experimental radiation index of the three CLT plates for mechanical excitation. Results presented in one-third octave bands. . . . .	51
4.6	Experimental radiation index of the three CLT plates excited by a diffuse sound field. Results presented in one-third octave bands. . . . .	52
4.7	Comparison between the experimental radiation indices for mechanical excitation and airborne excitation. The results, in one-third octave bands, refer to the plate CLT80_b mechanically excited. . . . .	53
4.8	Comparison between the experimental radiation indices obtained from the Diffuse field approach and the DCM. The results, in one-third octave bands, refer to the plate CLT80_b mechanically excited. . . . .	54
4.9	Comparison between the radiation efficiency from DCM considering a 513 measurement points grid or a 140 measurement points grid. The results, in one-third octave bands, refer to the plate CLT80_b mechanically excited. . . . .	55
4.10	Comparison between the surface mean square velocity averaged over 513 measurement points and over 140 measurement points. The results, in one-third octave bands, refer to the plate CLT80_b mechanically excited. . . . .	56
4.11	Comparison between the mean square velocity averaged over the entire surface (513 points grid) or over a reduced region excluding the border region: grids of 425 points; 345 points; 273 points. The results, in one-third octave bands, refer to plate CLT80_b mechanically excited. . . . .	57
4.12	Comparison between the mean square velocity averaged over (n) measurement positions randomly distributed on the panel surface. The results, in one-third octave bands, refer to plate CLT80_b mechanically excited. . . . .	57
4.13	Overall velocity level difference $\Delta L_V$ between the level averaged over the entire set of 513 points and the level averaged over (n) measurement positions randomly distributed on the surface of the panel CLT80_b. . . . .	58
4.14	Comparison between the mean square velocity averaged over a grid of 513 points and over a random distribution of measurement positions chosen according to the requirements of EN 10848-1. The results, in one-third octave bands, refer to plate CLT80_b mechanically excited. . . . .	58

4.15	Experimental setup for different propagation angles at steps of $\Delta\phi = \pi/8$ . The first measurement position is placed at a minimum distance $l_1 = 50$ cm from the excitation point to avoid near field effects and the accelerometers are equally spaced: $\Delta d = 10$ cm. . . . .	60
4.16	Evaluation of the time of flight of a flexural wave between two consecutive measurement positions: $f = 3100$ Hz – $\phi = \pi/2$ . .	61
4.17	Comparison between the frequency dependent elastic properties of an equivalent thin orthotropic plate and the elastic constants derived using Mindlin’s thick plate theory, associated with the principal directions. . . . .	63
4.18	Elliptic model: comparison between the elliptic and the experimental wavenumbers, determined for the angles: $\pi/8$ , $\pi/4$ and $3\pi/8$ ; at the frequencies: 100 Hz; 200 Hz, 500 Hz, 1000 Hz, 2000 Hz and 3000 Hz. . . . .	64
4.19	Elliptic model: comparison between the elliptic and the experimental bending stiffness, determined for the angles: $\pi/8$ , $\pi/4$ and $3\pi/8$ ; at the frequencies: 100 Hz; 200 Hz, 500 Hz, 1000 Hz, 2000 Hz and 3000 Hz. . . . .	65
4.20	CLT plate bending stiffness frequency and direction dependent: a) elliptic approximation using equation (3.65); b) thin plate orthotropic bending stiffness computed using equations (3.64)	66
4.21	a) – Experimental wave velocity determined with the phase difference ( <i>phd</i> ) and the time of flight ( <i>tof</i> ) methods. b) – Curve fitting of the experimental wave velocity using Mindlin’s dispersion relation. The shaded area represents the measured data standard deviation. Propagation angle: $\phi = 0$ . . . . .	66
4.22	a) – Experimental wave velocity determined with the phase difference ( <i>phd</i> ) and the time of flight ( <i>tof</i> ) methods. b) – Curve fitting of the experimental wave velocity using Mindlin’s dispersion relation. The shaded area represents the measured data standard deviation. Propagation angle: $\phi = \pi/8$ . . . . .	67
4.23	a) – Experimental wave velocity determined with the phase difference ( <i>phd</i> ) and the time of flight ( <i>tof</i> ) methods. b) – Curve fitting of the experimental wave velocity using Mindlin’s dispersion relation. The shaded area represents the measured data standard deviation. Propagation angle: $\phi = \pi/4$ . . . . .	67
4.24	a) – Experimental wave velocity determined with the phase difference ( <i>phd</i> ) and the time of flight ( <i>tof</i> ) methods. b) – Curve fitting of the experimental wave velocity using Mindlin’s dispersion relation. The shaded area represents the measured data standard deviation. Propagation angle: $\phi = 3\pi/8$ . . . . .	68

4.25	a) – Experimental wave velocity determined with the phase difference ( <i>phd</i> ) and the time of flight ( <i>tof</i> ) methods. b) – Curve fitting of the experimental wave velocity using Mindlin’s dispersion relation. The shaded area represents the measured data standard deviation. Propagation angle: $\phi = \pi/2$ . . . . .	68
4.26	Comparison between wave velocity obtained by using an experimental frequency vector with regular steps of 40 Hz and steps of 160 Hz, within the range 100 – 3150 Hz. Propagation angle: $\phi = \pi/2$ . . . . .	69
4.27	Comparison between the radiation index of a baffled steel plate obtained from the proposed code, either considering $L_{\sigma, Z_{mnpq}}$ or neglecting $L_{\sigma, R_{mn}}$ the fluid loading effect, and the results presented in Figure 2 of Ref. [17] $L_{\sigma, F_{oin}}$ . . . . .	71
4.28	Modal and average radiation efficiency of an aluminium plate, obtained from the code based on the modal summation approach. The average radiation efficiency is compared with the results presented in Figure 3 of Ref. [19]. . . . .	72
4.29	Average radiation index of an orthotropic carbon laminate plate, obtained from the proposed modal-average approach, compared with the results presented in Figure 10 of Ref. [30].	73
4.30	Radiation efficiency of a CLT plate: comparison between the analytical model results and experimental data related to the position of the exciting force $S_1$ . Results presented in one-third octave bands. . . . .	75
4.31	Comparison between the CLT plate’s radiation index computed considering the fluid loading $L_{\sigma, Z_{mnpq}}$ and the approximated results computed considering the self radiation resistance $R_{\sigma, Z_{mnpq}}$ . Results obtained from the analytical model are presented in one-third octave bands and refers to exciting force $S_1$ . . . . .	75
4.32	Radiation efficiency of a CLT plate: comparison between the analytical model results and experimental data related to the position of the exciting force $S_2$ . Results presented in one-third octave bands. . . . .	76
4.33	Radiation efficiency of a CLT plate: comparison between the analytical model results and experimental data obtained with a diffuse field excitation. Results presented in one-third octave bands. . . . .	77
4.34	Radiation efficiency of a CLT plate: comparison between the numerical results obtained from the modal summation approach and from the analytical model averaged over two source positions. Results presented in narrow band. . . . .	77



4.35	Radiation efficiency of a CLT plate: comparison between the numerical results obtained from the modal-average approach and experimental data averaged over two source positions. Results presented in one-third octave bands. . . . .	78
4.36	Radiation efficiency of a CLT plate: comparison between results obtained considering the orthotropic bending stiffness and its elliptic approximation. Results presented in one-third octave bands. . . . .	78
4.37	Plate measured displacements. Mechanical source $S_1$ . . . . .	80
4.38	Plate measured displacements. Airborne excitation . . . . .	81
5.1	An acoustic wave impinging on a stratified structure with an incidence angle $\theta$ . The multilayer element is surrounded by a semi-infinite fluid on both sides. . . . .	86
5.2	Sound transmission loss of the plate CLT80_b, comparison between experimental data and FTMM results. . . . .	89
5.3	Mapping of the vibration velocity levels distribution on a 1 square metre sample of the finishing layer of the <i>ETICS</i> system. (a) Mechanical connection mounting condition: • 7 bridges per square metre represents the standard in real conditions. (b) Mounting condition without mechanical connections. . . . .	91
5.4	Outline of the minimisation algorithm to determine the apparent elastic properties of the equivalent homogeneous layer. . . . .	94
5.5	Estimated values of $E$ associated to different values of $\eta$ of the equivalent homogeneous layer. . . . .	96
5.6	Diagram of the multilayer <i>ETICS</i> system modelled using FTMM. In order to consider the transmission contribution due to the bridges action, which is neglected by the FTMM, the mechanical force $F_b$ is determined as a function of the velocity $v_{S_1,F}$ . . . . .	97
5.7	Diagram of the <i>ETICS</i> system mounted on the basic masonry wall and the definition of TMM media. (a) The mounting condition involves only adhesive mortar without mechanical connections; (b) Both mortar and mechanical fixings are used to mount the cladding system on the basic wall. For each condition, a picture of the system before the finishing layer was applied is shown. . . . .	99
5.8	Transmission loss experimentally evaluated on the basic wall and on the multilayer structure, with and without the mechanical fixing. . . . .	100
5.9	Transmission loss of the <i>ETICS</i> system without structural connection. Comparison between the FTMM results and experimental data. . . . .	101

5.10	Ratio between the mean square velocities on the external surfaces of the multilayer structure. The experimental results, measured on the sample without mechanical bridges, are compared with numerical data obtained from the TMM .	102
5.11	Comparison between the total vibration velocity measured on the plaster layer surface, on the structure with mechanical connections multiplied by the radiation efficiency experimentally evaluated, and numerical surface velocity ratios with and without bridges multiplied respectively by the airborne and point-driven radiation efficiency. . . . .	103
5.12	Sound power levels radiated by the building element, experimentally determined from sound intensity measurements. . .	104
5.13	Transmission loss of the <i>ETICS</i> system with structural connection. Comparison between the FTMM results and experimental data. . . . .	105
5.14	Transmission loss of a clay brick wall lined with an <i>ETICS</i> system using a double density mineral wall. Comparison between the FTMM results and experimental data. . . . .	106
5.15	Transmission loss of a double leaf aluminium plate with structural line connections. Comparison with Figure 3, and 4 of Ref. [32]. . . . .	107
5.16	Transmission loss of a double leaf gypsum board with metal studs. Comparison with Figure 6 of Ref. [42]. . . . .	107
A.1	Coordinates transform given in equation (A.1) . . . . .	113
B.1	Coordinates transform given in equation (B.1) . . . . .	115
B.2	Coordinates transform given in equation (B.3) . . . . .	116
B.3	Comparison between the CLT plate average radiation efficiency computed considering the radiation impedance coefficients $Z_{mnpq}$ and its approximation with the self radiation resistance coefficients $R_{mn}$ . Plate mechanically excited in the position $S_1$ . Results given in one-third octave bands. . . . .	118
B.4	Comparison between the CLT plate average radiation efficiency computed considering the radiation impedance coefficients $Z_{mnpq}$ and its approximation with the self radiation resistance coefficients $R_{mn}$ . Plate mechanically excited in the position $S_2$ . Results given in one-third octave bands. . . . .	119
B.5	Comparison between the CLT plate average radiation efficiency computed considering the radiation impedance coefficients $Z_{mnpq}$ and its approximation with the self radiation resistance coefficients $R_{mn}$ . Diffuse sound field excitation. Results given in one-third octave bands. . . . .	119

List of Figures

---

B.6	Comparison between the CLT plate average radiation efficiency computed considering the radiation impedance coefficients $Z_{mnpq}$ and its approximation with the self radiation resistance coefficients $R_{mn}$ . Plate mechanically excited in the position $S_1$ . Results given in narrow band. . . . .	120
B.7	Comparison between the CLT plate average radiation efficiency computed considering the radiation impedance coefficients $Z_{mnpq}$ , and the approximation with the self radiation resistance coefficients $R_{mn}$ . Plate mechanically excited in the position $S_2$ . Results given in narrow band. . . . .	120
B.8	Comparison between the CLT plate average radiation efficiency computed considering the radiation impedance coefficients $Z_{mnpq}$ , and the approximation with the self radiation resistance coefficients $R_{mn}$ . Diffuse sound field excitation. Results given in narrow band. . . . .	121
C.1	Determination of the average radiation efficiency for a single propagation direction by combining the curves defined in each frequency region: below-coincidence, near-coincidence, above-coincidence; . . . . .	123
C.2	Frequency dependent average radiation index for different propagation angles $\phi$ . . . . .	124

# List of Tables

3.1	Summary of the different models to compute sound radiation of isotropic and orthotropic plates . . . . .	42
4.1	CLT plates geometry and density . . . . .	45
4.2	CLT's elastic constants for different propagation angles . . .	63
4.3	Experimental bending wavenumbers and loss factor used as input data to model the cross-laminated timber plate CLT80_b	74
5.1	Elastic properties of the equivalent homogeneous plate used as input data for the basic wall in the FTMM model . . . . .	97
5.2	Mechanical, geometrical and acoustic descriptors used as input data in the FTMM model . . . . .	98

# Chapter 1

## Introduction

It is surprisingly difficult to give a general definition of the difference between sound and noise, even though the idea is quite clear in everybody's mind. From a physic point of view, noise and sound are exactly the same phenomenon: a pressure wave propagating in an elastic medium at certain frequencies that the human hearing system can percieve. In a fascinating book, professor David Hendy [1] treats this subject by talking about music, speeches, mechanical noise, ringing bells, crowded cities and many other examples of how noise, or sound, deeply influenced human life through the centuries from prehistory until now. To highlight the individual nature of the difference between noise and sound professor Hendy quotes the artist and composer John Cage: *"Whenever we are what we hear is mostly noise. When we ignore it, it disturbs us. When we listen to it, we find it fascinating"*. The disturbance of unwanted noise is often regarded as a secondary problem. However, the European Environmental Agency (EEA) recently published a report [2] depicting a serious situation, with more than 900 thousand people each year suffering of hypertension caused by environmental noise, and almost 8 million people suffer sleep disturbance. The environmental noise is defined *"a threat to public health,"* by the World Health Organisation (WHO) [3], *"having negative impacts on human health and well-being"*. Moreover, several indoor sources contribute to increase the noise annoyance inside living spaces. Nevertheless, with a careful specific acoustic design of building elements, it is possible to provide a comfortable indoor environment, reducing the noise annoyance. In order to optimize the acoustic performance of the partitions, and accomplish such comfort inside buildings, accurate prediction models represent an essential and useful tool during the design process. Modern buildings present additional challenges for acousticians and engineers. Service equipments and electrical appliances, more and more present in any building, give a significant contribution to indoor sound pressure levels, generating both airborne noise and vibrations, that propagate in the building structures and can be radiated as sound energy. Moreover,

alongside traditional construction materials such as concrete, steel, and clay bricks, new building technologies, mostly involving lightweight structures, have been lately introduced into the market, achieving a great success. For example, cross-laminated timber, an engineered wood material, has become increasingly popular during the last two decades. This technology provides good structural stability, the fulfilment of all the safety requirements, and allows to reduce time and costs. Nevertheless, these structures cannot provide a satisfying sound insulation, due to their relative high stiffness compared to their low density, and need to be conveniently treated in order to increase the acoustic performance and meet the regulation requirements. Moreover, cross-laminated timber plates due to their layered structures can be highly orthotropic, which means they have different elastic and stiffness properties along mutually orthogonal directions. It is of fundamental importance to take into account this particular behaviour in vibro-acoustic prediction models.

In order to increase noise reduction, both lightweight and massive partitions are usually lined with sound insulating systems. To better optimise the acoustic treatment and obtain a good sound insulation, specific tools to investigate sound transmission through the element are absolutely necessary. The sound transmission loss, provided by the partition, can be evaluated by modelling the sound wave propagation through each different material constituting the layered structure. One of the greatest complexities is represented by the mechanical characterisation of the different materials a building partition is made of, which in most of the cases are not simple homogeneous isotropic elements.

### 1.1 Predicting sound transmission in buildings

Sound transmission in buildings is usually regarded in terms of direct and flanking transmission. The former path represents the sound energy generated in one room and transmitted through a partition into the adjoining room. Flanking transmission directly involves structural acoustics too and it can be subdivided in three different processes: *generation* of the vibrational field either by an acoustic or a mechanical source; *propagation* of vibrational energy from the excited structure to other elements; *radiation* of the vibrational energy in the surrounding air as sound energy. To accurately predict sound transmission it is necessary to consider the interaction between the different structures, in which the vibrational field propagates, and also the interaction between these structures and the surrounding fluid, in which they may radiate sound energy. The finite element method (FEM) for interior problems, and boundary element method (BEM) for exterior problems, are largely used in many engineering fields. They certainly represent powerful tools to perform vibro-acoustic analysis. However, the computational complexity of such numerical models drastically increases, not only with the size of the geometry,

but also with the frequency. Even though the potential of FEM and BEM is virtually infinite, they require high performance processors, and a great effort in terms of memory and time, especially if the analysis is extended up to the highest frequencies considered in building acoustics. Even with modern powerful processors, and the latest developments to increase the performance of these methods, FEM and BEM remain particularly suitable for low/medium frequency analysis. An alternative approach to predict sound transmission in buildings is represented by statistical energy analysis (SEA) [4]: in which a complex system is modelled as a combination of sub-systems, and the transmission between each sub-element is computed in terms of energy flow, based on analytical formulations. The SEA framework is based on the assumption that both the acoustic and structural domains are usually characterised by high modal density. Although SEA is much more computationally efficient than numerical methods, it is normally considered applicable only to high frequency analysis. It should be mentioned that in the last years hybrid methods FEM/SEA for an extended frequency range analysis have been developed. The series of standards EN 12354 [5] provides a calculation model to predict sound transmission in buildings, based on a simplified SEA approach, which neglects higher order structure-borne paths. The EN 12354 models allow one to compute the acoustic performance of the buildings, starting from the performance of each single partition. The input data necessary to implement all these different models represent a crucial aspect. FEM and BEM require the material's elastic properties to be known. A trustworthy material characterisation of the studied structures is essential to achieve accurate and reliable results. Further, SEA-based models require also some acoustic descriptors to be known as input data, characterising for example the coupling between different structures, or between a structure and the surrounding fluid. It might be difficult to determine such descriptors for most of the structures commonly used in buildings, since the simple formulations given in the standards only apply to monolithic homogeneous and isotropic elements.

### 1.1.1 Sound radiation of rectangular panels: state of the art

John William Strutt, also known as Lord Rayleigh, certainly was a pioneer in the field of acoustics and sound radiation. The Rayleigh's integral, presented later on in equation (3.21), was derived in his book *Theory of sound* [6] and represents the starting point of several radiation models. Many analytical or approximated formulations to predict the radiated sound power have been proposed by several authors in the last fifty years; developed using different approaches and under different basic assumptions, upon which depends their suitability for each specific problem and the accuracy of the results. Based on a *non-modal approach*, the modal-average radiation efficiency can be evaluated assuming a high modal density and the validity of the

equipartition of modal energy [7], focusing on the radiation behaviour of each mode only at its natural frequency. While using a *modal approach*, the in-vacuo single mode radiation efficiency is approximated over the entire frequency range, neglecting the cross-modal coupling and the fluid loading effect [8]. The effect of cross-modal coupling, deeply investigated by Keltie and Peng [9], can be considered by means of *analytical formulations*. To this purpose, the radiation impedance of the vibrating structure is generally computed following two distinct approaches: (i) by solving the Rayleigh integral, either assuming the radiation in the far-field [10], or by means of near-field approximated numerical solutions [11, 12, 13]; (ii) through the analysis of travelling bending waves, by transforming the pressure distribution from space-time domain into wavenumber domain, using the spatial Fourier transform [14]. A comparison between these different approaches to compute the radiated sound power has been presented by Atalla and Nicolas in 1994 [15]. Later in the same decade, Nelisse [16] proposed a generalised model to determine the acoustic radiation from baffled and unbaffled homogeneous plates, with arbitrary boundary conditions, considering either lightweight or heavy fluids surrounding the structure. The same approach was also followed by Foin to develop a tool to predict the vibration response and sound radiation of sandwich plates [17, 18]. The average radiation efficiency of plates and strips was computed by Xie, Thompson and Jones by using a modal summation approach, based on the far field sound intensity [19]. Rhazi and Atalla used simple and quick tools, such as statistical energy analysis and transfer matrix method, to estimate the vibro-acoustic response of multi-layer structures mechanically excited [20]. Davy developed a two dimensional strip analytic approximation to compute the forced radiation efficiency of acoustically excited finite size panels [21]. Moreover, Davy recently presented an approximation method to calculate both the real and the imaginary part of single-side specific forced radiation impedance of a rectangular panel [22]. The possibility to consider both the resonant and non resonant contribution, in the case of acoustically excited plate, and the near-field contribution in the case of mechanical excitation, was also introduced by Davy in a recently published paper [23].

While isotropic plates have been deeply investigated both from a vibrational and radiation point of view, sound radiation from orthotropic structures has not been studied as thoroughly. Many studies focused on ribbed [24] or corrugated plates [25], which are often approximated as equivalent orthotropic elements. This approximation is valid if the ribs' spacing is less than half a bending wavelength, as pointed out by Langley et al. [26]. This was not the case for the ribbed plate investigated by Maidanik in Ref. [8], who could not approximate that structure to an equivalent orthotropic plate, because the ribs were too widely spaced. Guyader and Lesueur derived the equations of motion for free vibration of a multilayer orthotropic plate [27] by means of a variational formulation, in order to develop a sound



transmission model. An overview of vibro-acoustics analysis of multilayer structures was presented by D’Alessandro et al. a few years ago [28]. The sound radiation efficiency of orthotropic plates has been investigated by Hugin and Ohlirch [29]. While in 2005, Anderson and Bratos-Anderson developed a prediction tool to estimate the radiation efficiency of orthotropic carbon-laminate plates [30]. They compute the average radiation efficiency, both with a modal approach, neglecting the fluid loading effect and considering each mode only at its natural frequency, and by means of the asymptotic modal-average radiation, assuming a high modal density over the entire frequency range. Further, Mejdi and Atalla presented a semi-analytical model to predict the vibro-acoustic response of stiffened plates [31], while Legault [32] analysed orthogonally ribbed plates by means of a periodic theory. In this research project, the sound radiation of cross-laminated plates has been modelled by means of two different approaches, either conveniently extending an analytical model, developed for isotropic plates, in order to also analyse orthotropic structures, and by using a modal-average formulation. Under the assumption of small displacements, the dynamic response of cross-laminated timber panels has been determined regarding these structures as orthotropic thin plates.

Acoustically excited structures are often regarded in terms of sound transmission rather than sound radiation. Sound transmission through orthotropic multilayer plates was studied by Guyader and Lesueur [33] for an oblique incident plane wave, highlighting in particular the effects of layering and damping. The analysis was then extended to the case of diffuse field excitation [34]. Structure-borne sound transmission between orthotropic plates has been thoroughly investigated by Bosmans et al. [35]. More recently, sound insulation of plywood panels, characterised by soft orthotropy, has been studied by Wareing, Davy and Pearse [36], taking into account the finite dimension of the plate, by means of the geometrical radiation impedance. The sound transmission through an orthotropic medium was modelled within the transfer matrix framework by Lin, Wang, and Kuo, [37]. They developed a two-dimensional model, assuming in-plane isotropy, i.e. the stiffness properties along the  $z$ -direction differ from the properties in the plane  $x - y$ . The model was then extended by Kuo et al. [38], for the three-dimensional case, describing an orthotropic elastic solid characterised by the stress and strain relationship defined by nine independent constants. In these dissertation the sound transmission loss of a cross laminated timber plate is evaluated by means of the transfer matrix method, modelling the structure as a thin orthotropic plate.

### 1.1.2 Sound transmission through multilayer structures

Multilayer elements are largely used in building constructions: double-leaf walls, cavity wall systems, massive or lightweight partitions lined to increase

the insulating performance, and cladding systems are just a few examples. Due to the presence of structural connections linking the external layers, on the receiving side the sound is radiated due to both airborne and structure-borne excitation. The theoretical sound insulation that would be provided by the element without mechanical fixings is thus reduced, due to the structure-borne sound transmission via the mechanical connections. In 2006, an extensive comparison between more than twenty different approaches to predict sound transmission in double panels was presented by Hongisto [39]. Among them, only a few methods took into account the presence of structural connections. By means of a decoupled approach, the problem is simplified by computing the fluid-borne transmission through the cavity, and the structure-borne path through the connections, as independent additive contributions. The decoupled approach was developed by Sharp [40] and it considers the sound transmission through structural bridges by means of a correction factor, calculated as a function of the sound power radiated by a point (or line) connected panel [41]. Sharp's method was modified and inserted into the transfer matrix framework by Vigran [42], who also extended the validity of the method above the critical frequency. A different version of the decoupled approach, mainly focused on line-connections for cavity stud walls, was developed by Fahy and Gardonio [43]. The possibility to consider studs with finite stiffness, a problem first analysed by Gu and Wang [44], was introduced into Fahy's model by Davy [45, 46], through an equivalent mechanical compliance. Moreover, Davy recently published the full derivation of a prediction model for sound transmission via structural bridges, both for line and point connections [47]. The line-connections assumption is particularly useful to model cavity stud walls and double panel structures when the screw spacing is small compared to the bending wavelength of the wave propagating into the plate [48].

Although several formulations have been proposed, it is still difficult to model some of the basic building structures, such as masonry brick walls. While these models have been developed mainly for thin plates, this assumption does not always fit to massive partition. Moreover, these models cannot take into account sound transmission through poroelastic media. High-density porous or fibrous material, that are often used in linings or to fill cavity walls, cannot be modelled as equivalent fluids, like is usually done with low density material, because the transmission contribution through their solid frame is not negligible. In this dissertation a more general model based on the transfer matrix method is presented, which has been developed during the doctoral research project in order to take into account these aspects.

## 1.2 Objective of the research

The aim of this research undertaken during the last three years has been to investigate sound radiation and sound transmission in complex building elements, extending some of the existing prediction methods in order to consider homogeneous orthotropic panels, and multilayer structures. These models should represent efficient and reliable tools, handy during the acoustic design process. Particular attention has been paid to the input data necessary to implement these models, developing procedures for their experimental derivation, and numerical approximation.

## 1.3 Dissertation outline

In Chapter 2 the background theory on plates' dynamics is recalled. The solution of the equation of motion of a thin plate undergoing flexural vibration is derived from two different approaches, in order to introduce important concepts that will be largely used in the following Chapters. The differences between Kirchhoff's theory for thin plates and Mindlin's theory for thick plates are discussed.

In Chapter 3 two different models to estimate the radiation efficiency of an orthotropic rectangular plate are proposed. An analytical model is derived by using Hamilton's variational principle to obtain the governing equations. Both a mechanical point force excitation and an acoustic incident field are considered. The influence of fluid loading is investigated and an approximated formulation, which neglects its effects, is discussed. A modal-average radiation efficiency of orthotropic plates is introduced, and an approximated formulation for the plate bending stiffness based on an elliptic interpolation, which does not need the knowledge of the in-plane shear modulus, is proposed. The model is based on basic assumptions of high modal density, and equipartition of modal energy within the considered frequency range.

The models are developed in order to evaluate the radiation efficiency of cross-laminated timber elements used in buildings. An experimental analysis of the radiation efficiency performed on three-ply cross-laminated timber panels is presented in Chapter 4, both for mechanical and airborne excitation. Different approaches to evaluate the radiated sound power are investigated, highlighting advantages and limitations. The influence on the radiation efficiency of the spatial sampling adopted to measure the vibration velocity, namely the number of measurement positions and their distribution, is investigated and discussed. An experimental procedure, based on structural wave analysis, is proposed to determine the plate stiffness properties along the principle directions, necessary as input data to implement the prediction models. The experimental radiation efficiency is finally used to validated the

sound radiation models.

In Chapter 5, sound transmission through building elements is simulated using the transfer matrix method. The possibility to model cross-laminated timber elements as thin orthotropic plates is firstly investigated. Moreover, a general model to predict sound transmission through multilayer elements, taking into account transmission through structural connections, is proposed. Unlike most of the existing approaches, the model can consider both thin and thick plates, and poroelastic materials. It has been specifically developed for cladding systems used both on massive and lightweight partitions. A numerical procedure to determine the elastic properties of the basic walls, from the measured transmission loss, is presented in order to obtain the input data needed to implement the model.

## Chapter 2

# Background on plate dynamics

### 2.1 Waves in solid media

In a compressible isotropic, homogeneous fluid medium, such as the air that usually surrounds building structures, only compressional waves, also known as pure longitudinal waves, can propagate. The particles displacement due to a pure longitudinal wave is parallel to its propagation direction. In solid media however, different kinds of waves can propagate, such as quasi-longitudinal, transverse, and bending waves. The aim of this section is to recall some basic concepts on wave propagation in plates useful for further discussions of this thesis. A complete analysis and the derivation of the equations can be found in many textbooks, see for example [41].

**Quasi-longitudinal waves:** Pure longitudinal waves might occur in solids, only when the wavelength is smaller than the structure's dimension parallel to their propagation direction. This is not the case of building elements, at least not within the entire frequency range. In fact a compressional wave, with a wavelength larger than the solid element's dimension parallel to its propagation direction, induces a transverse displacement other than a longitudinal one. However, the transverse displacement induced by quasi-longitudinal waves is very small and it is often neglected in sound radiation analysis. From the differential equation that governs the propagation of this type of wave into a thin homogeneous plate it is possible to derive the longitudinal wave speed:

$$c_L = \sqrt{\frac{E}{\rho(1-\nu^2)}}. \quad (2.1)$$

**Transverse waves:** Since solids, unlike fluids, can resist tangential stresses, transverse plane waves, sometimes called shear waves, can also occur. The

## 2.2. Bending waves in isotropic plates

---

shear deformation induced by the propagation of a transverse wave involves changes in the shape of the element due to the rotation. Pure shear waves occur when the element's dimensions are larger than the propagating wavelength. In a wide range of frequencies, the displacements that a transverse wave induces in a plate are parallel to the surface, unable to excite the surrounding fluid. Again, from the wave equation it is possible to derive the transverse wave speed as:

$$c_T = \sqrt{\frac{G}{\rho}}. \quad (2.2)$$

Transverse waves propagate slower than quasi-longitudinal waves, since the shear modulus  $G$  of the plate is usually smaller than its Young's modulus  $E$ . It should be mentioned that another type of transverse waves, called torsional waves, can propagate in beam-like structures.

**Bending waves:** The stresses and strains associated with bending or flexural waves act in the longitudinal direction. Nevertheless, bending induces in the structure transverse displacements  $w$ , with larger amplitude than waves previously introduced. In structure-borne sound transmission analysis it is important to consider the propagation of all these three kinds of wave, and their interaction. However, in sound radiation problems, due to their larger deflection, bending waves are by far of greater importance than quasi-longitudinal and shear waves. Unlike quasi-longitudinal and transverse waves, bending waves are dispersive. It means that the phase velocity is not constant, but depends on the frequency. The dispersion relation is derived in the next sections under different assumptions.

## 2.2 Bending waves in isotropic plates

The equation of motion of a vibrating plate can be derived using different approaches. The dynamic equilibrium approach, based on Newton's second law, or D'Alembert's principle, represents the most straightforward method when the system is excited by forces with a constant orientation, and the motion is restricted to a single plane. Although, when these conditions are not fulfilled, other approaches, such as variational method and integral equation formulation, introduced in Chapter 3, are more suitable. The solution of the equation of motion of a rectangular homogeneous isotropic thin plate, undergoing flexural vibrations, is derived in the next sections by following two distinct approaches. Moreover, the main differences between classical thin plate theory and Mindlin's theory for thick plates are recalled.

### 2.2.1 Thin plate theory

The equation of motion of a homogeneous isotropic rectangular thin plate, laying in the  $xy$  plane and undergoing flexural vibrations, can be described as a function of the transverse displacement  $w$  by using the classical plate theory, also known as Kirchhoff's theory. The differential equation of motion of a thin vibrating plate is derived under the following assumptions:

1. the plate's thickness  $h$  is small compared to its other dimensions.
2. the middle plane of the plate represents a neutral surface, therefore it does not undergo in-plane deformations,
3. the transverse displacement of the middle plane  $w$  is small compared to the plate thickness  $h$ ,
4. the influences of the transverse shear deformation is neglected,
5. the influence of the rotational inertia is neglected.

The thin plate's equation of motion for free and forced flexural vibration is given by:

$$D \left( \frac{\partial^4 w}{\partial x^4} + 2 \frac{\partial^4 w}{\partial x^2 \partial y^2} + \frac{\partial^4 w}{\partial y^4} \right) + \rho h \frac{\partial^2 w}{\partial t^2} = \begin{cases} 0; \\ f_e(x, y, t); \end{cases} \quad (2.3)$$

where  $f_e$  represents the external forces exciting the plate,  $\rho$  is the plate's density, and  $D$  its bending stiffness, defined as:

$$D = \frac{Eh^3}{12(1-\nu^2)}, \quad (2.4)$$

where  $E$  is the plate's elastic modulus, and  $\nu$  represents its Poisson's ratio.

Considering the homogeneous equation of motion for free vibration, a possible solution for the transverse displacement  $w$ , induced by a harmonic plane bending wave, with amplitude  $\bar{w}$  and angular frequency  $\omega$ , that propagates along a direction  $\phi = \arctan(k_y/k_x)$  to the  $x$ -axis, can be written in the form:

$$w(x, y, t) = \bar{w} e^{i(\omega t - k_x x - k_y y)}, \quad (2.5)$$

where  $k_x$  and  $k_y$  are the components along the  $x$  and  $y$  directions of the the bending wavenumber  $k_B$ :

$$k_B = \sqrt{k_x^2 + k_y^2}. \quad (2.6)$$

The plane bending wave equation, obtained by substituting equation (2.5) into the unforced equation of motion (2.3), can be written omitting the time dependency as:

$$\left( Dk_B^4 - \rho h \omega^2 \right) \bar{w} = 0, \quad (2.7)$$

## 2.2. Bending waves in isotropic plates

---

which is satisfied for:

$$k_B = \sqrt{\omega} \sqrt[4]{\frac{\rho h}{D}}. \quad (2.8)$$

The general solution of the unforced equation of motion can be written as:

$$w(x, y, t) = \left( \bar{w}_1 e^{ik_B(x \cos \phi + y \sin \phi)} + \bar{w}_2 e^{k_B(x \cos \phi + y \sin \phi)} + \bar{w}_3 e^{-ik_B(x \cos \phi + y \sin \phi)} + \bar{w}_4 e^{-k_B(x \cos \phi + y \sin \phi)} \right) e^{i\omega t}. \quad (2.9)$$

The solution part with complex wavenumbers  $\bar{w}_1 e^{ik_B(\dots)} e^{i\omega t} + \bar{w}_3 e^{-ik_B(\dots)} e^{i\omega t}$  represents propagating waves, where the sign of the exponential indicates the propagation direction. The solutions with a real exponential represent the so-called near-field vibrations, which might occur at the discontinuities, such as the plate's boundaries, or the excitation point. The exponentially decaying contribution of these evanescent waves is usually considered negligible at a distance equal or greater than half wavelength from the discontinuity. The phase velocity  $c_B$ , of a bending wave freely propagating in a homogeneous isotropic thin plate, is given by:

$$c_B = \frac{\omega}{k_B} = \sqrt{\omega} \sqrt[4]{\frac{D}{\rho h}}. \quad (2.10)$$

Equation (2.10), known as the thin plate dispersion relation, shows that the bending wave velocity is not constant, but increases with frequency. The bending wave velocity plays a key role in sound radiation mechanisms, as will be explained in Chapter 3.

The envelope function of a train of bending waves, with a different wavelength, is defined by the group velocity  $c_g$ :

$$c_g = \frac{d\omega}{dk_B}. \quad (2.11)$$

The group velocity is the speed at which the energy propagates, and it is helpful in the evaluation of the vibrational field by means of a statistical approach, which is often applied in vibro-acoustic analysis at high frequencies. The relationship between the phase and the group velocity depends on the dispersion of the waves in a given elastic medium: the phase velocity can be equal, greater, or less than the group velocity [49]. From equations (2.8) and (2.11) it is possible to express the group velocity of pure bending waves propagating in a plate as:

$$c_{g,B} = 2k_B \sqrt[4]{\frac{D}{\rho h}} = 2c_B, \quad (2.12)$$

under the thin plate theory the bending group velocity is thus double the phase velocity.



### 2.2.2 Modal approach solution

The real part of equation (2.9) represents the amplitude of the thin plate's transverse displacement due to free bending vibration. The approach followed for its derivation is particularly useful to understand important concepts, such as free bending wavenumber, dispersion relation, and propagating and evanescent waves. However, it might be helpful to introduce an alternative approach, based on modal analysis, to solve the unforced equation of motion (2.3). Assuming a harmonic dependence of time, the field variables can be separated as:

$$w(x, y, t) = \mathcal{F}(x, y) e^{i\omega t}, \quad (2.13)$$

where  $\mathcal{F}(x, y)$  is an unknown function of the spatial coordinates. By substituting this expression for transverse displacement into the homogeneous equation of motion, one can reformulate the differential equation as a standard eigenvalue problem:

$$\left(\nabla^4 - k_B^4\right) \mathcal{F}(x, y) = 0, \quad (2.14)$$

where  $\nabla^4$  is known as biharmonic operator. In Cartesian coordinates it has the form of:

$$\nabla^4 = \frac{\partial^4}{\partial x^4} + 2 \frac{\partial^2}{\partial x^2 \partial y^2} + \frac{\partial^2}{\partial y^2}.$$

One solution of the standard eigenvalue problem, given in equation (2.14), can be expressed as:

$$\begin{aligned} \mathcal{F}(x, y) = & A_1 \sin k_x x \sin k_y y + A_2 \sin k_x x \cos k_y y \\ & + A_3 \cos k_x x \sin k_y y + A_4 \cos k_x x \cos k_y y \\ & + A_5 \sinh k_x x \sinh k_y y + A_6 \sinh k_x x \cosh k_y y \\ & + A_7 \cosh k_x x \sinh k_y y + A_8 \cosh k_x x \cosh k_y y. \end{aligned} \quad (2.15)$$

To determine the value of the real constants  $A_1$ – $A_8$  it is necessary to consider the plate's boundary conditions. Assuming the plate to be simply-supported on the four edges, the boundary conditions are expressed as:

$$w|_{x=0, L_x} = 0; \quad \frac{\partial^2 w}{\partial x^2} \Big|_{x=0, L_x} = 0; \quad w|_{y=0, L_y} = 0; \quad \frac{\partial^2 w}{\partial y^2} \Big|_{y=0, L_y} = 0; \quad (2.16)$$

where  $L_x$  and  $L_y$  are the length and the width of the plate. For simply-supported boundaries a solution for the function  $\mathcal{F}(x, y)$  is given by:

$$\mathcal{F}(x, y) = A_1 \sin k_x x \sin k_y y. \quad (2.17)$$

The wavenumber components  $k_x$  and  $k_y$ , defined in the previous section, must satisfy:

$$\begin{aligned} k_x = k_m = \frac{m\pi}{L_x}; \\ k_y = k_n = \frac{n\pi}{L_y}; \end{aligned} \quad (2.18)$$

### 2.3. Influence of shear deformation and rotational inertia

---

where  $m$  and  $n$  are real positive integers, representing the modal index. From equations (2.8) and (2.18) it is possible to determine the natural frequency associated with each single natural mode:

$$\omega_{mn} = \left[ \left( \frac{m\pi}{L_x} \right)^2 + \left( \frac{n\pi}{L_y} \right)^2 \right] \sqrt{\frac{D}{\rho h}}, \quad (2.19)$$

and the mode shape function  $\psi_{mn}(x, y)$  of mode  $(m, n)$  is defined as:

$$\psi_{mn}(x, y) = \sin\left(\frac{m\pi x}{L_x}\right) \sin\left(\frac{n\pi y}{L_y}\right). \quad (2.20)$$

The orthogonality condition is satisfied, since:

$$\langle \psi_{mn}, \psi_{pq} \rangle = \int_0^{L_x} \int_0^{L_y} \psi_{mn} \psi_{pq} \, dx dy = \frac{L_x L_y}{2} \delta_{mn} \delta_{pq}, \quad (2.21)$$

where  $\delta_{ij}$  is the Kronecker delta, which is equal to 1 when  $i = j$  and equal to 0 otherwise. The general solution of the equation of motion (2.3) is given as a sum of a theoretically infinite number of natural modes:

$$w(x, y, t) = \sum_m \sum_n A_{mn} \psi_{mn} \sin(\omega_{mn} t + \varphi_{mn}). \quad (2.22)$$

The amplitude  $A_{mn}$ , that quantifies the contribution of the  $mn^{\text{th}}$  mode to the total response, and the phase shift  $\varphi_{mn}$ , are determined by applying the initial conditions of each specific problem.

### 2.3 Influence of shear deformation and rotational inertia

The thin plate theory neglects the effects of rotational inertia and shear deformation. In bending waves analysis, this approximation is generally valid when the plate's thickness is small compared to the bending wavelength. In other words, due to the dispersive nature of bending waves, the validity of the simple theory for thin plates is limited in frequency. A more sophisticated plate theory which considers rotational inertia and shear deformation was developed by Mindlin [50], extending Timoshenko beam theory. The equation of motion for free vibration under Mindlin's theory is given by [51, 52]:

$$D \nabla^4 w - \left[ \frac{\rho D}{\kappa^2 G} + I \right] \nabla^2 \frac{\partial^2 w}{\partial t^2} + \rho \frac{I}{\kappa^2 G} \frac{\partial^4 w}{\partial t^4} + \rho h \frac{\partial^2 w}{\partial t^2} = 0; \quad (2.23)$$

while it can be expressed, by taking into account an external force  $f_e(x, y, t)$ , as:

$$\begin{aligned} D \nabla^4 w - \left[ \frac{\rho D}{\kappa^2 G} + I \right] \nabla^2 \frac{\partial^2 w}{\partial t^2} + \rho \frac{I}{\kappa^2 G} \frac{\partial^4 w}{\partial t^4} + \rho h \frac{\partial^2 w}{\partial t^2} \\ = \left( 1 - \frac{D}{h \kappa^2 G} + \frac{I}{h \kappa^2 G} \frac{\partial^2}{\partial t^2} \right) f_e(x, y, t). \end{aligned} \quad (2.24)$$

### 2.3. Influence of shear deformation and rotational inertia

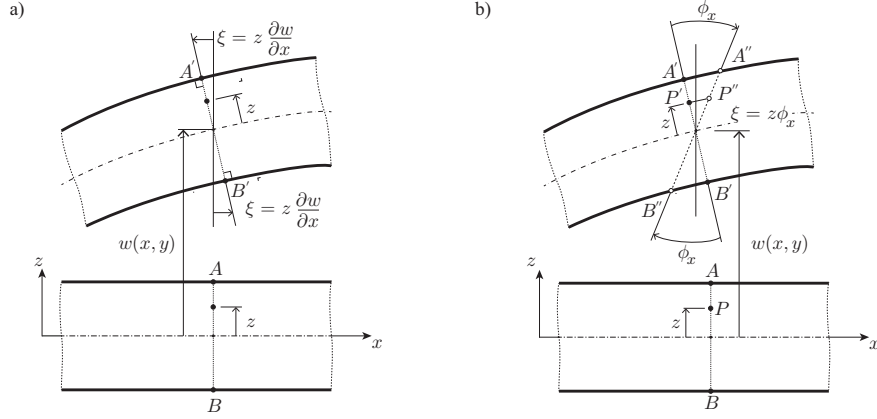


Figure 2.1: Bending waves deformation: differences between Kirchhoff's theory for thin plates a), and Mindlin's theory for thick plates b)

It should be noticed that when the mass moment of inertia of the plate  $I = \rho h^3/12$  is neglected, and the shear modulus  $G$  is assumed infinite, this equation turns into the equation of motion of a thin plate, given in equation (2.3). The coefficient  $\kappa^2$ , similar to the Timoshenko shear coefficient in thick beam theory [53], takes into account that the shear stress is not constant over the plate thickness. According to Ref. [54], it can be approximated using a simple relationship that follows from some considerations about the bending wave velocity limit of large wavenumbers:

$$\kappa = \frac{c_R}{c_S} = \frac{0.87 + 1.12\nu}{1 + \nu}, \quad (2.25)$$

where  $c_S$  is the pure shear wave velocity and  $c_R$  represents the Rayleigh surface wave velocity.

The thin plate dispersion relation for pure bending derived in equation (2.10), shows an unlimited increase of the wave velocity with frequency. However, for large wavenumbers the velocity should be limited, due to rotational inertia and especially shear deformation effects. Under Mindlin's theory it is possible to derive the dispersion relation of a flexural wave, by taking into account these effects [49]:

$$\left(1 - \frac{c^2}{\kappa^2 c_T^2}\right) \left(\frac{c_L^2}{c_T^2} - 1\right) = \frac{12}{h^2 \left(\frac{\omega}{c}\right)^2}, \quad (2.26)$$

where  $c$  represents the velocity of the structural wave propagating in the plate, while  $c_L$  and  $c_T$  are the longitudinal and the pure shear wave velocity, given in equations (2.1) and (2.2).

According to Mindlin's theory, at high frequencies the flexural wave velocity approaches the Rayleigh surface velocity  $c_R = \kappa c_T$ . A comparison

### 2.3. Influence of shear deformation and rotational inertia

---

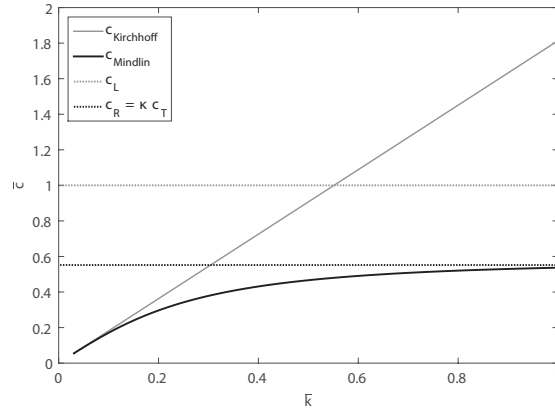


Figure 2.2: Comparison between flexural wave dispersion curves, derived under Kirchhoff's and Mindlin's theory. The normalised wave velocity:  $\bar{c} = c/c_L$  is plotted against the normalised wavenumber:  $\bar{k} = kh/2\pi$ . Recreated from Ref. [49].

between thin and thick plate dispersion relations is given in Figure 2.2. From an acoustic point of view, the effect of rotational inertia and shear deformation starts to be significant when the structural wave length is approximately six times smaller than the plate thickness  $\lambda_B < 6h$  [41]. This condition, sometimes expressed in terms of Helmholtz number as  $k_B h \geq 1$  [55], represents the frequency limit above which longitudinal waves associated with thickness resonances, known as dilatational waves, radiate sound efficiently [56].

## Chapter 3

# Sound radiated from orthotropic plates

### 3.1 Introduction

Sound radiation from vibrating structures is a topic of main interest in many fields of acoustics, both for sound insulation and noise control aspect, and, with an opposite purpose, also for speaker and monitor design. In order to design and optimise structures to provide good sound insulation it is fundamental to characterise how a vibrating element radiates sound. This has been object of an increasing interest during the last half century and the physic behind this mechanism is well known. However, from an engineering point of view, the rigorous computation of the sound power radiated by a vibrating surface is still a highly demanding task. In this Chapter the basic concepts of sound radiation by flexural vibration in plates are recalled, and two different models, developed to estimate the radiation efficiency of an orthotropic plate, are presented. The main purpose has been to implement prediction models, helpful tools for engineers and architects in the acoustic design of cross-laminated timber building partitions. Cross laminated plates are sometimes treated as layered structures, although the main idea of this research project was to analyse these elements as equivalent homogeneous orthotropic plates, by using frequency dependent apparent elastic properties. Frequency-dependent apparent material parameters are commonly used to model the dynamics of complex elements, such as sandwich beams or plates, by means of simplified theories, developed for homogeneous structures [57]. While a complete and thorough analysis of plate dynamics and sound radiation can be found in specific textbooks, see for example Ref. [51, 58] and Ref. [59, 60], in this Chapter the stress and strain relationship of orthotropic elastic materials are firstly recalled. The fundamental equations of motion governing flexural vibration of orthotropic thin plates are derived, both considering the in-vacuum condition, and the structure immersed in a fluid.

### 3.2. Orthotropic elastic solids

---

A variational approach based on Hamilton's principle follows, considering external excitations of different nature. The sound radiation model presented in Ref. [16] for isotropic plates has been extended, deriving an analytic model for orthotropic thin plates. The influence of fluid loading on the plate response is discussed, and an approximation of the radiation impedance with the self-radiation resistance is introduced. The modal summation approach presented by Xie et al. [19], is also introduced. Since this model has been already applied to orthotropic structures by Venini [61], providing reliable results, it has been used as basis for comparison with the analytic model. The concepts of resonant and non-resonant radiation are introduced, and the modal-average radiation efficiency for an orthotropic thin plate is derived, based on the work of Anderson and Bratos-Anderson [30]. The effect of vibrational near-field, and non-resonant field are finally discussed.

### 3.2 Orthotropic elastic solids

Considering a rectangular orthotropic plate, laying in the  $xy$  plane, with the principal directions of orthotropy aligned with the axes, as shown in Figure 3.1, it is possible to express the stress and strain relationship as a function of nine independent constants: three elastic moduli  $E_i$  and the Poisson's ratios  $\nu_{ij}$ , associated with the three principle orthotropic directions, and three shear moduli  $G_{ij}$ . The compliance matrix, in terms of the engineering strain and stress components, and material constants, is given as:

$$\begin{Bmatrix} \varepsilon_x \\ \varepsilon_y \\ \varepsilon_z \\ \gamma_{xy} \\ \gamma_{xz} \\ \gamma_{yz} \end{Bmatrix} = \begin{bmatrix} \frac{1}{E_x} & -\frac{\nu_{yx}}{E_y} & -\frac{\nu_{zx}}{E_z} & 0 & 0 & 0 \\ -\frac{\nu_{xy}}{E_x} & \frac{1}{E_y} & -\frac{\nu_{zy}}{E_z} & 0 & 0 & 0 \\ -\frac{\nu_{xz}}{E_x} & -\frac{\nu_{yz}}{E_y} & \frac{1}{E_z} & 0 & 0 & 0 \\ 0 & 0 & 0 & \frac{1}{G_{xy}} & 0 & 0 \\ 0 & 0 & 0 & 0 & \frac{1}{G_{xz}} & 0 \\ 0 & 0 & 0 & 0 & 0 & \frac{1}{G_{yz}} \end{bmatrix} \begin{Bmatrix} \sigma_x \\ \sigma_y \\ \sigma_z \\ \tau_{xy} \\ \tau_{xz} \\ \tau_{yz} \end{Bmatrix}. \quad (3.1)$$

However, under the thin plate assumptions, discussed in the previous section, a plane stress condition is considered by taking  $\sigma_z = 0$  and  $\gamma_{xz} = \gamma_{yz} = 0$ . Thus the stress and strain relationship matrix given in equation (3.1) reduces to:

$$\begin{Bmatrix} \varepsilon_x \\ \varepsilon_y \\ \gamma_{xy} \end{Bmatrix} = \begin{bmatrix} \frac{1}{E_x} & -\frac{\nu_{yx}}{E_y} & 0 \\ -\frac{\nu_{xy}}{E_x} & \frac{1}{E_y} & 0 \\ 0 & 0 & \frac{1}{G_{xy}} \end{bmatrix} \begin{Bmatrix} \sigma_x \\ \sigma_y \\ \tau_{xy} \end{Bmatrix}. \quad (3.2)$$

### 3.3. Derivation of the basic equations

---

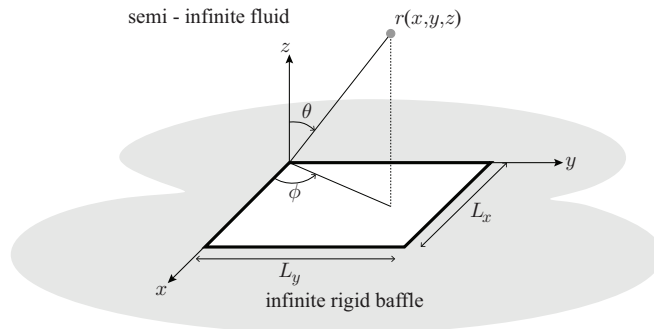


Figure 3.1: Elastic thin orthotropic plate inserted in a infinite rigid baffle, radiating sound energy in a semi-infinite fluid domain  $z > 0$ .

It is possible to express the strain components in terms of the plate's transverse displacement  $w$  as:

$$\begin{cases} \varepsilon_x = \frac{\partial \xi}{\partial x} = -z \frac{\partial^2 w}{\partial x^2}; \\ \varepsilon_y = \frac{\partial \zeta}{\partial y} = -z \frac{\partial^2 w}{\partial y^2}; \\ \gamma_{xy} = \frac{\partial \xi}{\partial x} + \frac{\partial \zeta}{\partial y} = -2z \frac{\partial^2 w}{\partial x \partial y}; \end{cases} \quad (3.3)$$

where  $\xi$  and  $\zeta$  represent the longitudinal in-plane displacement along the  $x$  and  $y$  axes respectively.

## 3.3 Derivation of the basic equations

### 3.3.1 In-vacuum vibration

Although the equation of motion of a thin orthotropic plate can be easily derived through the equilibrium approach, for sound radiation analysis it might be useful to derive it in terms of energy, by means of Hamilton's principle: a variational method to determine the dynamics of a system. Hamilton's principle analyses the motion of a mechanical system, between two instants  $t_1$  and  $t_2$ , as a path traced in a  $n$ -dimensional space, called *configuration space*.

$$\mathcal{H}(w) = \int_{t_1}^{t_2} \mathcal{L} dt = \int_{t_1}^{t_2} (\mathcal{T} - \mathcal{V} + \mathcal{W}_e) dt. \quad (3.4)$$

### 3.3. Derivation of the basic equations

---

The *Lagrangian* function,  $\mathcal{L}$ , is defined from the strain  $\mathcal{V}$  and kinetic  $\mathcal{T}$  energy and the work of external forces  $\mathcal{W}_e$ . For a conservative system, Hamilton's principle states that, among all the possible paths, the one that represents the true evolution of the system, within the interval  $t_1 - t_2$ , is such that the variation of the *Hamiltonian* functional  $\mathcal{H}$  is zero:

$$\delta \mathcal{H}(w) = \delta \int_{t_1}^{t_2} \mathcal{L} dt = 0, \quad (3.5)$$

where  $\delta$  represents the variational operator, which can be considered as the total derivative operator assuming the time to be constant. A more detailed analysis on variational methods, Hamilton's principle, and calculus techniques, can be easily found in Ref. [51, 62].

The strain energy of an elastic solid structure is defined by the product of stresses and strains integrated over the volume  $V$  of the element; for the orthotropic thin plate undergoing bending vibration it is given by:

$$\mathcal{V} = \frac{1}{2} \iiint_V (\sigma_x \varepsilon_x + \sigma_y \varepsilon_y + \tau_{xy} \gamma_{xy}) dV. \quad (3.6)$$

From the stress and strain relationship, given in equation (3.3), the stress components are given by:

$$\begin{cases} \sigma_x = \frac{E_x}{1 - \nu_{xy}\nu_{yx}} (\varepsilon_x + \nu_{yx}\varepsilon_y); \\ \sigma_y = \frac{E_y}{1 - \nu_{xy}\nu_{yx}} (\varepsilon_y + \nu_{xy}\varepsilon_x); \\ \tau_{xy} = G_{xy}\gamma_{xy}; \end{cases} \quad (3.7)$$

while the strain components can be expressed as a function of the transverse displacement  $w$  according to the relationships given in equations (3.2) as:

$$\begin{aligned} \mathcal{V} = \frac{1}{2} & \left\{ \frac{E_x}{1 - \nu_{xy}\nu_{yx}} \int_0^{L_x} \int_0^{L_y} \left[ \left( \frac{\partial^2 w}{\partial x^2} \right)^2 + \nu_{yx} \frac{\partial^2 w}{\partial x^2} \frac{\partial^2 w}{\partial y^2} \right] dx dy \right. \\ & + \frac{E_y}{1 - \nu_{xy}\nu_{yx}} \int_0^{L_x} \int_0^{L_y} \left[ \left( \frac{\partial^2 w}{\partial y^2} \right)^2 + \nu_{xy} \frac{\partial^2 w}{\partial x^2} \frac{\partial^2 w}{\partial y^2} \right] dx dy \\ & \left. + 4G_{xy} \int_0^{L_x} \int_0^{L_y} \left( \frac{\partial^2 w}{\partial x \partial y} \right)^2 dx dy \right\} \int_{-h/2}^{h/2} z^2 dz, \end{aligned} \quad (3.8)$$

or in terms of the bending stiffness along the principle orthotropic directions



### 3.3. Derivation of the basic equations

---

$D_x$ ,  $D_y$  as:

$$\begin{aligned} \mathcal{V} = & \frac{D_x}{2} \int_0^{L_x} \int_0^{L_y} \left[ \left( \frac{\partial^2 w}{\partial x^2} \right)^2 + \nu_{yx} \frac{\partial^2 w}{\partial x^2} \frac{\partial^2 w}{\partial y^2} \right] dx dy \\ & + \frac{D_y}{2} \int_0^{L_x} \int_0^{L_y} \left[ \left( \frac{\partial^2 w}{\partial y^2} \right)^2 + \nu_{xy} \frac{\partial^2 w}{\partial x^2} \frac{\partial^2 w}{\partial y^2} \right] dx dy \\ & + 2G_{xy} \frac{h^3}{12} \int_0^{L_x} \int_0^{L_y} \left( \frac{\partial^2 w}{\partial x \partial y} \right)^2 dx dy. \end{aligned} \quad (3.9)$$

If rotational inertia effect is neglected, the kinetic energy of the plate is defined as the product of the square vibration velocity and the material density integrated over the volume:

$$\mathcal{T} = \frac{1}{2} \iiint_V \rho \left( \frac{\partial w}{\partial t} \right)^2 dV = \frac{\rho h}{2} \int_0^{L_x} \int_0^{L_y} \left( \frac{\partial w}{\partial t} \right)^2 dx dy. \quad (3.10)$$

The work done by an external force  $f_e(x, y, 0, t)$ , acting on the plate surface, is defined as:

$$\mathcal{W}_e = \int_0^{L_x} \int_0^{L_y} f_e w dx dy. \quad (3.11)$$

Hamilton's principle can be written by substituting equations (3.9), (3.10), and (3.11) into equation (3.5). Solving the resulting integral will lead to the equation of motion of an orthotropic thin plate and to the equations associated with all the possible boundary conditions. The equation of motion of a thin orthotropic plate undergoing flexural vibrations is governed by the differential equation [58]:

$$D_x \frac{\partial^4 w}{\partial x^4} + 2B \frac{\partial^4 w}{\partial x^2 \partial y^2} + D_y \frac{\partial^4 w}{\partial y^4} + \rho h \frac{\partial^2 w}{\partial t^2} = \begin{cases} 0; \\ f_e(x, y, t); \end{cases} \quad (3.12)$$

where the bending stiffness along the principal directions,  $D_x$  and  $D_y$ , and the effective torsional stiffness  $B$ , are function of the elastic moduli  $E_x$  and  $E_y$ , and the in-plane shear modulus  $G_{xy}$ :

$$D_x = \frac{E_x h^3}{12(1 - \nu_{xy}\nu_{yx})}; \quad D_y = \frac{E_y h^3}{12(1 - \nu_{xy}\nu_{yx})}; \quad (3.13)$$

$$B = \frac{\nu_{yx} D_x}{2} + \frac{\nu_{xy} D_y}{2} + 2G_{xy} \frac{h^3}{12}. \quad (3.14)$$

According to Betti's reciprocal theorem the bending stiffnesses along the two principle directions satisfy the relationship [63, 64]:

$$\nu_{yx} D_x = \nu_{xy} D_y. \quad (3.15)$$

The Poisson's ratios  $\nu_{xy}$  and  $\nu_{yx}$  represent the elastic constants related to the geometrical configuration of the orthotropic plate.

### 3.3.2 Plate immersed in a fluid

The fluid-structure interaction, in some cases, might influence the structural dynamic response significantly [41, 60, 59], therefore, the vibro-acoustic analysis should also take into account the acoustic load of the fluid the plate is immersed into, other than the external forces acting on the plate. For the baffle condition we consider the fluid load effect only on the radiating side. For  $z > 0$ , the forced equation of motion considering the acoustic loading is given by:

$$D_x \frac{\partial^4 w}{\partial x^4} + 2B \frac{\partial^4 w}{\partial x^2 \partial y^2} + D_y \frac{\partial^4 w}{\partial y^4} + \rho h \frac{\partial^2 w}{\partial t^2} = f_e(x, y, t) - p(x, y, 0, t). \quad (3.16)$$

The work done by the acoustic pressure  $p(x, y, z)$  acting on the plate surface in the the semi-infinite fluid domain  $z > 0$ , is given by:

$$\mathcal{W}_f = \int_0^{L_x} \int_0^{L_y} p(x, y, 0) w(x, y) \, dx dy. \quad (3.17)$$

The acoustic pressure satisfies the Helmholtz equation (3.18a), and the continuity condition of the acoustic particle velocity and the mechanical vibration velocity must be fulfilled both on the interfaces fluid domain–plate surface (3.18b), and fluid–baffle (3.18c). Moreover, in the fluid domain  $z > 0$  Sommerfeld radiation condition at infinity, given in equation (3.18d), has to be satisfied [65]. Therefore, this radiation problem is governed by the equations:

$$\left( \nabla^2 + k_0^2 \right) p(r) = 0; \quad (3.18a)$$

$$\left. \frac{\partial p(r)}{\partial n_r} \right|_{plate} = \rho_0 \omega^2 w(r); \quad (3.18b)$$

$$\left. \frac{\partial p(r)}{\partial n_r} \right|_{baffle} = 0; \quad (3.18c)$$

$$\lim_{r \rightarrow \infty} \left[ r \left( \frac{\partial p(r)}{\partial r} - ik_0 p(r) \right) \right] = 0; \quad (3.18d)$$

indicating with  $r(x, y, 0)$  a point on the plate surface and with  $n_r$  the outward normal to the plate surface. The acoustic pressure in the fluid domain  $p(r)$  can be determined by using the integral formulation method. To this purpose it is necessary to derive a suitable Green's function  $G(r, \bar{r})$ , describing the sound pressure in a point of the fluid domain  $r(x, y, z)$ , due to a monopole source located in  $\bar{r}(\bar{x}, \bar{y}, \bar{z})$ . The Green's function for the semi-infinite free space is commonly used to simplify this kind of exterior baffled problem [66]:

$$G(r, \bar{r}) = \frac{e^{ik_0|r-\bar{r}|}}{2\pi|r-\bar{r}|}. \quad (3.19)$$

### 3.4. Analytical sound radiation model

---

It is possible to write the Kirchhoff-Helmholtz integral over the plate surface  $S$  to describe the acoustic pressure as:

$$p(\bar{r}) = \iint_S \left[ \frac{\partial G(r, \bar{r})}{\partial n_r} p(r) - \frac{\partial p(r)}{\partial n_r} G(r, \bar{r}) \right] dS. \quad (3.20)$$

The derivative of the semi-infinite space Green's function is zero, both on the baffle and on the plate surface, therefore, the equation (3.20) can be simplified as:

$$p(\bar{r}) = - \iint_S \frac{\partial p(r)}{\partial n_r} G(r, \bar{r}) dS, \quad (3.21)$$

obtaining the well-known Rayleigh's integral [6]. The acoustic pressure on the plate surface is thus defined as  $p(x, y, 0) = -p(\bar{x}, \bar{y}, 0)$ . Considering the continuity condition on the plate-fluid interface, expressed in equation (3.18b), the work associated with the fluid loading can be rewritten as a four-fold integral over the plate surface  $S$ :

$$\mathcal{W}_f = \rho_0 \omega^2 \iiint_S \iiint_S w(x, y) G(x, y, 0; \bar{x}, \bar{y}, 0) w(\bar{x}, \bar{y}) d\bar{x} d\bar{y} dx dy. \quad (3.22)$$

It can also be expressed as a function of the plate's radiation impedance  $Z$  as:

$$\mathcal{W}_f = -i\omega Z w, \quad (3.23)$$

defining the radiation impedance as:

$$Z = i\rho_0 \omega^2 \iiint_S \iiint_S w(x, y) G(x, y, 0; \bar{x}, \bar{y}, 0) w(\bar{x}, \bar{y}) dS dS. \quad (3.24)$$

The *Hamiltonian* functional can be formulated by considering both the work associated with the external forces and the work associated with the fluid acoustic pressure as:

$$\mathcal{H}(w) = \int_{t_1}^{t_2} (\mathcal{T} - \mathcal{V} + \mathcal{W}_e + \mathcal{W}_f) dt. \quad (3.25)$$

In the next section, a solution of equation (3.25) for the transverse displacement  $w$  will be sought, in order to determine the vibro-acoustic descriptors of the orthotropic plate.

## 3.4 Analytical sound radiation model

The solution for the transverse displacement  $w$  of the orthotropic plate can be derived following the generalised approach proposed by Nelisse [16] to evaluate the sound power radiated by rectangular isotropic plates immersed

### 3.4. Analytical sound radiation model

---

in a fluid. An approximate solution of the *Hamiltonian* functional can be determined through the Rayleigh-Ritz method. The plate transverse displacement  $w(x, y, t)$  can be approximated as a linear sum of admissible functions, separating the spatial and the temporal variables, analogous to what has been done in equation (2.13) for an isotropic plate.

$$w(x, y, t) = \sum_m^M \sum_n^N a_{mn} \psi_{mn}(x, y) e^{i\omega t}, \quad (3.26)$$

where  $a_{mn}$  represents the unknown amplitude of the transverse displacement associated with the mode  $(m, n)$ . The functions  $\psi_{mn}(x, y)$  depend only on the spatial coordinates and can be chosen as polynomial [10, 67], or trigonometric functions [68], satisfying the geometric boundary conditions. The *Hamiltonian* functional can be reformulated by substituting in the *Lagrangian*  $\mathcal{L}$  the transverse displacement  $w$ , expanded over the admissible functions given in equation (3.26). After some algebraic manipulations the Lagrange equations can be written as [65]:

$$\frac{d}{dt} \frac{\partial \mathcal{T}}{\partial a_{mn}} + \frac{\partial \mathcal{V}}{\partial a_{mn}} = \frac{\partial \mathcal{W}_e}{\partial a_{mn}} + \frac{\partial \mathcal{W}_f}{\partial a_{mn}}. \quad (3.27)$$

Assuming a harmonic time dependence of the kind  $e^{i\omega t}$ , it is possible to write the orthotropic plate's equation of motion, for a given angular frequency  $\omega$ , as a linear matrix system:

$$\left( -\omega^2 [M_{mnpq}] + [K_{mnpq}] + i\omega [Z_{mnpq}] \right) \{a_{mn}\} = \{f_{e,mn}\}, \quad (3.28)$$

where  $M_{mnpq}$  are the mass matrix coefficients,  $K_{mnpq}$  the stiffness matrix coefficients,  $Z_{mnpq}$  are the coefficients of the impedance matrix, and  $\{f_{e,mn}\}$  is the vector of the external force coefficients. The vector  $\{a_{mn}\}$  is the magnitude of the transverse displacement, which represents the only unknown of the system.

#### 3.4.1 Mass matrix coefficients

Assuming a simply supported boundary condition, sine functions can be used as trial functions, providing numerical stability in the computation [69]. Hence, the admissible functions  $\psi_{mn}(x, y)$  are represented by the plate's mode shapes given in equation (2.20). The generalised mass matrix coefficients for an orthotropic plate, do not differ from the isotropic case, and are given by:

$$M_{mnpq} = \rho h \int_0^{L_x} \int_0^{L_y} \psi_{mn}(x, y) \psi_{pq}(x, y) dx dy. \quad (3.29)$$

### 3.4. Analytical sound radiation model

---

Due to the orthogonality property of the admissible functions, expressed in equation (2.21), the mass matrix is diagonal, and equation (3.29) reduces to:

$$M_{mnpq} = \begin{cases} M_{mn} = \frac{\rho h L_x L_y}{4}, & \text{if } m = p \text{ and } n = q; \\ 0, & \text{if } m \neq p \text{ or } n \neq q. \end{cases} \quad (3.30)$$

#### 3.4.2 Stiffness matrix coefficients

The stiffness matrix  $\mathbf{K}$  of the orthotropic plate is defined as a function of the transverse displacement  $w(x, y, t)$  as:

$$K = \iint_S \left[ D_x \left( \frac{\partial^2 w}{\partial x^2} \right)^2 + D_y \left( \frac{\partial^2 w}{\partial y^2} \right)^2 + \nu_{yx} D_x \frac{\partial^2 w}{\partial x^2} \frac{\partial^2 w}{\partial y^2} + \nu_{xy} D_y \frac{\partial^2 w}{\partial y^2} \frac{\partial^2 w}{\partial x^2} + 4G_{xy} \frac{h^3}{12} \left( \frac{\partial^2 w}{\partial x \partial y} \right)^2 \right] dS. \quad (3.31)$$

The coefficients of the generalised matrix are computed by expressing the transverse displacements in terms of admissible functions, as given in equation (3.26), assuming a harmonic time dependence:

$$K_{mnpq} = \int_0^{L_y} \int_0^{L_y} \left[ D_x \frac{\partial^2}{\partial x^2} \psi_{mn}(x, y) \frac{\partial^2}{\partial x^2} \psi_{pq}(x, y) + D_y \frac{\partial^2}{\partial y^2} \psi_{mn}(x, y) \frac{\partial^2}{\partial y^2} \psi_{pq}(x, y) + \nu_{yx} D_x \frac{\partial^2}{\partial x^2} \psi_{mn}(x, y) \frac{\partial^2}{\partial y^2} \psi_{pq}(x, y) + \nu_{xy} D_y \frac{\partial^2}{\partial y^2} \psi_{mn}(x, y) \frac{\partial^2}{\partial x^2} \psi_{pq}(x, y) + 4G_{xy} \frac{h^3}{12} \frac{\partial^2}{\partial x \partial y} \psi_{mn}(x, y) \frac{\partial^2}{\partial x \partial y} \psi_{pq}(x, y) \right] dS. \quad (3.32)$$

The computation of the double-fold integral is still a computationally demanding task even for modern processors. However, under the assumption of simply supported boundary conditions, it was possible to reduce the integral equation to a simpler formulation, derived in Annex A.

#### 3.4.3 Radiation impedance matrix coefficients

The radiation impedance  $\mathbf{Z}$  is a sparse matrix of complex numbers. Its coefficients can be expressed in terms of real and imaginary part: the plate's radiation resistance  $R$  and radiation reactance  $X$  respectively:

$$Z_{mnpq} = R_{mnpq} + iX_{mnpq}. \quad (3.33)$$

### 3.4. Analytical sound radiation model

---

The rigorous computation of the radiation impedance coefficients involves a four-fold integral to be solved:

$$Z_{mnpq} = i\omega\rho_0 \int_0^{L_x} \int_0^{L_y} \int_0^{L_x} \int_0^{L_y} \psi_{mn}(x, y) G(x, y, 0, \bar{x}, \bar{y}, 0) \psi_{pq}(\bar{x}, \bar{y}) d\bar{x}d\bar{y}dxdy. \quad (3.34)$$

However, equation (3.34) can be reduced to a two-fold integral using the approach proposed by Sandman [13] and Nelisse [16], as shown in Annex B

#### 3.4.4 Excitation coefficients

In vibro-acoustic problems one needs to consider different kinds of excitation, of both mechanical and acoustic nature. The simplest case to treat analytically is represented by a point-force acting perpendicular to the plate surface. Considering a point mechanical force, acting in the position of coordinates  $(x_0, y_0)$  with amplitude  $F_0$ , the coefficients of the generalised force are given by:

$$f_{e,mn} = F_0 \psi_{mn}(x_0, y_0). \quad (3.35)$$

Considering an acoustic plane wave incident on the plate surface at an angle  $\theta$  to the normal, due to the plate response, a reflected sound wave on the exciting side, and a radiated wave on the opposite side, are generated. Assuming the reflected wave to be decomposed in a wave radiated by the vibrating plate and a sound wave reflected by the motionless surface, the generalised force due to the acoustic excitation is given by [18, 69]:

$$f_{e,mn} = 2 \int_0^{L_x} \int_0^{L_y} p_b(x, y, 0) w(x, y) dx dy, \quad (3.36)$$

where the blocked sound pressure  $p_b$  is the superposition of incident and reflected plane waves with the plate assumed to be motionless:

$$p_b(x, y, z, t) = e^{-ik_0(x \sin \theta \cos \phi + y \sin \theta \sin \phi - z \cos \theta)} e^{i\omega t}. \quad (3.37)$$

The acoustic pressure distribution is calculated for an incidence angle  $\theta$  to the normal of the plate, and an azimuthal angle  $\phi$  measured from the  $x$ -axis on the plate surface. For a simply supported boundaries the generalised force exciting the plate can be expressed as [70]:

$$f_{e,mn} = \frac{64 \left(\frac{m\pi}{L_x}\right)^2 \left(\frac{n\pi}{L_y}\right)^2}{\left[ (k_0 \sin \theta \sin \phi)^2 - \left(\frac{m\pi}{L_x}\right)^2 \right]^2 \left[ (k_0 \sin \theta \cos \phi)^2 - \left(\frac{m\pi}{L_x}\right)^2 \right]^2} \mathcal{S}, \quad (3.38)$$

### 3.4. Analytical sound radiation model

---

where the function  $\mathcal{S}$  depends on the modal indices:

$$\mathcal{S} = \begin{cases} \cos^2 \left( k_0 \sin \theta \sin \phi \frac{L_x}{2} \right) \cos^2 \left( k_0 \sin \theta \cos \phi \frac{L_y}{2} \right); & \text{odd-odd modes;} \\ \cos^2 \left( k_0 \sin \theta \sin \phi \frac{L_x}{2} \right) \sin^2 \left( k_0 \sin \theta \cos \phi \frac{L_y}{2} \right); & \text{odd-even modes;} \\ \sin^2 \left( k_0 \sin \theta \sin \phi \frac{L_x}{2} \right) \cos^2 \left( k_0 \sin \theta \cos \phi \frac{L_y}{2} \right); & \text{even-odd modes;} \\ \sin^2 \left( k_0 \sin \theta \sin \phi \frac{L_x}{2} \right) \sin^2 \left( k_0 \sin \theta \cos \phi \frac{L_y}{2} \right); & \text{even-even modes.} \end{cases} \quad (3.39)$$

When a diffuse sound field excites the plate surface different incident angles within the interval  $0 < \theta < \pi/2$ , other than different propagation angles  $0 < \phi < 2\pi$ , need to be considered. For each angular frequency  $\omega$ , the amplitude of the transverse displacement is given by:

$$a = \int_0^{\pi/2} \int_0^{2\pi} \omega^2 |a(\theta, \phi)|^2 d\phi d\theta. \quad (3.40)$$

#### 3.4.5 Vibro-acoustic indicators

Once the coefficients of the mass, stiffness, and radiation impedance matrix, and of the external force vector have been obtained, the vector of coefficients associated with the amplitude of the plate's transverse displacement  $a_{mn}$  can be computed by solving a set of linear algebraic equations:

$$a_{mn} = \mathcal{A}_{mnpq} f_{e,pq}, \quad (3.41)$$

where the admittance matrix  $\mathcal{A}$  is obtained from the inversion of the matrices between parentheses on the left hand side of equation (3.27) as:

$$[\mathcal{A}_{mnpq}] = \left( -\omega^2 [M_{mnpq}] + [K_{mnpq}] + i\omega [Z_{mnpq}] \right)^{-1}. \quad (3.42)$$

In order to numerically perform the matrix inversion it is necessary to rearrange the multi-dimensional matrices, i.e.  $\mathbf{M}$ ,  $\mathbf{K}$  and  $\mathbf{Z}$ , in two dimensions. For each angular frequency  $\omega$  the admittance matrix  $\mathcal{A}$  will result as:

$$[\mathcal{A}] = \begin{bmatrix} \mathcal{A}_{1,1,1,1} & \mathcal{A}_{1,2,1,1} & \cdots & \mathcal{A}_{1,n,1,1} & \cdots & \mathcal{A}_{m,n,1,1} \\ \mathcal{A}_{1,1,1,2} & \mathcal{A}_{1,2,1,2} & \cdots & \mathcal{A}_{1,n,1,2} & \cdots & \mathcal{A}_{m,n,1,2} \\ \vdots & \vdots & \ddots & \vdots & \vdots & \vdots \\ \mathcal{A}_{1,1,1,q} & \mathcal{A}_{1,2,1,q} & \cdots & \mathcal{A}_{1,n,1,q} & \cdots & \mathcal{A}_{m,n,1,q} \\ \vdots & \vdots & \vdots & \vdots & \ddots & \vdots \\ \mathcal{A}_{1,1,p,q} & \mathcal{A}_{1,2,p,q} & \cdots & \mathcal{A}_{1,n,p,q} & \cdots & \mathcal{A}_{m,n,p,q} \end{bmatrix}. \quad (3.43)$$

By solving the equation (3.41) it is possible to compute the vibro-acoustic indicators as a function of the plate's transverse displacement  $w$ . The mean square vibration velocity of the plate is given by:

$$\langle v^2 \rangle = \frac{\omega^2}{2S} \iint_S |w(r)|^2 dS = \frac{\omega^2}{8} \sum_m \sum_n |a_{mn}|^2. \quad (3.44)$$

### 3.5. Influence of fluid loading

---

The radiated sound power is computed by integrating the active sound intensity over the plate surface:

$$W_{rad} = \frac{1}{2} \iint_S \operatorname{Re} [i\omega w(\bar{r}) p(\bar{r})] dS = \frac{\omega^2}{2} \sum_m \sum_n \sum_p \sum_q a_{mn} \operatorname{Re} [Z_{mnpq}] a_{pq}^*, \quad (3.45)$$

where the superscript \* denotes the complex conjugate value.

The radiation efficiency  $\sigma$  is an important acoustic descriptor that characterises the capability of a vibrating structure to radiate sound.

$$\sigma = \frac{W_{rad}}{\rho_0 c_0 S \langle v^2 \rangle_{s,t}}. \quad (3.46)$$

It is defined as the ratio between the sound power actually radiated by a vibrating elastic structure  $W_{rad}$  and the sound power that would be theoretically radiated by a rigid piston of equal surface  $S$ , vibrating with the same mean square velocity  $\langle v^2 \rangle_{s,t}$ . The notation  $\langle \rangle_{s,t}$  indicates time and spatial average. For this reason it can be sometimes more accurately defined radiation ratio.

### 3.5 Influence of fluid loading

It is worth discussing some general considerations about the self and cross radiation impedance. The radiation reactance and resistance for different modes of a simply supported rectangular plate are plotted against the frequency in Figure 3.2, normalised with respect to the fluid acoustic impedance  $Z_0 = \rho_0 c_0$ . When the radiation of each single mode is considered, the diagonal coefficients  $Z_{mnmn}$  of the radiation impedance matrix are represented by the self-radiation resistance and reactance, which take positive values in the entire frequency range. The self-radiation reactance becomes negligible as the frequency increases, while the self-radiation resistance tends asymptotically to the fluid acoustic impedance, Figure 3.2a). The off-diagonal matrix coefficients  $Z_{mnpq}$ , which consider the interaction of the modes  $(m, n)$  and  $(p, q)$ , can be analogously expressed in terms of cross-radiation resistance and reactance. In this case the coefficients assume positive or negative values oscillating around zero, as shown in Figure 3.2b). Many studies have been undertaken on the effects of the load of the fluid on the structural dynamic response and on the radiated sound power [71, 72, 73]. Evidence shows that when the vibrating plate is immersed in water, the fluid loading has a significant influence both on the dynamic response, for example by shifting the in-vacuum resonance frequencies, and on the radiated sound power too. Moreover, the angular dependence of wavenumbers, which characterises orthotropic plates, is increased but not distorted by the fluid loading [74]. It should be noted however, that in buildings, the fluid surrounding



### 3.5. Influence of fluid loading

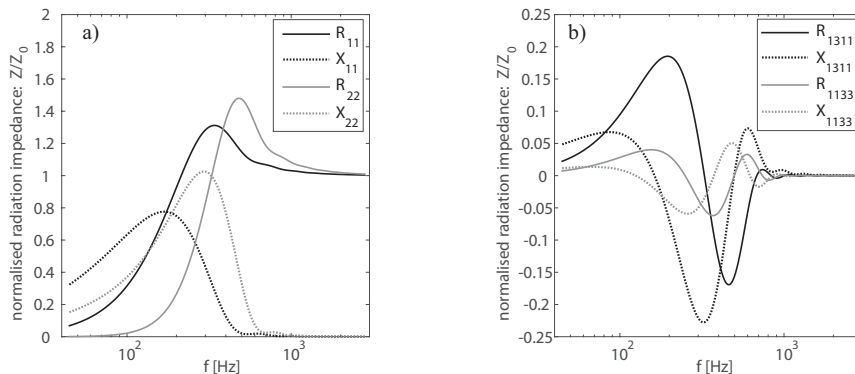


Figure 3.2: a) self radiation resistance  $R$  and reactance  $X$  of modes (1, 1) and (2, 2); b) cross radiation resistance  $R$  and reactance  $X$  of modes (1, 3) – (1, 1) and (1, 1) – (3, 3)

the radiating structures is air, which has a rather low inertia compared to building elements, and an acoustic impedance thousand times smaller than water. A general criterion to consider the light-fluid hypothesis was proposed by Innes and Crighton [75]:

$$\epsilon = \frac{\rho_0 c_0}{\rho h \omega_c} \ll 1, \quad (3.47)$$

where  $\omega_c$  is the critical angular frequency. In such a case, the influence of the fluid loading is thus very small and the radiation impedance might be approximated by the diagonal terms of the radiation resistance.

$$Z_{mnpq} \approx Z_{mn} \approx R_{mn}. \quad (3.48)$$

#### 3.5.1 Modal radiation efficiency

For each vibrational mode  $(m, n)$  a modal radiation efficiency  $\sigma_{mn}$  can be defined, which is proportional to the self radiation resistance  $R_{mn}$ :

$$\sigma_{mn} = \frac{W_{mn}}{\rho_0 c_0 S \langle v_{mn}^2 \rangle} = \frac{R_{mn}}{\rho_0 c_0 S n_{mn}}. \quad (3.49)$$

The modal radiation efficiency equals the self-radiation resistance normalised for the air impedance  $Z_0$ , the plate area  $S$ , and the norm of the mode  $n_{mn}$ . The first approximate formulae to evaluate the modal radiation efficiency

### 3.5. Influence of fluid loading

---

were proposed by Maidanik [8] in the early 1960s. Wallace derived an integral equation, based on the far-field acoustic intensity, to compute the modal radiation efficiency for a rectangular simply supported plate at any given frequency [76].

$$\sigma_{mn} = \frac{64k_0^2 L_x L_y}{\pi^6 m^2 n^2} \int_0^{\pi/2} \int_0^{\pi/2} \left\{ \frac{\cos\left(\frac{\alpha}{2}\right) \cos\left(\frac{\beta}{2}\right)}{\left[\left(\frac{\alpha}{m\pi}\right)^2 - 1\right] \left[\left(\frac{\beta}{n\pi}\right)^2 - 1\right]} \right\}^2 \sin\theta \, d\theta d\phi, \quad (3.50)$$

in which:

$$\begin{cases} \alpha = k_0 L_x \sin\theta \cos\phi; \\ \beta = k_0 L_x \sin\theta \sin\phi. \end{cases} \quad (3.51)$$

The function  $\cos(\alpha/2)$  is used if  $m$  is an odd integer while  $\sin(\alpha/2)$  if  $m$  is an even integer. The trigonometric functions with argument  $(\beta/2)$  are chosen analogously with respect to the integer  $n$ . The integration is performed over the bending wave propagation angle  $\phi$  and over the angle of propagation  $\theta$  of the radiated acoustic wave in the fluid medium. An alternative asymptotic formulation to compute the modal radiation efficiency was proposed by Leppington [77] for large acoustic and structural wavenumbers.

As discussed in the previous section, when the fluid that surrounds the structure is lightweight, the effects of its load can be neglected and the radiation impedance coefficients  $Z_{mnpq}$  can be approximated by the self radiation resistance coefficients, computed from the modal radiation efficiency  $\sigma_{mn}$ , according to equation (3.49). This approximation reduces drastically the computational cost of the analytical model to determine the radiation efficiency  $\sigma$  of an orthotropic plate.

#### 3.5.2 Modal summation approach

An alternative approach to evaluate the plate radiation efficiency by investigating single mode radiation, neglecting the cross-modal coupling, was presented by Xie, Thompson, and Jones for homogeneous isotropic baffle plates and strips (or plates with a large aspect ratio) [19]. Moreover, this method has already been successfully applied at orthotropic structures by Venini [61], and it is reported here as basis for comparison with the analytical method derived in the previous section. Unlike the analytical method, this approach considers only mechanical excitation. The total radiated power is computed by considering all the possible positions of uncorrelated point forces, in order to average out the contribution of cross-modal coupling:

$$\overline{W}_{mn} = \overline{|u_{mn}|^2} \int_0^{2\pi} \int_0^{\pi/2} \frac{\mathcal{A}_{mn}(r) \mathcal{A}_{mn}^*(r)}{2\rho c_0} r^2 d\theta d\phi, \quad (3.52)$$

### 3.6. Resonant and non-resonant modes

---

where  $r(r, \theta, \phi)$  represents a point in the fluid domain, in spherical coordinates. The square modulus of the modal velocity amplitude averaged over all the excitation positions is computed as:

$$\overline{|u_{mn}|^2} = \frac{4\omega^2 |F|^2}{M^2 \left[ (\omega_{mn}^2 - \omega^2)^2 + \eta^2 \omega_{mn}^4 \right]}, \quad (3.53)$$

where  $M$  is the plate mass,  $F$  is the amplitude of the exciting force,  $\eta$  represent the plate loss factor and  $\omega_{mn}$  is the orthotropic plate natural frequency associated with the mode  $(m, n)$  [58]:

$$\omega_{mn} = \frac{\pi^2}{\sqrt{\rho h L_x^2}} \sqrt{D_x m^4 + 2Bm^2 n^2 \left(\frac{L_x}{L_y}\right)^2 + D_y n^4 \left(\frac{L_x}{L_y}\right)^4}. \quad (3.54)$$

The function  $\mathcal{A}_{mn}$  is defined as:

$$\mathcal{A}_{mn}(r) = ik_0 \rho_0 c_0 \frac{e^{-ik_0 r} L_x L_y}{2\pi r \pi^2 mn} \left[ \frac{(-1)^m e^{i\alpha} - 1}{(\alpha / (m\pi))^2 - 1} \right] \left[ \frac{(-1)^m e^{i\beta} - 1}{(\beta / (n\pi))^2 - 1} \right]. \quad (3.55)$$

The terms  $\alpha$  and  $\beta$  are given in equation (3.51). The mean square velocity, averaged over all the force positions, is given for each mode  $(m, n)$  by:

$$\overline{\langle v_{mn}^2 \rangle}_{s,t} = \frac{1}{2M^2} \frac{\omega^2 |F|^2}{\left[ (\omega_{mn}^2 - \omega^2)^2 + \eta^2 \omega_{mn}^4 \right]}. \quad (3.56)$$

The modal radiation efficiency  $\sigma_{mn}$  can be determined by substituting the modal radiated power  $\overline{W}_{mn}$  and the averaged mean square velocity  $\overline{\langle v_{mn}^2 \rangle}_{s,t}$  into equation (3.49), to obtain a formulation identical to Wallace's equation (3.50). Finally the orthotropic average radiation efficiency, considering all the possible force positions, is determined as:

$$\sigma = \frac{\sum_{m=1}^{\infty} \sum_{n=1}^{\infty} \sigma_{mn} \left[ (\omega_{mn}^2 - \omega^2)^2 + \eta^2 \omega_{mn}^4 \right]^{-1}}{\sum_{m=1}^{\infty} \sum_{n=1}^{\infty} \left[ (\omega_{mn}^2 - \omega^2)^2 + \eta^2 \omega_{mn}^4 \right]^{-1}}. \quad (3.57)$$

### 3.6 Resonant and non-resonant modes

Before introducing the equations to determine the modal-average radiation efficiency of an orthotropic plate, it might be useful to make some considerations on resonant and non-resonant modes. A forced wave induced into the plate by an external excitation, either mechanical or acoustic, will propagate with the free wavenumber rather than the forced one once it has been reflected by the edges. The forced response of a plate, mechanically excited at a certain frequency, is given by the superposition of a theoretically infinite number of modes. The multi-mode response due to a broadband

### 3.6. Resonant and non-resonant modes

---

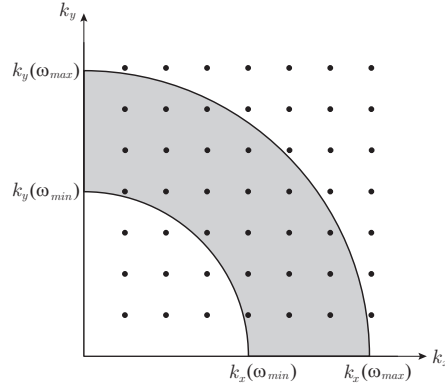


Figure 3.3: Resonant and non-resonant modes represented in the wavenumber space: the shaded area represents the frequency range of the exciting source. Resonant modes are identified in the wavenumber space by points falling within the shaded region.

mechanical force is governed by resonant modes, and those are responsible for most of the radiated sound power [78]. The resonant modes are those with wavenumbers  $k_{mn}$  that match the forced wavenumber. The structural wavenumber  $k_{mn}$  associated with the mode  $(m, n)$  is defined, as a function of its  $x - y$  components given in equation (2.18), as:

$$k_{mn} = \sqrt{k_x^2 + k_y^2}. \quad (3.58)$$

In Figure 3.3, each plate mode is represented in the wavenumber space at his natural frequency, by a single point of coordinates  $(k_x, k_y)$ . The modes that fall within the shaded region are resonant modes, since their natural frequency matches one of the exciting frequencies. The wavenumber diagrams are useful to understand the different mechanisms that govern sound radiation in different frequency ranges. In Figure 3.4, where the wavenumber components have been normalised for the acoustic wavenumber  $k_0$ , five different regions associated with different classes of modes can be identified, according to the relationship between  $k_x$ ,  $k_y$  and  $k_0$ :

- (a)  $k_{mn} < k_0$  and  $k_y, k_x < k_0$ : above the coincidence region;
- (b)  $k_{mn} > k_0$  and  $k_y, k_x < k_0$ :  $x - y$  edges modes;
- (c)  $k_x > k_0$  and  $k_y < k_0$ :  $y$ -edge modes;

### 3.6. Resonant and non-resonant modes

---

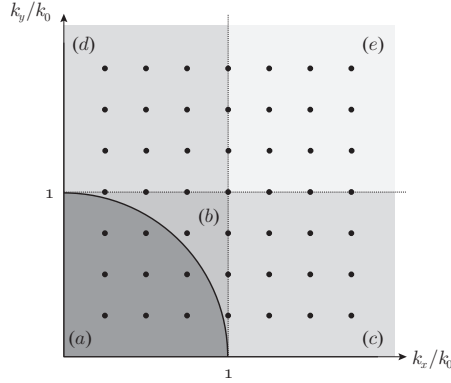


Figure 3.4: Different radiation modes represented in the normalised wavenumber space. a) modes above the coincidence; b) edges modes; c)  $y$ -edge modes; d)  $x$ -edge modes; e) corners modes.

(d)  $k_x < k_0$  and  $k_y > k_0$ :  $x$ -edge modes;

(e)  $k_x > k_0$  and  $k_y > k_0$ : corner modes.

The frequency at which the structural wavenumber equals the acoustic wavenumber  $k_{mn} = k_0$ , and the flexural wave velocity matches the acoustic velocity in the surrounding fluid, is called first coincidence, or critical frequency  $f_c$ . Assuming that all modes are resonant, excited by a broadband mechanical force, the resonant plate modes can be divided in different classes. The most efficient radiators are the ones characterised by a structural wavenumber  $k_{mn} < k_0$ . Above the critical condition the sound is radiated uniformly from the plate surface and propagates away from the surface, like in the case of a piston source, since the bending wavenumber always fits the wavenumber of the acoustic wave, according to the relationship  $k_B = k_0 \sin \theta$ , or analogously  $\lambda_0 = \lambda_B \sin \theta$ , as shown in Figure 3.6a). Below the critical condition the acoustic wavelength is bigger than the plate wavelength, thus air particles can move parallel to the plate surface to compensate the oscillating areas associated with high and low pressure. The sound is radiated only at the edges, and at other discontinuities, where the pressure change cannot be fully compensated by the moving fluid particles. In this frequency range the radiation efficiency is much smaller than unity. This phenomenon is illustrated in Figure 3.5a), considering a mode shape of the plate where both the bending wavelength  $\lambda_x$  and  $\lambda_y$  are smaller than the acoustic wavelength  $\lambda_0$ , the sound radiated can be modelled as quadrupole source in the center of the plate, and dipole sources along the edges. The positive and negative contributions cancel out, except at the corners of the plate, when

### 3.6. Resonant and non-resonant modes

---

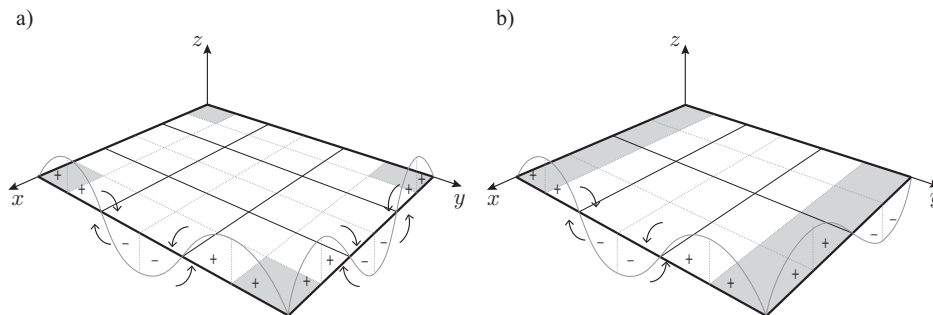


Figure 3.5: Cross-cancellation representation for a) corner mode:  $\lambda_x, \lambda_y < \lambda_0$ ; b) edge mode:  $\lambda_x \geq \lambda_0$  and  $\lambda_y < \lambda_0$

the sound can be seen as radiated by a monopole source. These are known as *corner-modes*.

Otherwise, the modes characterised by at least one of the structural wavelengths propagating along the principle direction larger than the acoustic wavelength, are called *edge-modes*. In this case cross-cancellation happens at the center of the plate between out of phase dipole sources, but not along the edge associated with the the larger wavelength, as shown in Figure 3.5b).

As already mentioned the transverse vibration of a plate mechanically excited by a broadband force consists of a near-field, that represents the vibrational field of an infinite plate, and a resonant field due to the reflection at the boundaries. Above the critical condition the near field cannot be distinguished from the resonant field. However, even if the resonant fields tends to be the dominant component, the near-field contribution might be significant below the critical frequency. The radiation behaviour is different when the structure is acoustically excited by an incident plane wave or a diffuse sound field. In this case the plate vibrational response consists of a non-resonant forced field at the excitation frequency and a resonant field, generated when the forced wave is reflected at the edges. The dynamic response of a plate acoustically excited is strongly related to its sound radiation behaviour by the so-called *vibro-acoustic reciprocity principle* presented by Lord Rayleigh [6], and clearly illustrated in Ref. [60]. Considering a simplifying example of a plane sound wave impinging on an infinite plate at the frequency  $\bar{f}$ , at an angle  $\theta$  to the normal to the surface, the plate response has to match the incident wavelength, and it is characterised by a single trace wavenumber  $\bar{k}_t = \bar{k}_0 \sin \theta$ , Figure 3.6b). The forced flexural wave travels across the plate with a velocity  $\overline{c}_F = c_0 / \cos \theta$ , always equal or greater than the acoustic velocity  $c_0$ . When the finite dimension of real structures is taken into account, the spectrum of the incident sound pressure wavenumber is spread over the wavenumber domain, due to scattering and

### 3.7. Average radiation efficiency model

---

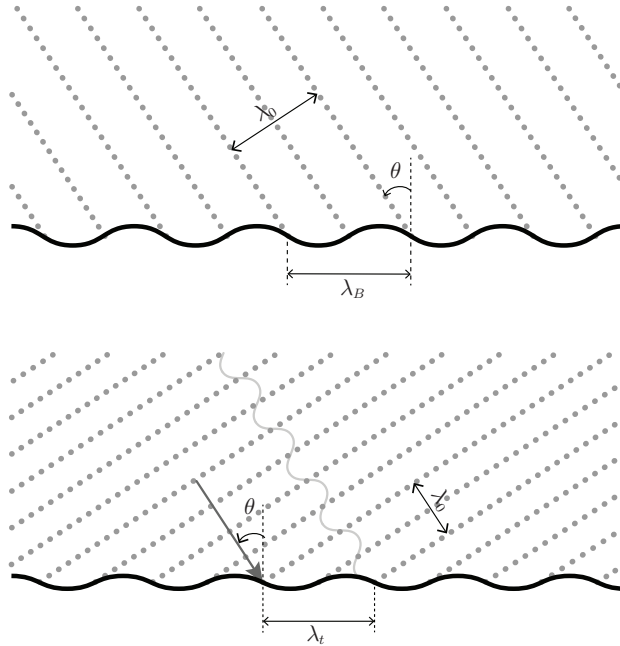


Figure 3.6: a) Matching between the bending wavelength propagating in the plate and the wavelength of the radiated acoustic wave propagating away from the surface; b) Matching between the incident acoustic wavelength, and the forced trace wavelength propagating in the plate.

diffraction caused by variation of the surface impedance. Analogously, a structural wavenumber  $k_t$ , propagating in the finite size plate, can take an infinite range of values. The forced flexural waves, induced by the incident sound field, will travel with free bending wavenumbers once they have been reflected. Therefore, even those modes with a resonant frequency below the critical condition can be excited by an acoustic plane wave, even if not at their resonance. The forced non-resonant field tends to govern the sound radiation below the critical condition while, as it happens for mechanically excited plates, near and above the critical condition this contribution is not distinguishable from the resonant field.

### 3.7 Average radiation efficiency model

So far the average radiation efficiency of orthotropic plates has been computed by considering the sound power radiated by each single mode. However, as the number of modes within the frequency band increases it might be more convenient to directly derive a modal-average radiation efficiency, rather than consider the modal radiation. Approximated formulations of the modal-

### 3.7. Average radiation efficiency model

---

average radiation efficiency, which provide a general trend of the radiation behaviour of the structure as a function of the frequency, have been given by several authors [8, 77, 22]. This acoustic descriptor, usually expressed in one third octave bands, is often required in building acoustics for prediction models based on the statistical energy analysis (SEA) framework, or when a broad band excitation is involved. The average radiation efficiency of orthotropic and composite plates, under Mindlin's theory, was derived using the wave approach by Ghinet and Atalla [79]. This statistical approach needs some additional assumptions: (i) high modal density and modal overlap over the entire frequency range, to treat the discrete distribution of modes as a continuous function; (ii) the sound power is only radiated by resonant modes; (iii) the resonant modes are uncorrelated; (iv) equipartition of modal energy: all the modes within the frequency band have the same vibrational energy. To consider the total resonant vibrational energy, the orthotropic radiation efficiency  $\sigma(\omega, \phi)$  is weighted by the plate modal density  $n_d$ , within the frequency range delimited by  $\omega_{min}$  and  $\omega_{max}$ :

$$\sigma_r(\omega) = \frac{\int_{\omega_{min}}^{\omega_{max}} \int_0^{\pi/2} \sigma(\omega, \phi) n_d(\omega, \phi) d\phi d\omega}{\int_{\omega_{min}}^{\omega_{max}} \int_0^{\pi/2} n_d(\omega, \phi) d\phi d\omega}. \quad (3.59)$$

The plate modal density  $n_d$ , that describes the number of modes per Hz, is given by [80, 81]:

$$n_d(\omega) = \frac{L_x L_y}{\pi^2} \int_0^{\pi/2} k_B(\omega, \phi) \frac{\partial k_B}{\partial \omega} d\phi. \quad (3.60)$$

The average radiation model presented here, is based on an analogous formulation developed under the thin plate assumptions following the work presented by Anderson and Bratos-Anderson [30]. The average radiation efficiency given in equation (3.59) can be reformulated for a thin orthotropic baffled plate, with simply supported boundary conditions, as:

$$\sigma_r(\omega) = \frac{L_x L_y}{\pi^2 n_d} \int_0^{\pi/2} \sigma(\omega, \phi) k_B \frac{\partial k_B}{\partial \omega} d\phi. \quad (3.61)$$

The model proposed by Anderson et al. was developed for a specially orthotropic carbon laminate plate, with the principal axes aligned with the edges, undergoing harmonic vibrations. In order to investigate cross-laminated timber plates, this model has been slightly modified, to allow for frequency dependent input data, which are necessary to compensate for the simplified thin plate theory, that neglects the shear effect. The radiation efficiency  $\sigma(\omega, \phi)$ , at the angular frequency  $\omega$ , and for a propagation azimuthal angle  $\phi$  of structural wave, is computed using Leppington's asymptotic



### 3.7. Average radiation efficiency model

---

formulations [77, 82], developed for three different frequency ranges, with respect to the critical condition:

$$\begin{aligned}\mu < 1 - \delta & : \text{above the critical condition;} \\ \mu = 1 \pm \delta & : \text{near the critical condition;} \\ \mu > 1 + \delta & : \text{below the critical condition;}\end{aligned}$$

where  $\mu$  is the dimensionless bending wavenumber defined as the ratio  $\mu = k_B/k_0$  and  $\delta$  indicates a frequency range around the critical condition  $\mu = 1$ , defined *near-coincidence* region. The complete set of Leppington's equations to compute the asymptotic radiation efficiency for a given angle  $\phi$  are provided in Annex C. However, Leppington's papers do not provide much information on how the term  $\delta$ , to define the frequency limits, should be determined. The procedure to determine the three frequency ranges for which Leppington's equations are defined was implemented for a discrete number of angles within the interval  $0 \leq \phi \leq \pi/2$  and is described in Annex C. At any propagation angle  $\phi$  the direction-dependent bending wavenumber  $k_B(\phi)$  can be estimated from the wavenumber components along the principal directions  $k_{B,x}$  and  $k_{B,y}$ , by applying a well-established orthotropic elliptic model [30, 83]:

$$k_B(\phi) = \sqrt{(k_{B,x} \cos \phi)^2 + (k_{B,y} \sin \phi)^2}. \quad (3.62)$$

The modal density  $n_d$ , given in equation (3.60), can be re-written for a thin orthotropic rectangular plate as:

$$n_d = \frac{L_x L_y \sqrt{\rho h}}{2\pi^2} \int_0^{\pi/2} \sqrt{\frac{1}{D(\phi)}} d\phi. \quad (3.63)$$

The orthotropic plate bending stiffness, that appears in the integrand denominator of equation (3.63), is defined as:

$$D(\phi) = D_x \cos^4 \phi + 2B \cos^2 \phi \sin^2 \phi + D_y \sin^4 \phi. \quad (3.64)$$

Computing the orthotropic bending stiffness using equation (3.64) requires the knowledge of the in-plane shear modulus  $G_{xy}$ . In order to evaluate the plate modal density the direction dependent bending stiffness can be approximated for each propagation angle  $\phi$ , at a given angular frequency  $\omega$ , as a function of the bending wavenumber  $k_B$  given in equation (3.62):

$$\tilde{D}(\phi) = \frac{\omega^2 \rho h}{k_B^4(\phi)}. \quad (3.65)$$

This approximation might be helpful when information regarding the in plane shear modulus  $G_{xy}$  is not available. Moreover, it is straightforward from equation (3.62) and (3.65) to determine the rate of change of the plate wavenumber with the frequency:

$$k_B(\phi) \frac{\partial k_B}{\partial \omega} = \frac{(k_{B,x} \cos \phi)^2 + (k_{B,y} \sin \phi)^2}{2\omega}. \quad (3.66)$$

### 3.7.1 Near-field and non-resonant contribution

The modal-average radiation efficiency computed from equation (3.59) considers only sound radiated due to resonant modes. In order to increase the model accuracy, Davy recently presented a method to include the near-field contribution for point and line mechanical forces [23]. The radiation efficiency of a simply-supported plate, excited by a point-force acting orthogonally to its surface, is given by:

$$\sigma = \begin{cases} \sigma_r \left(1 + \frac{1}{r_r}\right) & \text{if } \omega < \omega_c; \\ \sigma_r & \text{if } \omega \geq \omega_c. \end{cases} \quad (3.67)$$

The ratio  $r_r$ , of the sound power radiated by resonant modes to the sound power radiated by the vibrational near-field due to the point-force, can be computed as:

$$r_r = \frac{\pi\omega_c\sigma_r}{4\omega\eta}. \quad (3.68)$$

While, if the plate is excited by a line-force acting orthogonally to the plate surface, the ratio of the resonant field to the near-field is given by:

$$r_r = \frac{\sigma_r\sqrt{\omega_c/\omega}}{2\eta}. \quad (3.69)$$

Moreover in the same paper, Davy introduced the possibility to take into account the non-resonant radiation contribution for acoustically excited plates. In this case, the transverse vibration consists of a freely propagating resonant field and a forced non-resonant vibrational field. The ratio of the sound power radiated by the two contributions is equal to the ratio  $r$ , given in equation (3.68) for a mechanical point-force. The radiation efficiency of the plate excited by an incident plane wave is computed as:

$$\sigma = \begin{cases} \frac{1}{r+1} (r\sigma_r + \sigma_{nr}) & \text{if } \omega < \omega_c; \\ \sigma_r & \text{if } \omega \geq \omega_c. \end{cases} \quad (3.70)$$

Below the critical condition, the non-resonant radiation efficiency  $\sigma_{nr}(\phi)$ , for a given angle incidence  $\theta$ , has to be considered together with the resonant contribution  $\sigma_r$ . Different models have been proposed to take into account the diffraction effects due to the finite size of the structure, discussed in the previous section. The radiation efficiency of finite size panels was investigated by Sato [84] and Sewel [85], considering an oblique incident wave, and a diffuse field excitation. More recently, Davy [21] derived an analytical expression, based on two dimensional strip theory, approximating Sato's results. Villot et al. [86] developed a model to compute the finite size

### 3.7. Average radiation efficiency model

---

radiation efficiency, based on wave approach, using the spatial windowing technique. Considering a plane wave incident on the plate at an angle  $\theta$  to the normal, the non-resonant radiation efficiency  $\sigma_{nr}$  is computed as:

$$\sigma_{nr}(k_t, \phi) = \frac{S}{\pi^2} \int_0^{k_0} \int_0^{2\pi} \left\{ \frac{1 - \cos[(k_r \cos \varphi - k_t \cos \phi) L_x]}{[(k_r \cos \varphi - k_t \cos \phi) L_x]^2} \right. \\ \left. \frac{1 - \cos[(k_r \sin \varphi - k_t \sin \phi) L_y]}{[(k_r \sin \varphi - k_t \sin \phi) L_y]^2} \frac{k_0 k_r}{\sqrt{k_0^2 - k_r^2}} \right\} d\varphi dk_r. \quad (3.71)$$

The trace wavenumber  $k_t$  is related to the plane wave incident angle  $\theta$  according to the relationships:  $k_t = k_0 \sin \theta$ ;  $k_r$  is the modulus of the wavenumber spectrum in of the structural vibration velocity, the angle  $\varphi$  indicates the propagation direction as polar coordinate in the wavenumber space. A simplified version of this formulation was proposed by Vigran [87], but it's limited to isotropic plates with a low aspect ratio. An alternative, and more general model to account for the finite dimension of the excited structure, was proposed by Rhazi and Atalla, based on Rayleigh integral formulation [88]. The radiation efficiency is computed from the real part of the radiation impedance, normalised for the plate surface, as:

$$\sigma_{nr}(k_t, \phi) = k_0 \frac{L_y}{4\pi} \int_0^{\pi/2} r \mathcal{G}(\varrho) d\varrho. \quad (3.72)$$

The function  $\mathcal{G}$  of the variable  $(\varrho)$ , obtained in the paper after a few changes of variables, can be solved analytically:

$$\mathcal{G}(\varrho) = \frac{1}{4} [\mathcal{G}(\varrho, \alpha_1) + \mathcal{G}(\varrho, \alpha_2) + \mathcal{G}(\varrho, \alpha_3) + \mathcal{G}(\varrho, \alpha_4)]. \quad (3.73)$$

The functions  $\mathcal{G}$  can be computed as:

$$\mathcal{G}(\varrho, \alpha_i) = \sin(\alpha_i R_\theta) \left[ -\frac{2}{\alpha_i^2} \left( \frac{L_x}{L_y} \sin \varrho + \cos \varrho \right) + \frac{2L_x}{\alpha_i^2 L_y} R_\theta \cos \varrho \sin \varrho \right] \\ + \cos(\alpha_i R_\theta) \left[ -\frac{4}{\alpha_i} + 2 \frac{R_\theta}{\alpha_i} \left( \frac{L_x}{L_y} \sin \varrho + \cos \varrho \right) \right. \\ \left. + \frac{L_x}{L_y} \cos \varrho \sin \varrho \left( \frac{2}{\alpha_i^3} - \frac{R_\theta^2}{\alpha_i} \right) \right] \\ - \frac{2}{\alpha_i^3} \frac{L_x}{L_y} \cos \varrho \sin \varrho + \frac{4}{\alpha_i}, \quad (3.74)$$

where the variables  $\alpha_i$  are defined as:

$$\alpha_{1,2} = \frac{L_x}{2} [k_0 \pm k_t \cos(\varrho - \phi)]; \quad \alpha_{3,4} = \frac{L_x}{2} [k_0 \pm k_t \cos(\varrho + \phi)]; \quad (3.75)$$

### 3.8. Conclusion

---

and  $R_\theta$  is defined as a function of incidence angle  $\theta$  and the plate aspect ratio as:

$$R_\theta = \begin{cases} \frac{2}{\cos \theta} & \text{if } \theta \leq \arctan\left(\frac{L_y}{L_x}\right); \\ \frac{L_y}{L_x} \frac{2}{\sin \theta} & \text{if } \theta > \arctan\left(\frac{L_y}{L_x}\right). \end{cases} \quad (3.76)$$

A simplified version of such a model was presented by Bonfiglio et al. [89], by introducing an additional change of variable. This formulation is computationally more efficient but its applicability is restricted to isotropic panels with low aspect ratio. Based on Rhazi and Atalla approach, also Davy et al. [23] proposed approximate formulation for the forced radiation impedance, assuming it to be independent from the azimuthal angle. The non-resonant radiation efficiency evaluated using either equation (3.71), or (3.72), is dependent upon the azimuthal propagation angle  $\phi$ , thus, the structural averaged radiation efficiency can be computed by a further integration over  $0 < \phi < 2\pi$ . It should be mentioned that the ratio  $r_r$  between the resonant and the near-field, or the non-resonant field, as defined by equations (3.68) and (3.69), was developed only for homogeneous isotropic plates [90], therefore this correction cannot be extended to orthotropic elements. However, acoustically excited structures are usually investigated in terms of sound transmission rather than sound radiation. Since the non-resonant radiation efficiency does not depend on the properties of the plate, but only on its geometry [91], it is helpful to consider the diffraction effect in sound transmission models based on wave propagation in infinitely extended element, as illustrated later on in Chapter 5.

### 3.8 Conclusion

In this Chapter different approaches to model the radiation efficiency of an orthotropic thin plate have been presented. An analytic model has been developed from the plate's equation of motion, derived using Hamilton's variational principle. This approach allows to compute the sound power radiated by each single mode, either resonant or non-resonant. The plate dynamic response can be computed both for a mechanical exciting force, or for an incidence sound field. Further, it is possible to take into account the influence of the fluid loading on the plate response. This effect is almost negligible when the density of the fluid is much lower than the density of the structure. In this case the radiation impedance can be approximated by the self-radiation resistance, reducing significantly the computational cost of the algorithm. A model based on the modal summation approach has been introduced as basis for comparison, since it was already successfully applied to orthotropic panels. This model computes the plate response,

### 3.8. Conclusion

---

and the sound power radiated, averaging over all the possible position of a mechanical point force, to reduce the influence of the fluid loading. When the plate response is characterised by an high modal density, within the investigated frequency range, the radiation efficiency can be computed from a modal-average approach. Each mode is considered only at its resonance, therefore this model is usually applied to investigate the radiation efficiency of structures mechanically excited by a broadband force, since in this case the multi-mode response is governed by the resonant field. Although an approach to take into account the near-field contribution in mechanically excited plates, or the non-resonant response when the structure is excited by a sound field, is available, it has been developed only for homogeneous isotropic plates, thus it does not apply to orthotropic elements. Nevertheless, the geometric radiation efficiency, associated with non-resonant sound radiation, is dependent only on the plate dimension and it can be used to increase the accuracy of sound transmission models, as it will be discussed in the following of this dissertation. In Table 3.1 the suitability of the different approaches to evaluate the sound radiated from isotropic or orthotropic plates under different condition is summarised.

### 3.8. Conclusion

---

Table 3.1: Summary of the different models to compute sound radiation of isotropic and orthotropic plates

	Isotropic Plates	Orthotropic Plates
Modal-Average approach	Modal-average radiation efficiency of resonant modes (high-modal density)	
Modal-Average + near-field correction	Modal-average radiation efficiency of mechanically excited plates	-
Modal-Average + non-resonant correction	Modal-average radiation efficiency of acoustically excited plates	-
Modal Approach	Sound radiation of plates excited by external forces of different nature, immersed in a lightweight fluid (fluid loading is neglected)	
Analytical Approach	Sound radiation of plates excited by external forces of different nature immersed in a lightweight or heavy fluid (fluid loading and modal cross-coupling are taken into account)	

## Chapter 4

# Sound radiation efficiency of CLT plates

### 4.1 Introduction

In this Chapter the experimental evaluation of the radiation efficiency of cross-laminate timber plates is investigated. Cross-laminated timber, often abbreviated to the acronym CLT, is an innovative engineered solid wood material consisting of an odd number of layers of lumber beams glued together, alternating perpendicularly the wood fibres orientation of neighboring plies:  $0^\circ - 90^\circ$ . The outer layers fibres are oriented vertically in order to increase the vertical load-bearing capacity of wall panels. CLT elements can be made of different lumber species, such as pine-wood, spruce, or larch. Building panels are generally fabricated with three, five, or seven layers, according to the static requirements, with a total thickness up to 500 mm. According to the standard EN 16351 [92] the thickness of each layer should be within the range 4 – 65 mm. An exhaustive review of all the different aspects that concern CLT, from manufacture to building design, can be found in [93]. This relatively new engineered wood material has gained a growing success in construction market over the last two decades, especially in Europe and North America. CLT plates provide good structural stability, fulfil the safety requirements and allow to reduce the construction time, since they can be completely prefabricated and then rapidly assembled at the construction site. Nowadays, CLT represents a valuable alternative to traditional building materials like concrete, masonry and steel.

However CLT structures, due to their high stiffness combined with their low density, provide a poor sound insulation. To enhance their performance and meet the acoustic requirements for buildings, it is necessary to design and optimise specific treatments, such as additional layers applied to the walls [94], like gypsum board linings on a cavity, or a concrete floating screed over the CLT floor [95]. Due to the layered structure CLT plates exhibit

an orthotropic behaviour [96], having different elastic properties along the vertical and the horizontal direction. For this reason, in section 4.5, the experimental radiation efficiency is used to validate the different prediction models presented in the previous Chapter.

Although the laboratory experimental evaluation of the radiation efficiency has been presented in several papers, mainly to validate prediction model results, and a few attempts to perform in-situ measurements have also been made [97], at the moment there are no standard procedures to measure this important acoustic descriptor. It should be noted that the radiation efficiency is not directly measurable but needs to be experimentally determined through other quantities: namely the total radiated sound power and the mean square vibration velocity. In the next section two different approaches used to determine the radiation efficiency of three different CLT plates will be introduced and discussed. In section 4.3 the average radiation efficiencies of three cross laminated timber plates are compared, to highlight how the ratio of the layers' thickness influences their vibro-acoustic behaviour. The two different methods used to compute the radiated sound power are compared. Finally, a parametric study on the same set of experimental data set is performed, to better understand how the mean square vibration velocity is influenced by the number of measured points and their distribution on the plate surface.

An easily implementable non-destructive procedure developed to evaluate the elastic and stiffness properties of specific orthotropic building elements is presented, and applied to a CLT plate. The literature offers a variety of different approaches to experimentally investigate the mechanical properties of solid wood through non destructive tests [98]. Many of them are modal analysis-based methods [99, 100], or involve ultrasound measurements [101, 102]. The experimental approach presented here is based on wave propagation analysis within the audible frequency range. The flexural wave velocity can be directly evaluated measuring the time-of-flight difference between two adjoining transducers in line with the excitation source, a technique derived from ultrasound measurements [103] and also applied for the characterization of poroelastic materials [104]. Alternatively, the flexural wavenumber can be determined by measuring the phase difference between two consecutive accelerometers, as proposed by Rindel [105] for low frequency measurements. This approach has also been applied by Nightingale [106] to study a wooden joist floor, implementing a slightly different setup in order to investigate higher frequencies. A method to measure the flexural wave velocity, based on phase difference of the frequency response function (FRF) [107], was also applied by Thwaites to detect damages in sandwich structures other than to determine the material elastic properties [108]. While these approaches use continuous wave random noise excitation, or impact impulses, the method to be described here involves short pulse excitation. Pulse excitation usually requires more effort during the measurement stage, since a longer time



## 4.2. Experimental measurements

---

Table 4.1: CLT plates geometry and density

		CLT80_a	CLT80_b	CLT100
$L_x$	[m]	4.20	4.20	4.20
$L_y$	[m]	2.90	2.90	2.90
$h_{tot}$	[mm]	80	80	100
$h_{out.l.}$	[mm]	15	30	30
$h_{int.l.}$	[mm]	50	20	40
$\rho$	[kgm <sup>-3</sup> ]	467	484	484

is needed to investigate a wide frequency range, compared to broadband excitation. On the other hand, it allows to obtain accurate results with a much easier signal processing. The novelty aspect of the proposed method is represented by an analytical data fitting of the experimental flexural wave velocity in order to diminish the number of single frequencies to be tested within the investigated band, reducing significantly the measurement time. Besides, the fitting procedure also limits the influence of the scatter in the experimental data, especially at high frequency.

## 4.2 Experimental measurements

### 4.2.1 Studied structures

The investigated three-ply CLT plates are 4.2 m wide and 2.9 m high, their characteristics are reported in Table 4.1, and their cross section along the two principle directions is shown in Figure 4.1. All three panels were tested in Empa<sup>1</sup>'s wall sound insulation test facility as shown in Figure 4.2. The source and the receiving rooms have a volume of 73 m<sup>3</sup> and 101 m<sup>3</sup> respectively. Each plate was mounted into a rigid frame between the two test rooms, and fixed using a sealant putty along the edges on both sides, as shown Figure 4.3. Vibro-acoustic measurements were performed in the frequency range from 1 Hz to 6000 Hz in order to evaluate the plate radiation efficiency. The surface vibration velocity was measured, using a Polytec PSV-500 scanning laser vibrometer, on a grid with 513 evenly distributed points, approximately spaced 160 millimetres apart. The sound pressure transmitted in the receiving room was measured by a B&K rotating boom microphone. The plates were excited subsequently at two different positions using a B&K electrodynamic shake, and acoustically by an omnidirectional

---

<sup>1</sup>Empa - Swiss Federal Laboratories for Material Science and Technology - Laboratory for Acoustics/Noise Control; Dübendorf (Switzerland)

## 4.2. Experimental measurements

---

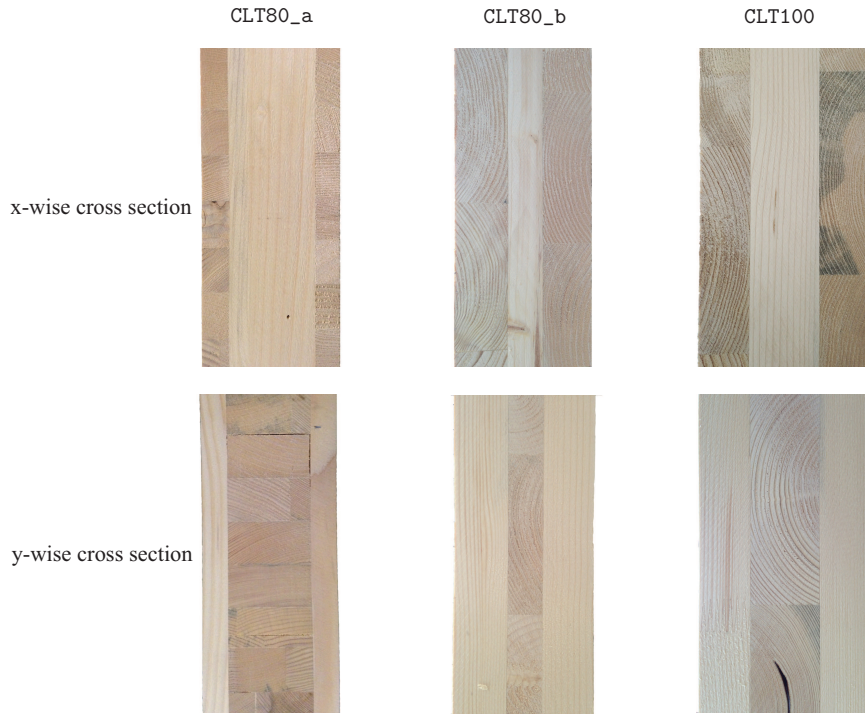


Figure 4.1: Cross section along the two principle directions of the three investigated CLT plates.

dodecahedron source. All sources were driven by a broadband white noise signal. The shaker was connected to the plate by a stinger screwed in the wood. Additionally, the reverberation time of the source and the receiving room was experimentally determined, evaluating the decay curves using the impulse response method and a MLS-signal according to the standard ISO 3382-2 [109]. The radiation efficiency needs to be experimentally determined from other quantities according to equation (3.46).

### 4.2.2 Radiated sound power

The sound power radiated by a vibrating surface is not directly measurable, but it can be experimentally determined by using different approaches. For example it can be evaluated from the average sound pressure measured in a reverberant room; by scanning the vibrating surface using a sound intensity probe, consisting of two microphones; further the radiated sound field can be determined by measuring the sound pressure, or particle velocity, with an array of transducers, by means of a technique known as near-field acoustic holography. Moreover, the radiated sound power can be evaluated

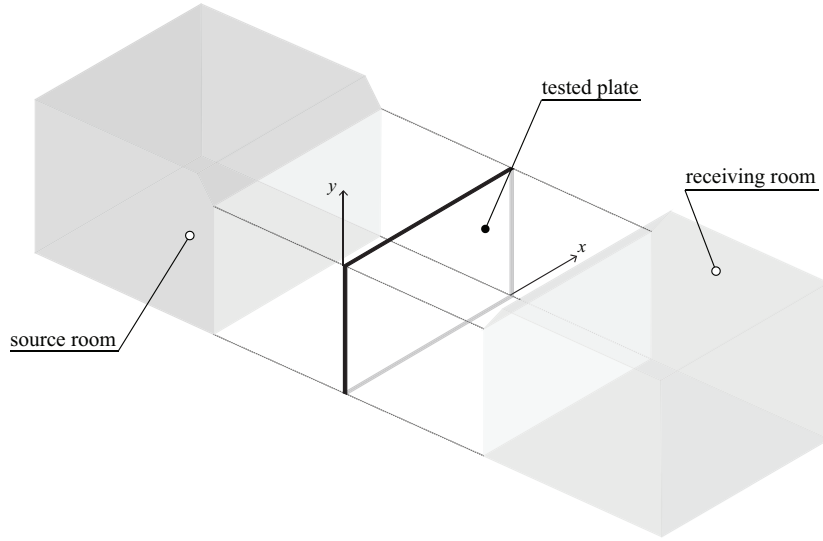


Figure 4.2: Experimental set-up diagram: CLT plate mounted into the sound insulation test facility.

from the surface vibration velocity applying hybrid methods, which use both experimental data and analytic calculation. The sound power radiated from each CLT plate was determined both from the measured diffuse sound pressure field, and from the surface vibration velocity using the hybrid discrete calculation method.

### Diffuse field approach

Assuming a perfectly diffuse sound field, the radiated sound power is determined from the sound pressure measured in the center of the room and the equivalent absorption area of the receiving room. The sound pressure level measured in the central area of the testing room is lower than the mean sound pressure of the entire volume, because in the spatial sampling the boundary regions, where the pressure is higher, are neglected. This effect becomes smaller at high frequencies due to the decrease of the size of the near field at the boundaries. To consider this effect the Waterhouse correction has been applied [56] and the radiated power was calculated using the equation:

$$W_{rad} = \frac{\langle p^2 \rangle_{s,t}}{4\rho_0 c_0} A \left( 1 + \frac{S_T \lambda}{8V} \right) \quad (4.1)$$

where  $\lambda$  is the sound wavelength,  $S_T$  is the total surface area of the receiving room, and the equivalent absorption area  $A$  is calculated from the measured reverberation time  $T_{20}$  and the room volume  $V$ , using the well known Sabine's

## 4.2. Experimental measurements

---

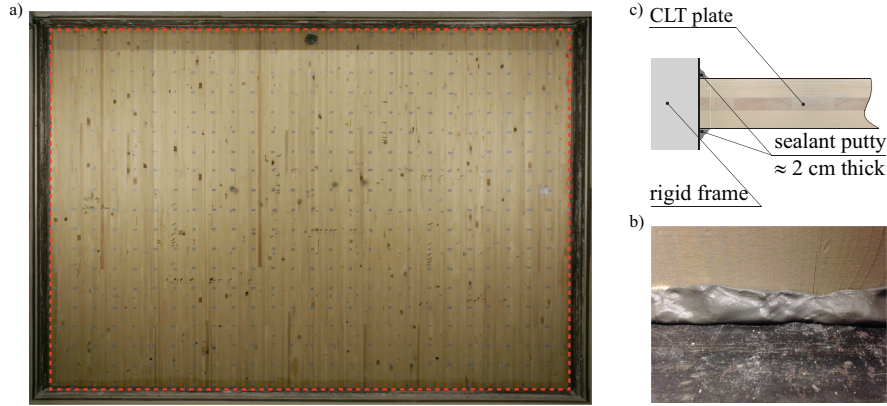


Figure 4.3: Mounting condition of the investigated CLT plates

relationship.

$$A = 24 \ln(10) \frac{V}{c_0 T_{20}} \quad (4.2)$$

This method requires a test facility provided with the test window coupled with a reverberation room to be implemented. The main limit of this approach is the diffuse field assumption, which, in wall sound insulation laboratories designed according to the standard ISO 10140-5 [110], is hardly achieved below 100 Hz.

### Discrete calculation method

The radiated sound power was also evaluated by using the discrete calculation method (DCM), a hybrid method, proposed by Hashimoto [111], that requires both numerical calculations and the experimental measurements of the complex vibration velocity, over a grid of points on the plate surface, but does not involve sound pressure measurements.

$$W_{rad} = \sum_i \left[ \operatorname{Re}(Z_{ii}) |v_i|^2 + \sum_j \operatorname{Re}(Z_{ij} v_i v_j^*) \right] \quad (4.3)$$

The plate surface has to be discretised in small piston-like source elements. The radiated power is determined from the measured complex vibration velocity  $v_{i,j}$ , and from the self  $Z_{ii}$  and cross radiation impedance  $Z_{ij}$  of each small piston source, computed as:

$$Z_{ii} = \rho_0 c_0 s_i \left[ 1 - \frac{J_1(2k_0 a_i)}{k_0 a_i} + i \frac{S_1(2k_0 a_i)}{k_0 a_i} \right]; \quad (4.4)$$

$$Z_{ij} = \frac{\rho_0 c_0 k_0^2 s_i s_j}{2\pi} \left[ 2 \frac{J_1(k_0 a_i)}{k_0 a_i} \right] \left[ 2 \frac{J_1(k_0 a_j)}{k_0 a_j} \right] \left( \frac{\sin k_0 d}{k_0 d} + i \frac{\cos k_0 d}{k_0 d} \right); \quad (4.5)$$

## 4.2. Experimental measurements

---

where  $J_1$  is the first order Bessel's function and  $S_1$  is the Struve's function,  $s_i$  is the area of the  $i^{th}$  element, while  $a_i$  is its equivalent radius and  $d$  is the distance between the  $i^{th}$  and  $j^{th}$  elements. For a complete and more detailed description of this method refer to the original paper presented by Hashimoto.

This approach assumes that the plate radiates sound into a free field, thus the influence of the room is neglected. Since the method does not require the measurement of the sound pressure in a perfectly diffuse field, it can be easily applied at low frequencies. However, the number of plate subdivisions will determine the upper frequency limit. The same set of experimental data was used to evaluate the radiated power and the plate complex velocity on a coarser grid, by considering only 140 of the 513 measured points, in order to investigate two distinct aspects: (i) the effect of the larger size of the piston-like elements, determining a lower upper frequency limit for the radiated power computation; (ii) the influence of the number of measurement positions over which the vibration velocity is spatially averaged.

### 4.2.3 Average vibration velocity

The surface vibration velocity of the three CLT plates was averaged over 513 positions, evenly distributed on grid with a spacing of approximately 160 mm. Vibration velocity measurements on building elements are usually very time consuming, due to the big size of the structures. Nevertheless, by using a scanning laser vibrometer it is possible to map the surface vibration velocity on a narrow grid in a relatively short time, compared to time that would be necessary by using accelerometers. The alternative is represented by averaging the vibration velocity over a random distribution of transducer positions. In order to investigate the influence of spacing between grid points, or the number of positions in a random distribution, a parametric analysis was undertaken on the same set of experimental data. The vibration velocity was thus averaged over the entire set of data of 513 points, Figure 4.4 a), and over a grid of only 140 positions, spaced approximately 320 mm Figure 4.4 b). Furthermore, since accelerometers are more commonly used than scanning laser vibrometer, a random distribution of the measured points was considered. In order to analyse the influence of the number of transducers and their spatial distribution, the mean square velocity was determined by averaging a different number of positions that were randomly chosen as shown in Figure 4.4 c). Random measurement points were chosen over the plate surface according to the requirements given in in the standard EN 10848-1 [112]. The random positions are chosen with respect to the following minimum distances:

- 0.25 m between the measurement points and the plate borders;
- 1.00 m between the excitation point (when a mechanical point source

### 4.3. Experimental results

---

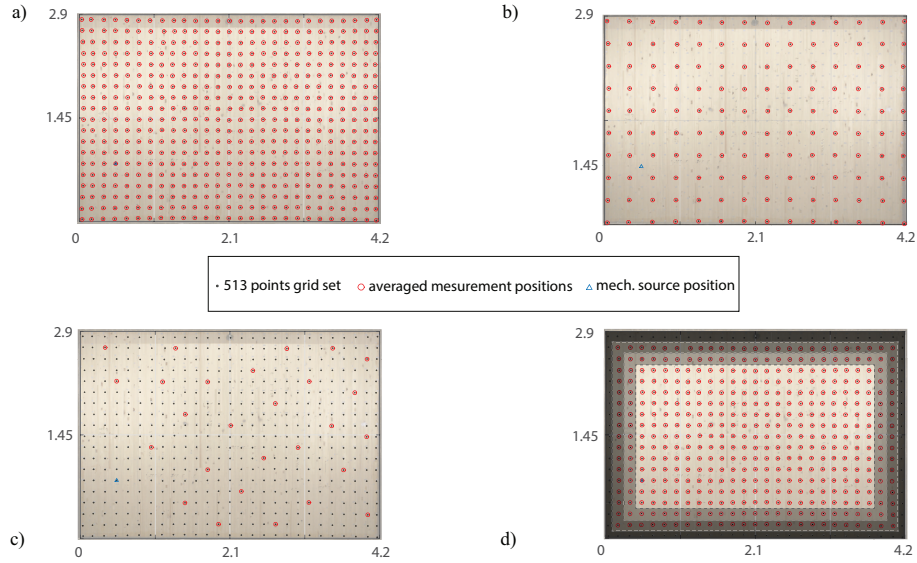


Figure 4.4: Measurement points distributions: a) grid of 513 points; b) grid of 140 points; c) 27 random points fulfilling EN 10848 requirements; d) grid 425 points excluding boundary regions.

is used) and the measurement points;

- 0.50 m between distinct measurement positions.

However, the grid spacing is not the only factor that influences the average velocity, but the distance from the plate borders of the closest measurement position can also be significant on its spectrum. In order to investigate this influence, three different grids of points, neglecting a progressively wider area close to the plate's boundaries, as shown in Figure 4.4 d), were analysed: i) a region approximately 85 mm wide, associated with the most external ring of measurement points, is not considered and the velocity is averaged over 425 positions; ii) a region approximately 255 mm wide, associated with two rings of measurement points, is not considered and the velocity is averaged over 345 positions; iii) a region approximately 422 mm wide, associated with the three orders of measurement points is not considered and the velocity is averaged over 273 positions.

## 4.3 Experimental results

### 4.3.1 CLT plates' radiation efficiency

For each plate the radiation efficiency has been calculated, both for structure-borne and airborne excitation, by averaging the results obtained from the

---

### 4.3. Experimental results

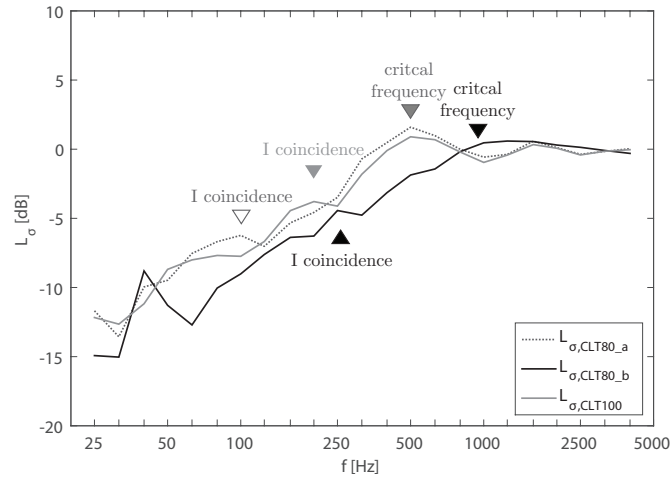


Figure 4.5: Experimental radiation index of the three CLT plates for mechanical excitation. Results presented in one-third octave bands.

DCM and the classical diffuse field method. In Figure 4.5 the radiation index  $L_\sigma = 10 \log(\sigma)$  of the three plates, averaged over the two shaker positions, is compared. The plates CLT80\_a and CLT100 show a similar radiation index; their critical frequency falls within the band centred around 500 Hz. Since the structural flexural wave at a given frequency propagates with different velocity along the two principal directions, orthotropic plates are characterised by two significant coincidence frequencies. The lowest coincidence is associated with the stiffest principal direction and in CLT plates it is related to the vertical orientation of the fibres of the outer layers. The first coincidence is identified below the critical condition by a peak from where the radiation efficiency curve slope changes, falling within the 100 Hz band for the plate CLT80\_a and in the 200 Hz band for the plate CLT100. The plate CLT80\_b exhibits a different behaviour: the radiation curve is shifted towards higher frequencies. The lowest coincidence falls in the 250 Hz frequency band, while the coincidence associated with the orthogonal direction, which also represents the plate critical condition, falls within the 1000 Hz band, and it is marked by a softer peak. These results suggest that the differences in sound radiation are mostly due to the CLT plate's inner structures, since the panels CLT80\_a and CLT80\_b even though have a comparable surface mass exhibit a different radiation efficiency. Moreover, even though the mass per unit of area of the plate CLT100 is approximately 30% greater than the surface mass of the plate CLT80\_b, these structures exhibit a similar radiation behaviour, with the critical frequency falling in the same band. A different ratio between the thickness of outer layers and inner core have a significant influence on the stiffness of the plate.

### 4.3. Experimental results

---

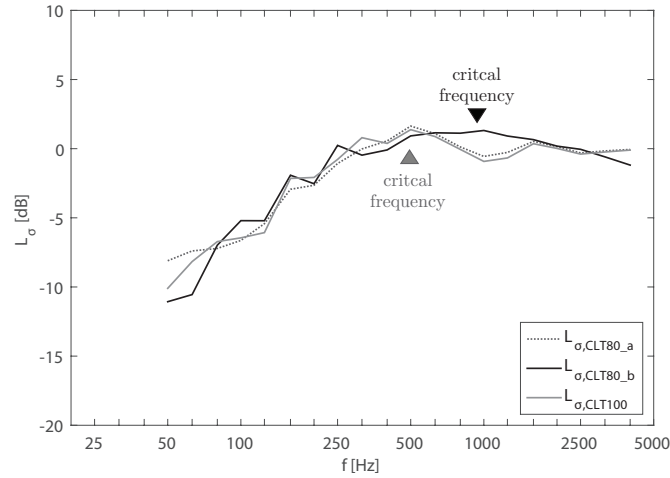


Figure 4.6: Experimental radiation index of the three CLT plates excited by a diffuse sound field. Results presented in one-third octave bands.

When an airborne sound source is used, below the critical condition, all the three plates behave in a similar way, as shown in Figure 4.6. This is due to the great influence of non-resonant modes when the structure is excited by a diffuse sound field, as discussed in Chapter 3. Below the critical frequency the radiation is thus governed by the forced non-resonant field, and since this depends only on the panel dimension, no significant differences are found between the three plates. For none of the investigated panels it is possible to identify the first coincidence frequency. However, the critical frequency of the three elements is still recognisable, falling within the 500 Hz band for the plate CLT80\_a and CLT100, and within the 1000 Hz band for the plate CLT80\_b. It has been found that below 100 Hz, the airborne excitation sound energy was not sufficient to have a good signal to noise ratio to correctly determine the plates' radiation efficiency, for neither the velocity, nor the sound pressure measurements. To highlight the differences due to the exciting source, the experimental radiation index of the plate CLT80\_b is given in Figure 4.7 both for the mechanical force and the diffuse field excitation.

#### 4.3.2 Comparison between diffuse field approach and DCM

In this paragraph the DCM and the classical method, used to evaluate the radiation efficiency, are compared. The comparison is undertaken by presenting results referring to the plate CLT80\_b mechanically excited. The radiation indices given in Figure 4.8 show a good agreement between the two methods, although, the discrete calculation method tends to overestimate



### 4.3. Experimental results

---

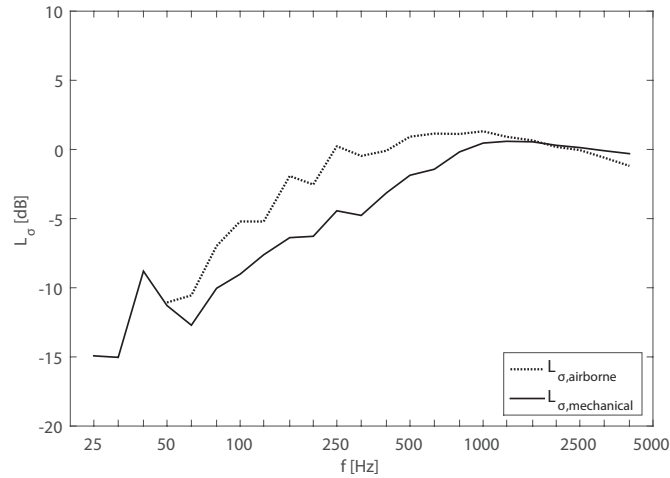


Figure 4.7: Comparison between the experimental radiation indices for mechanical excitation and airborne excitation. The results, in one-third octave bands, refer to the plate CLT80\_b mechanically excited.

the radiation efficiency compared to the diffuse field approach. The biggest difference occurs in the 400 Hz band, where a radiation index about 3 dB higher was obtained from the DCM. In the remaining frequency bands the difference is less than 2 dB:  $\pm 1$  dB around the average.

The main limit of the classical approach is the perfectly diffuse field assumption. In standard sound insulation test facilities this is hardly achievable in the lowest frequency bands, and never verified below 100 Hz [113]. Thus the experimental evaluation of the radiation efficiency cannot be extended to the low frequencies. According to Hashimoto [111], in order to obtain accurate results using DCM, it is necessary that the piston-source elements dimensions are smaller than the half wavelength at the critical frequency of the vibrating plate. The critical frequency of the plate CLT80\_b falls within the 1000 Hz band. The corresponding half wavelength,  $\lambda_c \approx 0.34$  m, is larger than the average grid spacing, approximately equal to 0.16 m. When a 140 points grid is considered, the average size of the sub-elements is about 0.32 m, close to the wavelength at the coincidence frequency. In Figure 4.9 the radiation indexes computed using the two different grids are compared in one-third octave bands. The two curves show a similar trend, but small differences are shown. This indicates that when the spacing between elements equals the structural wavelength, the discretisation of the velocity field is not sufficient and information about the real vibration between points is missing. The velocity of the pistons and thus the radiated sound will appear as uncorrelated in the DCM calculation, as it is also the case above the coincidence frequency of the plate. For the coarser grid of 140 points, this

### 4.3. Experimental results

---

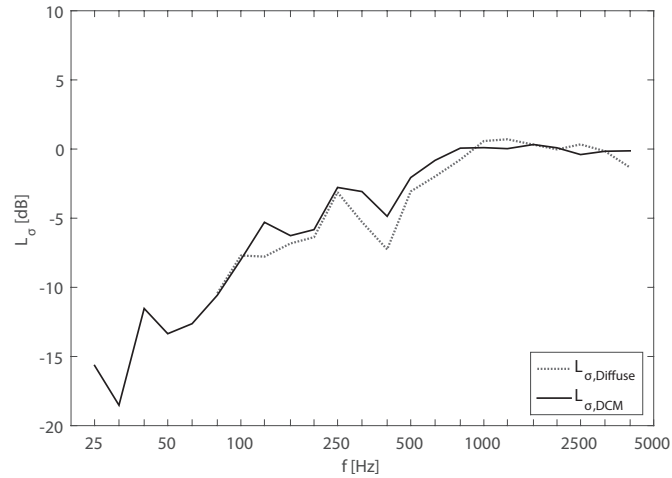


Figure 4.8: Comparison between the experimental radiation indices obtained from the Diffuse field approach and the DCM. The results, in one-third octave bands, refer to the plate CLT80\_b mechanically excited.

limit lays around the coincidence frequency of plate and thus the distinct peak at 1000 Hz is less pronounced compared to the curve obtained with the finer grid. However, also at lower frequencies starting from the 250 Hz frequency band, some discrepancies between the two curves are found. It should be noted that the wider grid average spacing is close to one-quarter of the wavelength at 250 Hz. In many calculation methods in which an element is discretised in smaller sub-elements the one-quarter wavelength is correlated with a frequency limit. This aspect might influence DCM computation of self and mutual sound power and should be further investigated.

#### 4.3.3 Average vibration velocity

The discrepancies in the radiation efficiency obtained from the DCM with different grids might be caused not only by the sound power computation, but also by the measured mean square velocity. In order to investigate the influence of the grid spacing, and of the number of measured positions, mean square velocities averaged over a different number of points are compared. The vibration velocities averaged over all the 513 points and only over 140 points, given in Figure 4.10, show a very similar trend. The mean square velocity curves are in good agreement, with only small discrepancies: the larger difference is about 1.2 dB around the 1250 Hz band. On the other hand, a significant influence on the average velocity spectrum is found in the low frequency range, neglecting the regions closed to the plate boundaries. As shown in Figure 4.11, as the size of the excluded regions increases, the velocity

### 4.3. Experimental results

---

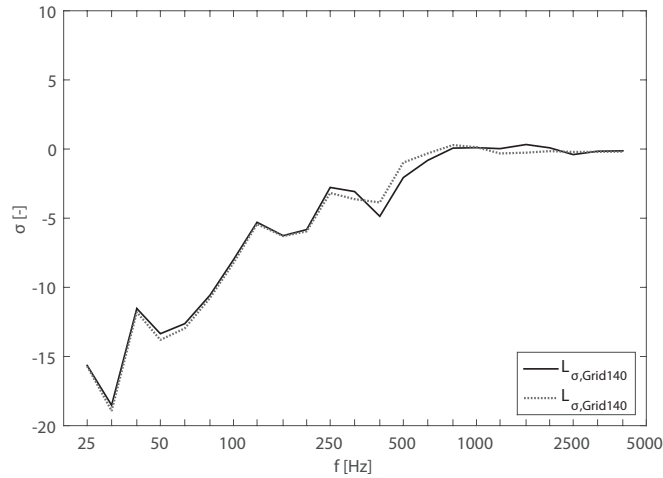


Figure 4.9: Comparison between the radiation efficiency from DCM considering a 513 measurement points grid or a 140 measurement points grid. The results, in one-third octave bands, refer to the plate CLT80\_b mechanically excited.

levels in the low frequency bands increase, and the dip in the 150 Hz band is more emphasised. This effect, caused by the restraints along the edges given by the mounting conditions, is the inverse analogous to the Waterhouse effect, mentioned in the previous section. In fact at low frequencies, higher velocity levels are measured if the boundaries regions are neglected. This is verified up to the band centred on 80 Hz, from which the velocity levels measured only the central region of the plates are lower than the level averaged over the entire scanned surface. Above the 500 HZ no relevant differences are found between the velocity spectra. Since the extension of those border regions is small compared to the plate size, the influence on the average velocity is not very accentuated, however it could be much more emphasised in a smaller plate using a similar grid spacing.

So far only small biases in the plate mean square velocity were obtained, as long as a great number of positions are measured on a grid distribution. But when accelerometers are used to sample the plate vibration velocity, it would be extremely time consuming to obtain a sufficiently dense grid, and therefore a random distribution of fewer points, that gives a good average of the real mean square velocity, is preferred. To understand the influence of the number of measured points, the velocity averaged over 200, 100, 50, 25, 20 and 10 positions, randomly chosen on the plate surface, are compared in Figure 4.12. The velocity level spectra are scattered around the curve computed from the complete set of points, with a more accentuated deviation as the frequency increases, although, it is not clear whether a low spatial

### 4.3. Experimental results

---

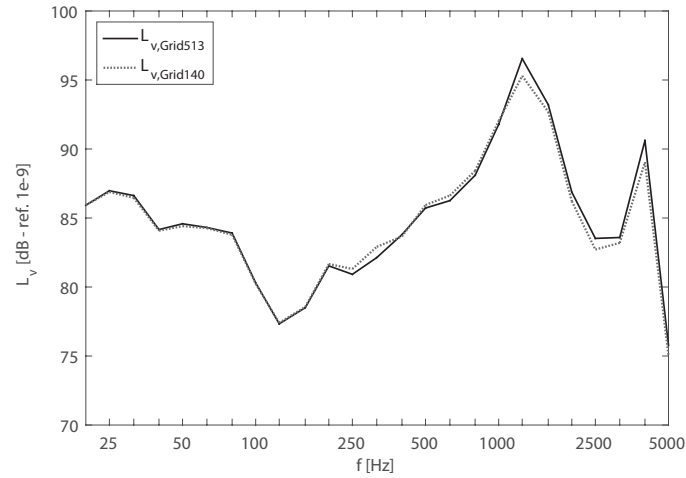


Figure 4.10: Comparison between the surface mean square velocity averaged over 513 measurement points and over 140 measurement points. The results, in one-third octave bands, refer to the plate CLT80\_b mechanically excited.

sampling gives an overestimation or an underestimation of the mean square velocity. For a better understanding, the same results are also given in terms of the overall level difference with the mean square velocity averaged over all the 513 points, in Figure 4.13. The overall single number is computed by taking the energetic sum of all the third-octave bands. This comparison shows that, for a plate of this size, at least 100 measurement points are necessary to reduce drastically the differences with the mean square velocity calculated over 513 positions. In Figure 4.14 a last comparison is made between the surface velocity, averaged over the entire set of 513 points, and averaged over three random distribution of 25 positions, chosen according to the requirements on minimum distances given in the standard EN 10848-1. For the latter case, 25 positions represent the maximum number of transducers that can fit the plate size fulfilling the standard requirements. The velocity spectrum obtained from the different EN distributions always represents an underestimation of the velocity averaged over a great number of points, suggesting that a low sampling, combined with the exclusion of the surface regions close to the discontinuities leads to a lower mean square velocity.

### 4.3. Experimental results

---

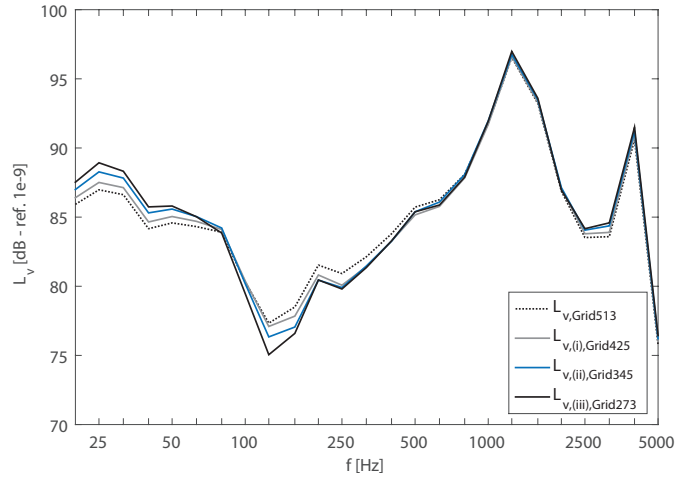


Figure 4.11: Comparison between the mean square velocity averaged over the entire surface (513 points grid) or over a reduced region excluding the border region: grids of 425 points; 345 points; 273 points. The results, in one-third octave bands, refer to plate CLT80\_b mechanically excited.

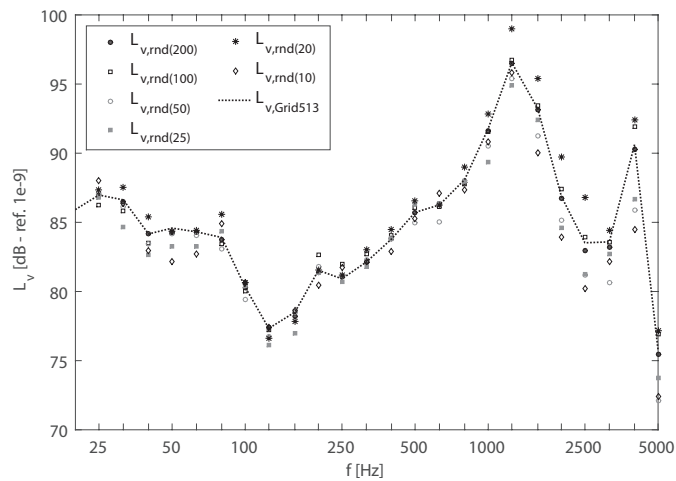


Figure 4.12: Comparison between the mean square velocity averaged over (n) measurement positions randomly distributed on the panel surface. The results, in one-third octave bands, refer to plate CLT80\_b mechanically excited.

### 4.3. Experimental results

---

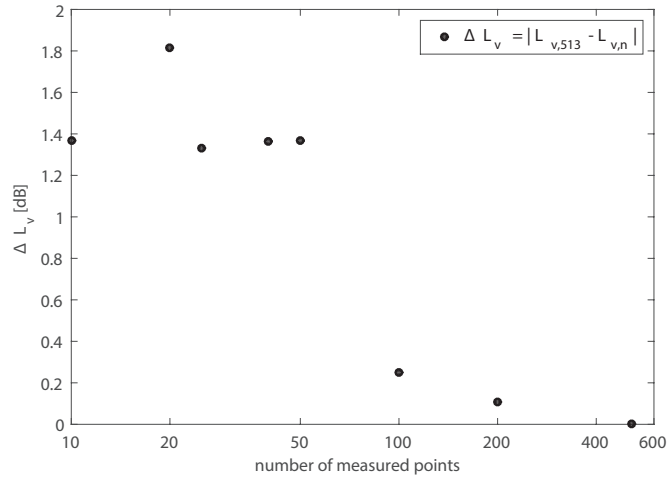


Figure 4.13: Overall velocity level difference  $\Delta L_V$  between the level averaged over the entire set of 513 points and the level averaged over (n) measurement positions randomly distributed on the surface of the panel CLT80\_b.

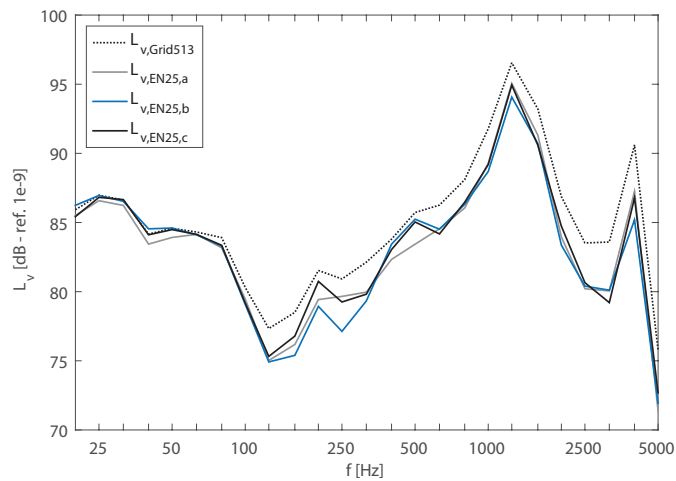


Figure 4.14: Comparison between the mean square velocity averaged over a grid of 513 points and over a random distribution of measurement positions chosen according to the requirements of EN 10848-1. The results, in one-third octave bands, refer to plate CLT80\_b mechanically excited.

## 4.4 Mechanical characterisation of CLT plate

The dynamic behaviour of CLT plates is known to be orthotropic, therefore the elastic parameters, and the stiffness properties, are direction dependent [114, 96]. The wave velocity has to be evaluated for many angles over the plate surface to analyse the propagation along different directions separately. The aim of this work is to present a fast and non-destructive method to investigate the elastic and stiffness properties of particular orthotropic elements using wave propagation analysis. The stiffness properties expressed as structural wavenumbers, have been used as input data to model sound radiation and sound transmission of CLT plates. The flexural wave velocity was measured on a three-ply cross-laminated timber plate for different propagation angles, instead of cutting beams along those directions [115]. Consequently, due to its non-destructive nature, the method can be applied either in-situ or in laboratory. Only propagating wave are taken into account, neglecting the reflection from the discontinuities. Therefore this method is not dependent on the boundary conditions of the panel.

### 4.4.1 Experimental flexural wave analysis

The frequency-dependent velocity of a propagating flexural wave was experimentally determined for the plate CLT80\_b. The propagating flexural waves were induced into the plate by a B&K 4809 vibration exciter driven by short sinusoidal pulses (2.5 cycles). The central frequency was varied from 100 Hz to 3100 Hz at 40 Hz steps. The transverse acceleration was measured by five PCB-353B15 accelerometers (10 mV/g) aligned with the excitation point and equally spaced 10 centimetres apart, as sketched in Figure 4.15. In order to avoid the influence of the vibrational near-field and to consider only the propagating wave neglecting the evanescent component, the closest accelerometer was placed 50 centimetres from the excitation point. The signals were generated and acquired by a National Instruments data acquisition system controlled with an in-house implemented software. Each measurement was performed for 5 different angles, from 0 to  $\pi/2$  radians, to investigate the dependency of the wave velocity upon the propagation direction.

To evaluate the flexural wave velocity each set of measured data was analysed with two different methods. The wave velocity can be determined by evaluating the phase difference between each pair of adjoining transducers. In order to consider only the direct incoming wave the measured signals must be windowed in the time domain, removing reflections from the edges. However, the time window should be long enough allowing the propagating wave to reach the furthest measurement point. It is appropriate to shrink the time window as the frequency increases, since the length of the signal reduces. The window size is thus determined for each investigated frequency

#### 4.4. Mechanical characterisation of CLT plate

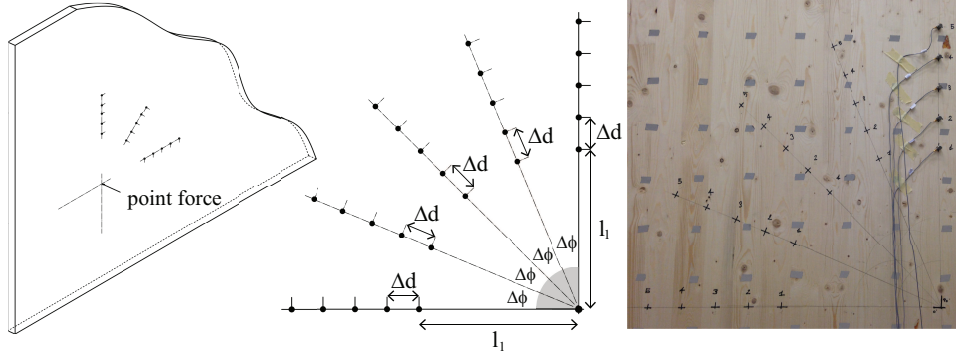


Figure 4.15: Experimental setup for different propagation angles at steps of  $\Delta\phi = \pi/8$ . The first measurement position is placed at a minimum distance  $l_1 = 50$  cm from the excitation point to avoid near field effects and the accelerometers are equally spaced:  $\Delta d = 10$  cm.

as a function of the first positive peak, detected in the time domain, of the incoming pulse. A clear description of the window size effects on the measurements can be found in [116], where the phase difference method was used to investigate the stiffness properties of building components. The phase difference is evaluated between each pair of consecutive accelerometers, by performing an FFT on the windowed signals. For each frequency the real part of the bending wavenumber, hence the wave velocity, can be evaluated by dividing the measured phase shift  $\Delta\varphi$  by the spacing  $\Delta d$ , and averaging over the accelerometer positions:

$$\text{Re}\{k_B(\omega)\} = \frac{1}{n_p - 1} \sum_{i=1}^{n_p-1} \left( -\frac{\Delta\varphi_{i,i+1}}{\Delta d_{i,i+1}} \right) \quad (4.6)$$

$$\text{Re}\{c_B(\omega)\} = \frac{\omega}{\text{Re}\{k_B(\omega)\}} \quad (4.7)$$

where  $n_p$  indicates the number of accelerometers, in this case  $n_p = 5$ . In the second method, the wave velocity is determined directly from the time of flight difference between neighbouring accelerometers. The measured data were first smoothed by applying a second order Savitzky-Golay polynomial filter in order to have a better signal to noise ratio, then the time of arrival of the first positive peak was determined for each acceleration signal. The time of flight is evaluated as the difference between the arrival time of two consecutive accelerometers:  $\Delta t_{i,i+1} = t_{i+1} - t_i$ . Assuming the dissipation to be negligible for small distances, the real part of the wave velocity is estimated by averaging over  $(n_p - 1)$  pairs of neighbouring accelerometers, the ratio of the spacing between two transducers  $\Delta d_{i,i+1}$  to the related time



#### 4.4. Mechanical characterisation of CLT plate

---

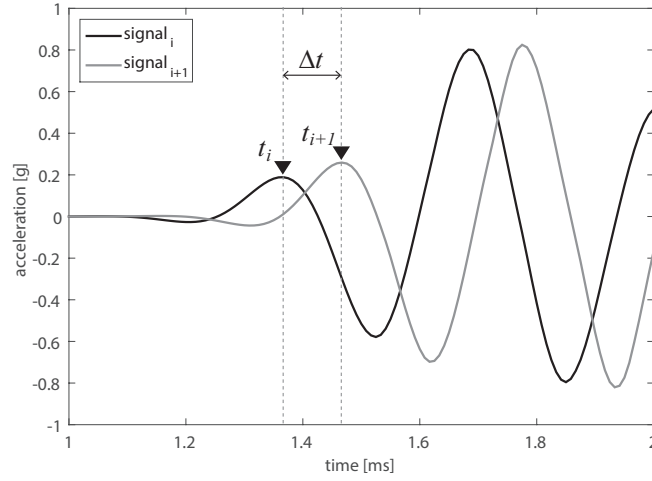


Figure 4.16: Evaluation of the time of flight of a flexural wave between two consecutive measurement positions:  $f = 3100 \text{ Hz} - \phi = \pi/2$ .

of flight:

$$\text{Re}\{c_B(\omega)\} = \frac{1}{n_p - 1} \sum_{i=1}^{n_p-1} \left( \frac{\Delta d_{i,i+1}}{\Delta t_{i,i+1}} \right) \quad (4.8)$$

An example of the determination of the time of flight difference between a pair of consecutive transducers is given in Figure 4.16. Both methods assume that all the reflections are removed from the signal by the time window and that the imaginary part of the wave velocity is negligible. As it will be clear from the experimental results presented in the next section, the phase difference method is more reliable in the low-mid frequency range, while the time of flight analysis is more appropriate at high frequencies. The spacing between the transducers should be much smaller than the bending wavelength to correctly evaluate the phase shift between the signals. In order to reduce the dispersion of the experimental results in the entire frequency range, the two data sets were combined using a cut-off frequency:  $f_{co} = 1500 \text{ Hz}$ . The measured wave velocities were fitted to obtain continuous smooth curves within the frequency range 50 – 5000 Hz, using Mindlin’s dispersion relation given in equation (2.26). A fitting algorithm implemented in Matlab R2014b, based on non-linear regression `nlinfit`, returns the estimated coefficients,  $c_L$  and  $c_S$ , for which the dispersion relation best fits the measured values. The resulting coefficients of the fitting algorithm represent the plate longitudinal and shear waves velocities, introduced in equations (2.1), and (2.2). From the values of  $c_L$  and  $c_S$  it is possible to derive directly the elastic  $E(\phi)$  and

the shear  $G(\phi)$  moduli for all the investigated propagation directions:

$$E_{\phi_i} = \rho c_{L,\phi_i}^2 (1 - \nu^2) \quad (4.9)$$

$$G_{\phi_i} = \rho c_{S,\phi_i}^2 \quad (4.10)$$

Sometimes, for engineering applications, simplified approaches are preferred over the more sophisticated ones. Simplified theories do not rigorously describe the structure dynamics, although they provide accurate approximated results in a relatively short computational time. Solving the equations of motion for an orthotropic thick plate, under Mindlin's assumptions, would require a great effort and the knowledge of much more input data as described in Ref. [117], therefore sound prediction models for CLT plates have been derived under the simplified thin plate theory. To compensate for the fact that the effects of rotational inertia and the shear deformation are neglected, the structure needs to be described by using frequency dependent properties, that can be derived from the experimental wave velocity measured along the principal directions [96]. The apparent frequency-dependent elastic properties along the principal directions  $E_x$  and  $E_y$  can be easily estimated from the thin plate dispersion relation given in equation (2.10) as:

$$\begin{aligned} E_x &= \frac{12\rho c_{exp,x}^4 (1 - \nu^2)}{h^2\omega^2} \\ E_y &= \frac{12\rho c_{exp,y}^4 (1 - \nu^2)}{h^2\omega^2} \end{aligned} \quad (4.11)$$

To account for the orthotropic behaviour of the CLT plate the elliptic model introduced in section 3.7 is adopted, assuming the bending wavenumbers along the principal directions to be independent. At any propagation angle  $\phi$ , the bending wavenumbers are derived from the experimental wavenumbers, measured along the  $x$ -direction ( $\phi = 0$ ) and the  $y$ -direction ( $\phi = \pi/2$ ), as given in equation (3.62). The direction-dependent bending stiffness can be approximated by using equation (3.65).

#### 4.4.2 Experimental results

The apparent parameters derived from the fitted wave velocity using the simplified thin plate dispersion relation are frequency dependent, as found in other studies when simplified assumptions are applied over more sophisticated theories for thick or composite plates [118, 57]. The frequency dependency of the apparent elastic modulus, or the apparent bending stiffness, takes into account that the plate dynamics at high frequency is mostly governed by the shear deformation, which is neglected in the classical plate theory. The apparent elastic moduli along the principal directions are plotted in Figure 4.17. The frequency dependent properties are compared to the elastic constant derived from the longitudinal wave velocity  $c_L$  resulting

#### 4.4. Mechanical characterisation of CLT plate

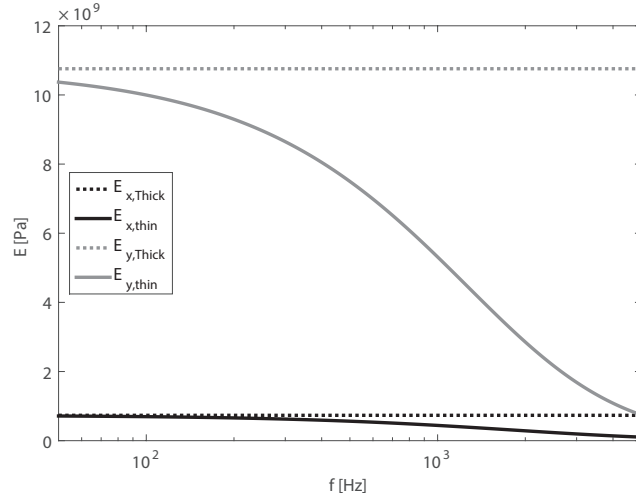


Figure 4.17: Comparison between the frequency dependent elastic properties of an equivalent thin orthotropic plate and the elastic constants derived using Mindlin's thick plate theory, associated with the principal directions.

Table 4.2: CLT's elastic constants for different propagation angles

$\phi$ [rad]	0	$\pi/8$	$\pi/4$	$3\pi/8$	$\pi/2$
$E$ [Pa]	$7.34e+08$	$9.68e+08$	$1.66e+09$	$3.80e+09$	$1.08e+10$
$G$ [Pa]	$2.40e+08$	$4.84e+08$	$2.52e+08$	$4.96e+08$	$5.72e+08$

from the fitting algorithm. The elastic and the shear moduli experimentally determined for different directions are reported in Table 4.2. The elastic modulus and the shear moduli along the  $x$ -axis,  $\phi = 0$ , have a comparable order of magnitude, while along the  $y$ -axis,  $\phi = \pi/2$  the shear modulus is almost two orders of magnitude lower than the elastic modulus. For this reason, the equivalent elastic properties along this direction, as the frequency increases, exhibit a more emphasised reduction than in the opposite direction, and the same is obviously valid for the apparent bending stiffness. These findings agree very well with the results from a recent study performed on cross-laminated timber beams using a modal analysis approach [119, 96].

To demonstrate the suitability of this approach for the investigated CLT plate, the theoretical bending wavenumbers obtained using the elliptic model were compared with the experimental values, for different propagation angles at various frequencies. The comparison between experimental and numerical data in wavenumber space, given in Figure 4.18, proves that

#### 4.4. Mechanical characterisation of CLT plate

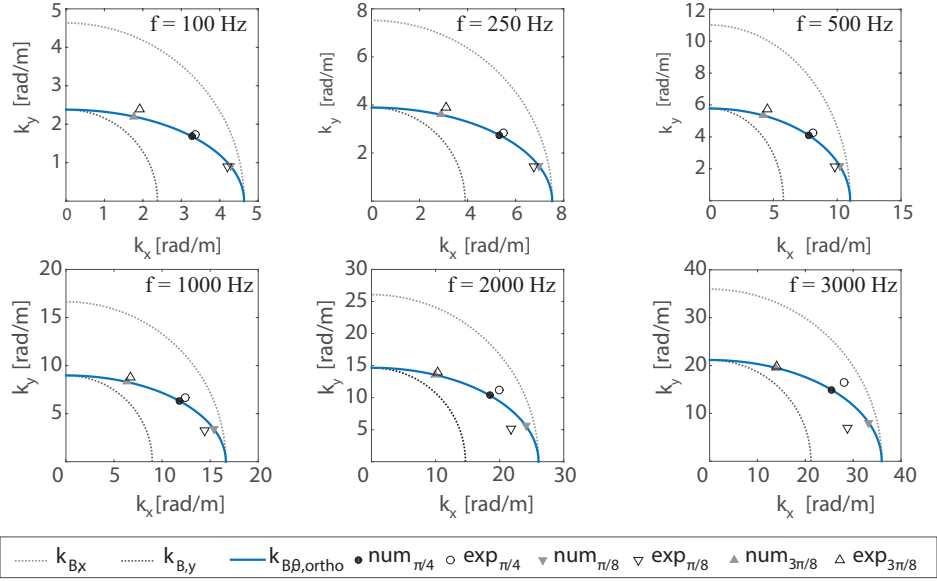


Figure 4.18: Elliptic model: comparison between the elliptic and the experimental wavenumbers, determined for the angles:  $\pi/8$ ,  $\pi/4$  and  $3\pi/8$ ; at the frequencies: 100 Hz; 200 Hz, 500 Hz, 1000 Hz, 2000 Hz and 3000 Hz.

the elliptic model is a reliable approximation to describe the orthotropic behaviour, showing a remarkably good agreement up to 1000 Hz. At higher frequencies the experimental wavenumbers slightly deviate from the predicted ellipse, consistent with the results of the analysis of wood material properties presented in Ref. [120]. Above 1000 Hz, the measured wavenumber along the  $\phi = \pi/4$  direction is larger than the estimated value, whereas for  $\phi = \pi/8$  the experimental wavenumbers is smaller than the numerical one. In other words, at high frequencies the elliptic model tends to overestimate the wave velocity propagating at  $\phi = \pi/4$  while it underestimates the wave velocity along the direction  $\phi = \pi/8$ . However, it should be noted that in the high frequency range the standard deviation of the measured velocity is significantly higher and of the same order of magnitude as the difference between the experimental and estimated wavenumbers. A similar comparison, with consistent results, is presented in Figure 4.19. The apparent bending stiffness, derived in equation (3.65), is compared with the values directly computed from the experimental wavenumber, for different angles and at different frequencies. The frequency and direction dependent apparent bending stiffness of the orthotropic cross-laminated timber plate is presented in Figure 4.20. A comparison is made between the approximated stiffness, function of the bending wavenumbers elliptically interpolated, and the orthotropic stiffness computed using equation (3.64). In the latter case to determine the effective

#### 4.4. Mechanical characterisation of CLT plate

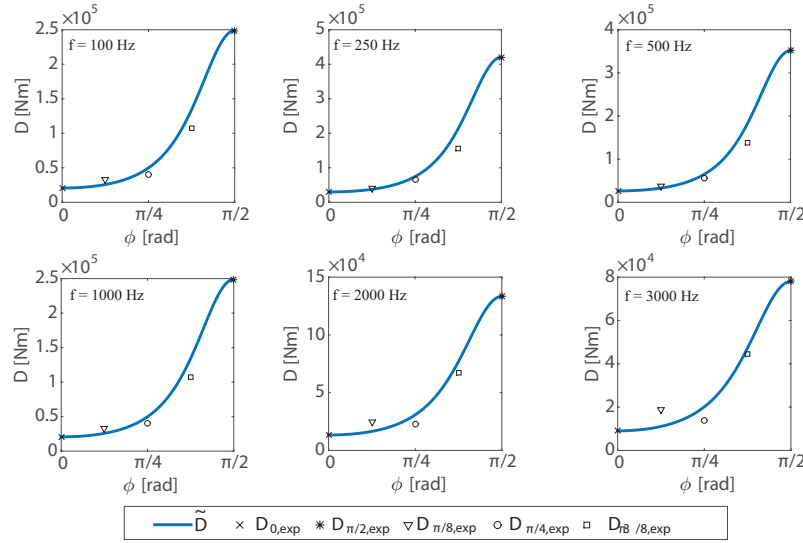


Figure 4.19: Elliptic model: comparison between the elliptic and the experimental bending stiffness, determined for the angles:  $\pi/8$ ,  $\pi/4$  and  $3\pi/8$ ; at the frequencies: 100 Hz; 200 Hz, 500 Hz, 1000 Hz, 2000 Hz and 3000 Hz.

torsional stiffness  $B$  the in-plane shear modulus was approximated as a function of the elastic moduli associated with the principle directions, as given in equation (A.7). The main difference is found in the bending stiffness decay associated with the transition between the two principle directions. The approximated bending stiffness exhibit a steeper reduction as the propagation angle approaches  $\phi = 0$ , resulting, for the intermediate directions, lower than the orthotropic bending stiffness computed from equation (3.64), which exhibit a softer decay.

Finally the flexural wave velocity measured along five propagation directions are presented. The propagation angles were investigated from  $\phi = 0$  to  $\phi = \pi/2$  at steps of  $\pi/8$  radians. The velocity obtained from the phase difference methods or by evaluating the time of flight difference are compared in the left side graphs, named a). The experimental data set, derived from the combination of these results by using a cut off frequency  $f_{co} = 1500$  Hz, were fitted using Mindlin's wave dispersion relation, given in equation (2.26), and are plotted in the right-hand side graphs named b), together with the shear wave velocity  $\kappa_{CS}$ . The fitted curves agree very well with the experimental data, as shown in Figure 4.21-4.25. Moreover the fitting method proved to be efficient, since the final results are independent from the used initial guess value, even if the frequency step in the measured data vector is increased from 40 Hz to 160 Hz, as shown in Figure 4.26.

#### 4.4. Mechanical characterisation of CLT plate

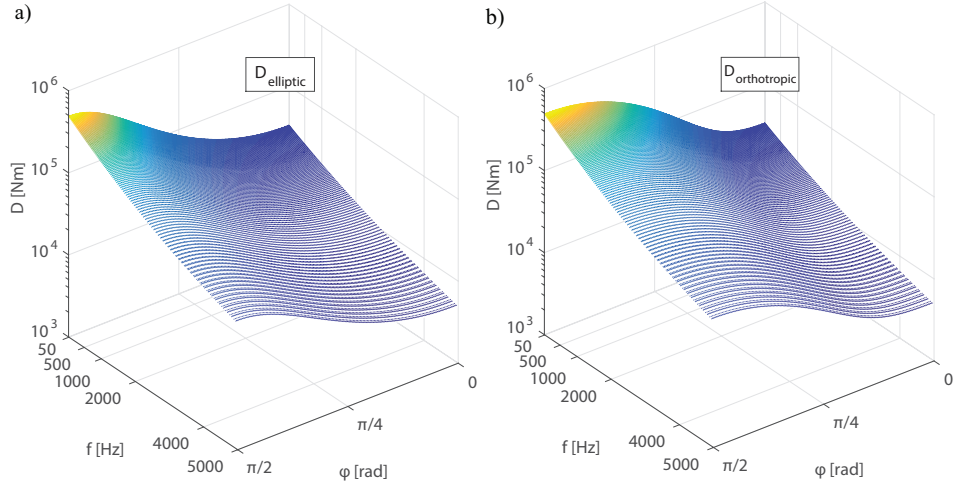


Figure 4.20: CLT plate bending stiffness frequency and direction dependent: a) elliptic approximation using equation (3.65); b) thin plate orthotropic bending stiffness computed using equations (3.64)

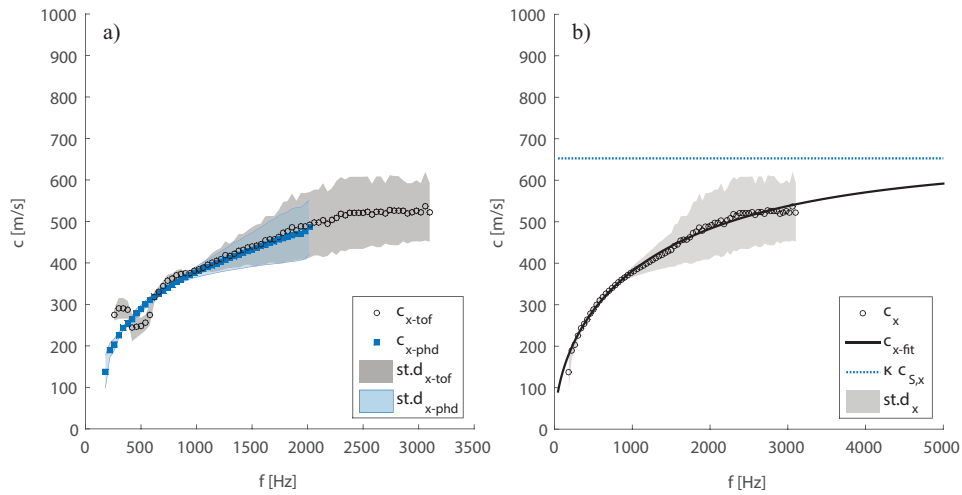


Figure 4.21: a) – Experimental wave velocity determined with the phase difference (*phd*) and the time of flight (*tof*) methods. b) – Curve fitting of the experimental wave velocity using Mindlin's dispersion relation. The shaded area represents the measured data standard deviation. Propagation angle:  $\phi = 0$

#### 4.4. Mechanical characterisation of CLT plate

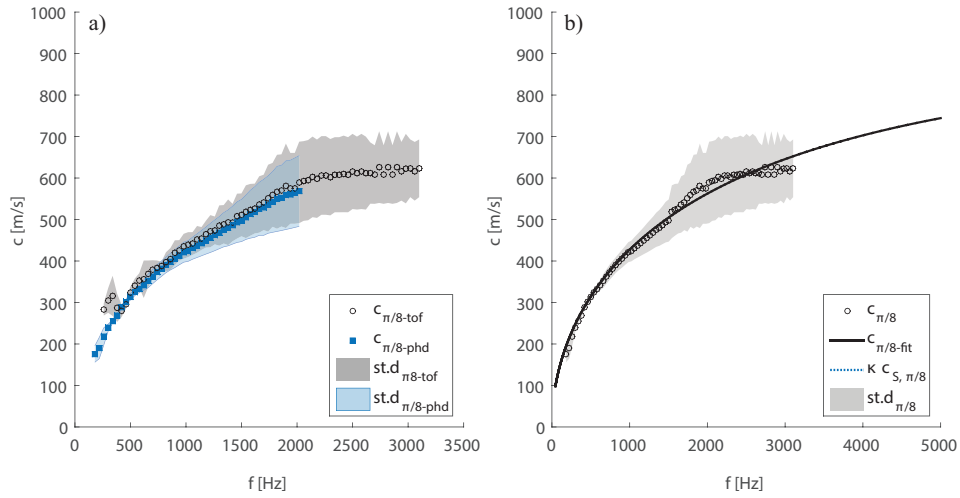


Figure 4.22: a) – Experimental wave velocity determined with the phase difference (*phd*) and the time of flight (*tof*) methods. b) – Curve fitting of the experimental wave velocity using Mindlin's dispersion relation. The shaded area represents the measured data standard deviation. Propagation angle:  $\phi = \pi/8$

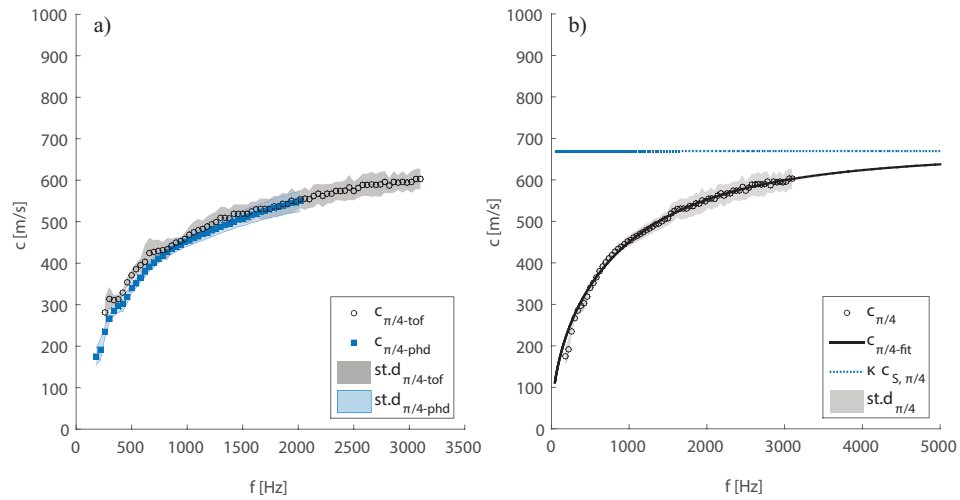


Figure 4.23: a) – Experimental wave velocity determined with the phase difference (*phd*) and the time of flight (*tof*) methods. b) – Curve fitting of the experimental wave velocity using Mindlin's dispersion relation. The shaded area represents the measured data standard deviation. Propagation angle:  $\phi = \pi/4$

#### 4.4. Mechanical characterisation of CLT plate

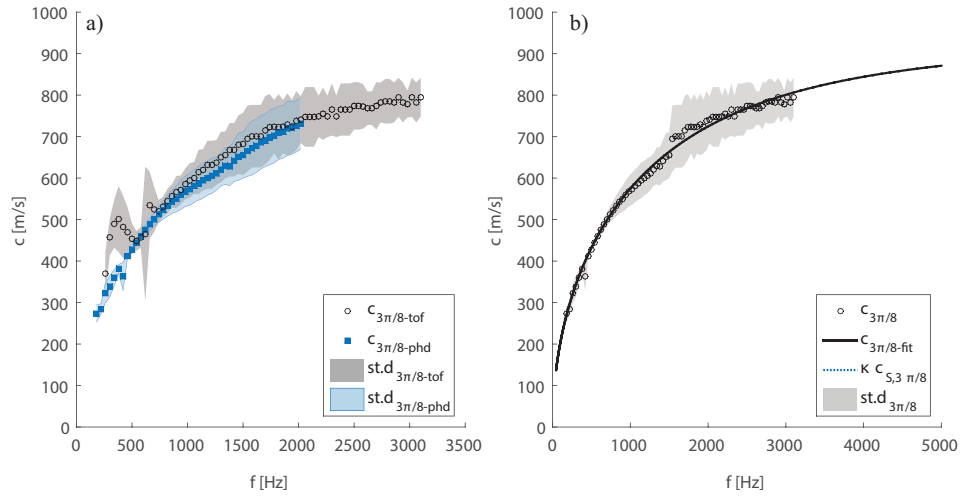


Figure 4.24: a) – Experimental wave velocity determined with the phase difference (*phd*) and the time of flight (*tof*) methods. b) – Curve fitting of the experimental wave velocity using Mindlin's dispersion relation. The shaded area represents the measured data standard deviation. Propagation angle:  $\phi = 3\pi/8$

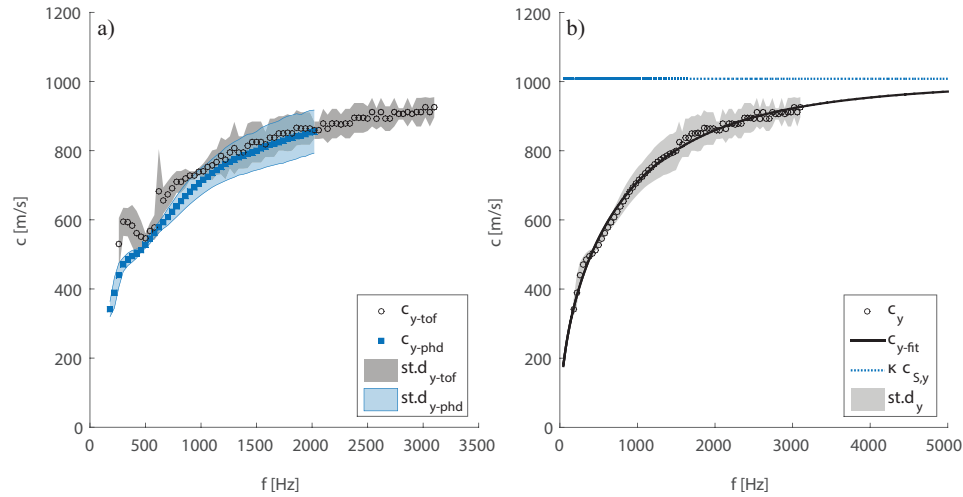


Figure 4.25: a) – Experimental wave velocity determined with the phase difference (*phd*) and the time of flight (*tof*) methods. b) – Curve fitting of the experimental wave velocity using Mindlin's dispersion relation. The shaded area represents the measured data standard deviation. Propagation angle:  $\phi = \pi/2$



#### 4.4. Mechanical characterisation of CLT plate

---

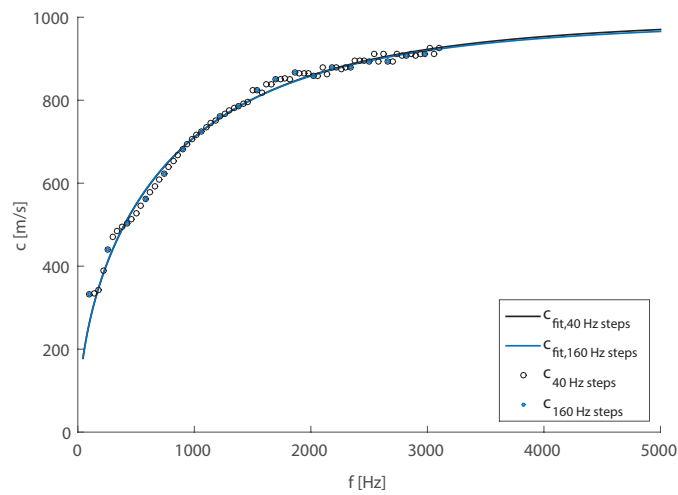


Figure 4.26: Comparison between wave velocity obtained by using an experimental frequency vector with regular steps of 40 Hz and steps of 160 Hz, within the range 100 – 3150 Hz. Propagation angle:  $\phi = \pi/2$

## 4.5 Validation of sound radiation models

The validation of the prediction models presented in Chapter 3 has been performed in two steps. A preliminary code verification was performed by comparing the results presented in the acknowledged papers with the data obtained from the models implemented for orthotropic plates. In particular, the code of the analytical model, described in section 3.4, was verified by computing the radiation efficiency of a steel plate, presented by Foin et al. in Figure 2 of reference [17], either considering the fluid loading effect, or by approximating the radiation impedance matrix  $Z_{mnpq}$  with the self radiation resistance  $R_{mn}$ . As shown in Figure 4.27, the radiation efficiency obtained calculating the radiation impedance matrix agrees very well with the curve presented in Ref. [17], except for minor discrepancies due to different frequency vectors used for the computation. The approximated radiation efficiency is reported as well, in order to show the influence of the fluid loading effect on a lightweight steel plate surrounded by the air. In order to verify the code based on the modal summation approach, described in section 3.5.2, the radiation efficiency of a rectangular aluminium plate was computed and compared with the results presented by Xie et al. in Figure 3 of Ref. [19]. The average radiation efficiency, shown in Figure 4.28 together with the modal radiation efficiency, matches very well with the results obtained by Xie et al. in Ref. [19]. These models, which are specifically developed for orthotropic plates, can be applied to isotropic materials by setting equal stiffness properties along the two principle directions. A preliminary code checking of the modal-average model was performed by computing the radiation efficiency of a thin carbon laminate plate. The result, given in Figure 4.29, are in good agreement with the radiation efficiency presented for a simply supported plate, by Anderson and Bratos-Anderson in Figure 10 of Ref. [30].

The second validation step concerned the applicability of these models to orthotropic building structures, such as CLT plates. The validation process has been undertaken by comparing the predicted radiation efficiency with the experimental data measured on the plate CLT80\_b. The plate's stiffness properties, necessary as input data, were experimentally determined by means of a procedure based on structural wave analysis, as described in section 4.4.1. The measured wavenumbers  $k_x$  and  $k_y$  are given in Table 4.3, together with plate loss factor  $\eta$ . The plate damping can be taken into account using complex input data [121], such as elastic modulus, or bending stiffness, or bending wavenumber, given by:

$$E^* = E(1 + i\eta); \quad (4.12)$$

$$D^* = D(1 + i\eta); \quad (4.13)$$

$$k_B^* = \sqrt[4]{\frac{k_B^4}{(1 - i\eta)}}. \quad (4.14)$$

#### 4.5. Validation of sound radiation models

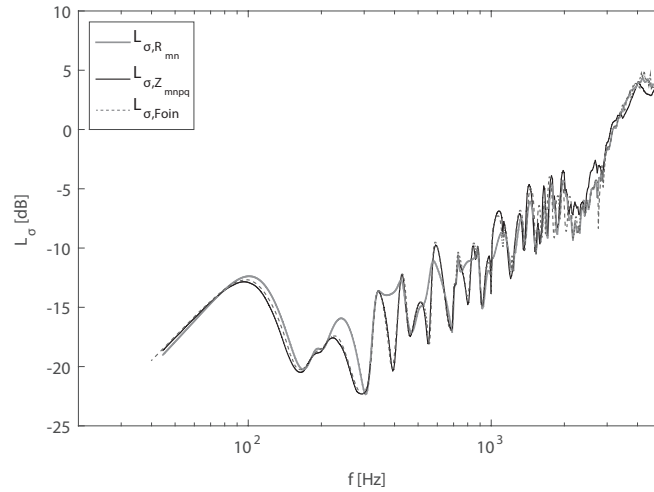


Figure 4.27: Comparison between the radiation index of a baffled steel plate obtained from the proposed code, either considering  $L_{\sigma,Z_{mnpq}}$  or neglecting  $L_{\sigma,R_{mn}}$  the fluid loading effect, and the results presented in Figure 2 of Ref. [17]  $L_{\sigma,Foin}$ .

The loss factor  $\eta$  of the CLT plate was determined using the power injection method from point input force and acceleration, measured with an impedance head attached to the shaker stinger, as described in [122, 123, 124]. This method was derived from SEA power balance equations, and its accuracy has been proved in several papers [125, 126, 127], in which it was compared to other methods to determine the structural damping, such as the decay response method, or the half-power bandwidth method.

The analytical model is validated by comparing the numerical results with the radiation efficiency measured on the plate CLT80\_a for two distinct excitation positions:  $S_1 = (0.5, 0.8)$  and  $S_2 = (3.6, 0.9)$ . In Figure 4.30 the numerical and experimental results related to the source position  $S_1$  are compared in one-third octave band, while the curves given Figure 4.32 refer to the source position  $S_2$ . The numerical data compared with the experimental results have been obtained implementing the analytical model with 9 frequencies for each third octave band, and considering up to 25 nodal lines along the  $x$  and  $y$  directions. The criterion, usually adopted in BEM analysis, that the higher resonance should be at least double the critical frequency, is largely fulfilled and the computational cost is kept reasonably low. The results are obtained neglecting the effect of cross-modal coupling and approximating the radiation impedance matrix  $Z_{mnpq}$  with the diagonal terms of the radiation resistance matrix  $R_{mn}$ . The influence of the fluid loading on CLT elements is almost negligible, as shown in Figure 4.31 by comparing

#### 4.5. Validation of sound radiation models

---

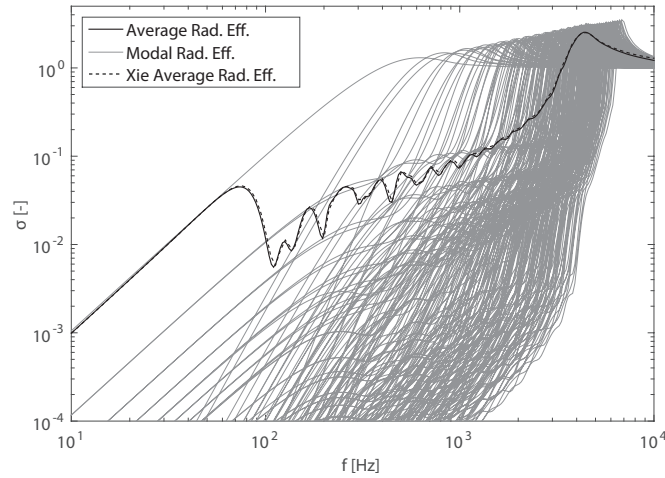


Figure 4.28: Modal and average radiation efficiency of an aluminium plate, obtained from the code based on the modal summation approach. The average radiation efficiency is compared with the results presented in Figure 3 of Ref. [19].

the plate's radiation efficiency computed either considering the radiation impedance  $Z_{mnpq}$ , or the self-radiation resistance  $R_{mn}$ , in one-third octave bands. Moreover, the small influence of fluid loading is proved in Annex B by comparing the results, both in third-octave band and in narrow band, for all the exciting sources. A good agreement is found between numerical data and experimental results for both the source positions. The first coincidence, associated with the vertical stiffest direction, and the critical frequency are well detected. The peaks and the dips of the radiation efficiency below the critical condition are approximated with satisfying accuracy. Nevertheless the predicted radiation efficiency is an overestimation of the experimental results, and discrepancies up to 3 dB can be found in certain frequency bands. The main cause is found in the assumption of simply supported boundaries, which does not rigorously represent the complexity of the CLT plate's mounting conditions. The fact that in the experimental setup the translational motion is not completely prevented at the edges, reducing the sound energy actually radiated, as discussed in the next section.

The analytical approach also allows to predict the radiation efficiency of an acoustically excited plate, either for the simple case of an incident sound wave, or considering a diffuse sound field. In Figure 4.33 the numerical results obtained with the analytical model for a diffuse incident sound field are compared with the experimental results. The contribution of non-resonant modes below the critical frequency, which falls around 1000 Hz is clearly

#### 4.5. Validation of sound radiation models

---

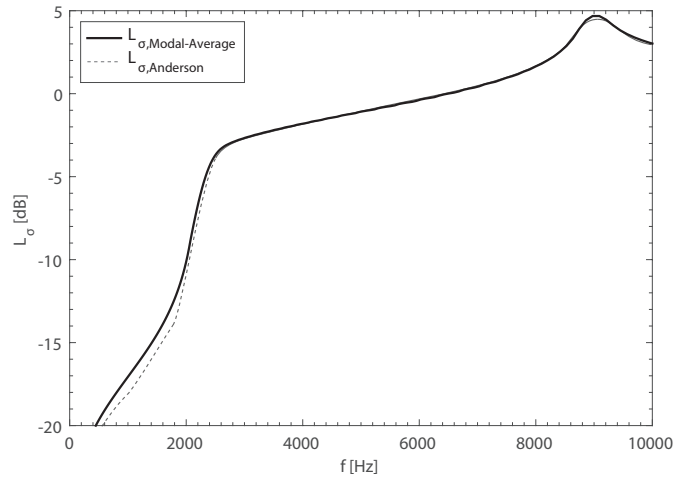


Figure 4.29: Average radiation index of an orthotropic carbon laminate plate, obtained from the proposed modal-average approach, compared with the results presented in Figure 10 of Ref. [30].

shown. The influence of the different boundary conditions below the critical frequency seems to be more relevant than for the radiation due to mechanical force. In this frequency range the numerical radiation index represents an overestimation of the experimental results, with differences up to 6 dB in certain bands. Moreover, the dips and peaks are slightly shifted, falling in a lower third octave band. No experimental results are given below 100 Hz band, since the energy of the diffuse sound field incident on the plate was not enough to have a good signal to noise ratio in order to correctly evaluate the radiation efficiency, thus a comparison would not be reliable.

The radiation efficiency computed by means of the modal summation approach, represents the average over all the possible source positions, which reduces the contribution of the fluid loading effect. Since this model has been already successfully applied to compute the radiation efficiency of orthotropic structures, it has been used as basis for comparison with the average radiation efficiency of the CLT plate, obtained from the analytical approach averaging the results over the two source positions. The modal average radiation efficiency, obtained from these two approaches, is given in narrow band in Figure 4.34, together with the radiation efficiency of each mode  $(m, n)$  considered. The results are in good agreement, although the fluid loading has been neglected in the analytical model. This allows for a faster computation, reducing the time to approximately 1.5% the time required to calculate the impedance matrix coefficients, obtaining an algorithm performance almost identical to the one provided by modal summation approach. To further

#### 4.5. Validation of sound radiation models

---

Table 4.3: Experimental bending wavenumbers and loss factor used as input data to model the cross-laminated timber plate CLT80\_b

$f$ [Hz]	$k_x$ [m]	$k_y$ [m]	$\eta$ [-]	$f$ [Hz]	$k_x$ [m]	$k_y$ [m]	$\eta$ [-]
40	2.938	1.503	0.08	500	10.967	5.742	0.04
50	3.288	1.684	0.08	630	12.512	6.59	0.03
63	3.697	1.895	0.08	800	14.440	7.674	0.03
80	4.191	2.149	0.08	1000	16.479	8.849	0.03
100	4.679	2.402	0.08	1250	18.907	10.284	0.03
125	5.228	2.687	0.08	1600	22.353	12.348	0.03
160	5.986	3.082	0.07	2000	25.993	14.620	0.03
200	6.701	3.457	0.07	2500	30.468	17.485	0.03
250	7.512	3.885	0.07	3150	36.313	21.285	0.03
315	8.504	4.411	0.06	4000	44.015	26.343	0.02
400	9.721	5.063	0.05	5000	52.994	32.329	0.02

reduce the computational cost, all the algorithms implement a frequency interpolation proposed by Foin [17] to compute either the radiation impedance  $Z_{mnpq}$  or the self radiation resistance  $R_{mn}$ .

The experimental radiation efficiency averaged over the two source positions was used to validate the modal-average radiation model. The comparison between experimental and predicted radiation index is shown in Figure 4.35. The statistical model provides a good approximation of the radiation trend. It is possible to clearly detect the critical frequency although the numerical curve exhibits a sharper peak. The first coincidence, which falls within the 250 Hz frequency band, is not as pronounced as in the experimental data, but only identified by a slight change of the curve slope. With this model the radiation efficiency below the critical condition is not as accurately approximated as with the analytical approach, due to several effects that are not taken into account by the simplifying assumption of the model. The high modal density assumption, necessary to consider a continuous distribution of modes, is not verified within the entire frequency range. In fact, at low frequencies the vibrational field of the CLT plate surface is not diffuse, and only a few modes falls within the frequency bands. Moreover, below the first coincidence the sound is mainly radiated from the plate discontinuities, like the boundaries, that are assumed to be simply supported, which are more complex in the reality, as will be illustrated in the next section. Furthermore, the near field around the excitation point represents an additional discontinuity not considered by the model that might slightly enhance sound radiation. Nevertheless, this model gives helpful insights on the radiation behaviour of the orthotropic CLT plate, providing a reliable trend of the radiation efficiency. Finally the results obtained approximating the plate bending stiffness as a function of the elliptic interpolation of bending wavenumber, given

#### 4.5. Validation of sound radiation models

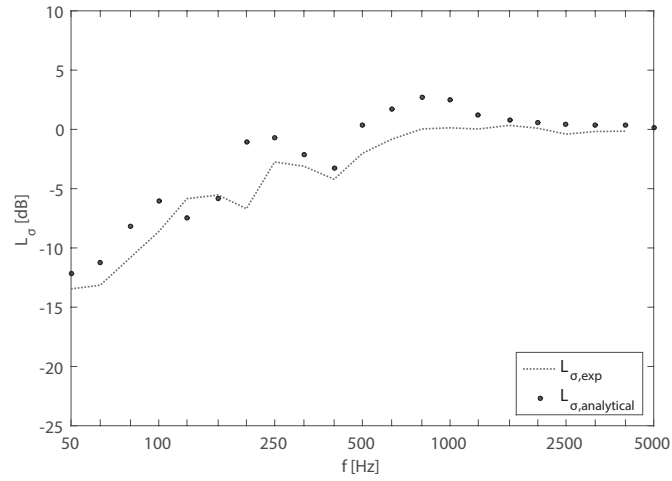


Figure 4.30: Radiation efficiency of a CLT plate: comparison between the analytical model results and experimental data related to the position of the exciting force  $S_1$ . Results presented in one-third octave bands.

in equation (3.65), are compared with the results obtained considering the orthotropic bending stiffness given in equation (3.64) in Figure 4.36. These

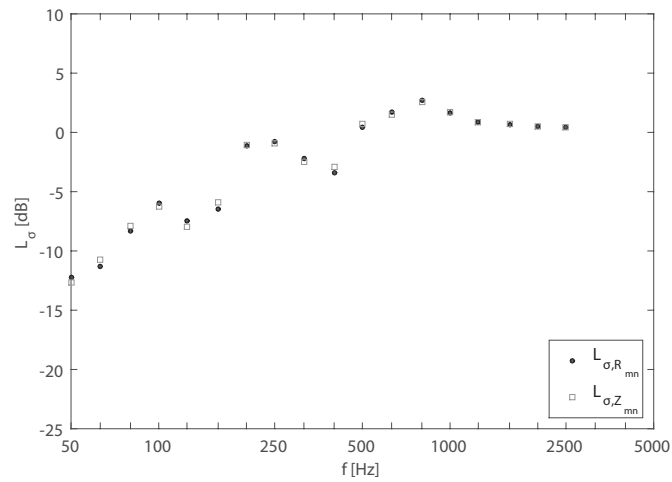


Figure 4.31: Comparison between the CLT plate's radiation index computed considering the fluid loading  $L_{\sigma,Z_{mnpq}}$  and the approximated results computed considering the self radiation resistance  $R_{\sigma,Z_{mnpq}}$ . Results obtained from the analytical model are presented in one-third octave bands and refers to exciting force  $S_1$ .

#### 4.5. Validation of sound radiation models

---

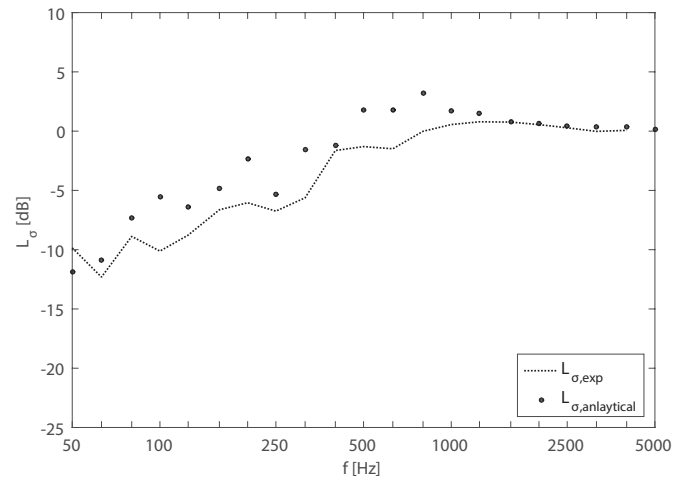


Figure 4.32: Radiation efficiency of a CLT plate: comparison between the analytical model results and experimental data related to the position of the exciting force  $S_2$ . Results presented in one-third octave bands.

two formulations provide consistent results, since no relevant differences are found in the modal-average radiation efficiency.



#### 4.5. Validation of sound radiation models

---

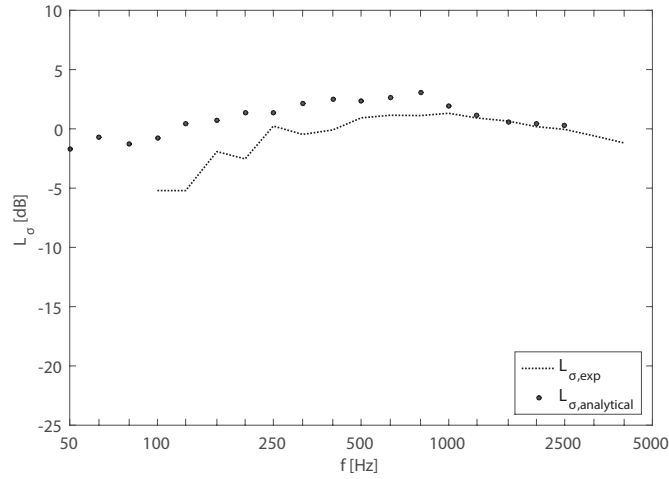


Figure 4.33: Radiation efficiency of a CLT plate: comparison between the analytical model results and experimental data obtained with a diffuse field excitation. Results presented in one-third octave bands.

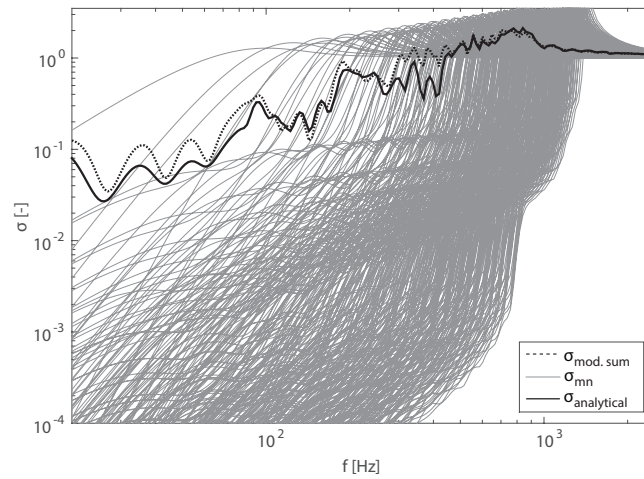


Figure 4.34: Radiation efficiency of a CLT plate: comparison between the numerical results obtained from the modal summation approach and from the analytical model averaged over two source positions. Results presented in narrow band.

#### 4.5. Validation of sound radiation models

---

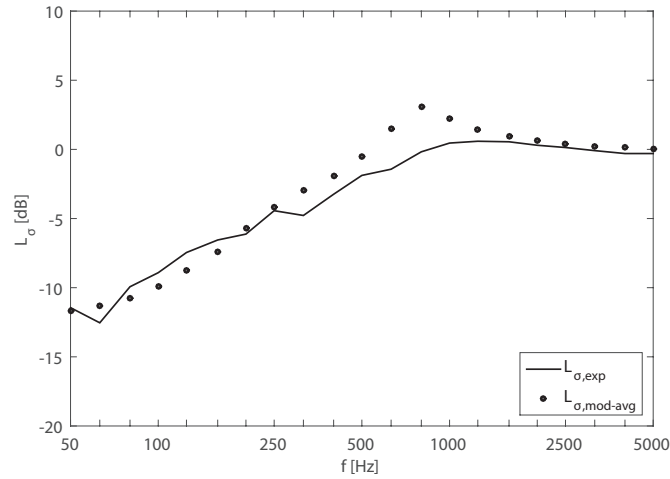


Figure 4.35: Radiation efficiency of a CLT plate: comparison between the numerical results obtained from the modal-average approach and experimental data averaged over two source positions. Results presented in one-third octave bands.

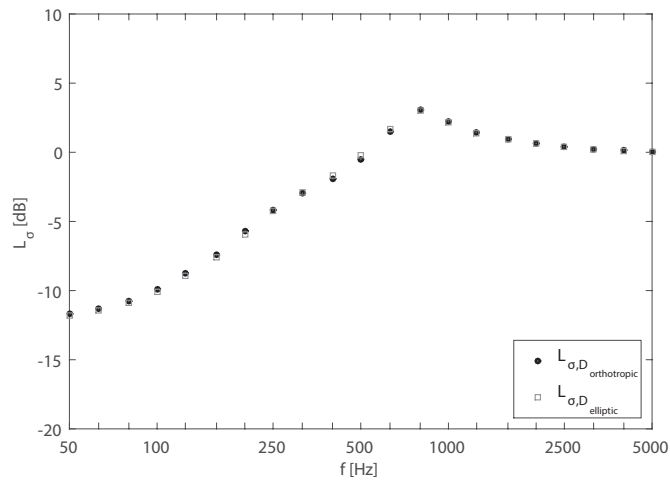


Figure 4.36: Radiation efficiency of a CLT plate: comparison between results obtained considering the orthotropic bending stiffness and its elliptic approximation. Results presented in one-third octave bands.

## 4.6 Plate boundary conditions

For all the implemented models the plate boundaries have been considered simply supported. This simplifying assumption provides an analytical solution of several equations, allowing for a faster computation. However, the real boundary conditions of the investigated plate are much more complex, as shown in Figure 4.3: at the bottom edge the plate is supported by a rigid frame whereas at all the other edges there is a small gap, sealed with elastic putty that does not completely prevent the out of plane translational motion of the plate. The influence of the boundary conditions on the radiation efficiency has been widely investigated. Gomperts analysed modal radiation of plates with general boundary conditions [128, 129], determining the plate's response as the product of the mode shapes of two orthogonal beams. Below the critical condition, Leppington et al. found an average increase of 3 dB in the radiation efficiency of a rectangular plate clamped on all edges compared to a simply supported plate [130]. Berry et al. proposed a method to compute sound power radiated from plates with arbitrary boundary conditions under point-force excitation, describing the displacement by means of a set of polynomial trial functions [10]. Beslin and Nicolas derived a method to describe plate bending modes for any kind of boundary condition, using a set of hierarchical trigonometric functions [68]. A thorough analysis of the influence of the boundary conditions on the sound radiation efficiency was recently published by Squicciarini et al. [131]. A comparison between simply supported, clamped, and free boundaries, shown that clamped plates are the most efficient radiators for all the frequencies above the first mode, while fully free plates exhibit the lowest radiation efficiency. Hence below the critical condition, a plate with free boundaries exhibit a lower radiation efficiency than a simply supported one. Above the critical frequency, the boundary conditions do not have significant influence on sound radiation. The CLT plate's motion, obtained by scanning the vibration velocity over the surface, reported in Figure 4.37 for mechanical excitation, and in Figure 4.38 for diffuse field excitation, clearly shows that the out of plane translation was not completely restrained along all the four edges, and particularly along the top edge. The plate's motion at the edges is relevant and proportional to the displacement measured in the center of the surface within the entire frequency range. The discrepancies highlighted between the experimental radiation efficiency and the results obtained from the analytical model Figure 4.30, 4.32 and 4.33, are perfectly in line with the findings of the study presented by Squicciarini, in which differences up to 25 dB between free and simply supported boundaries have been found. The plate's transverse motion induced by a mechanical source tends to reduce as the frequency increases, Figure 4.37. Under airborne excitation the plate exhibits a similar behaviour up to the critical frequency, where the vibrational field perfectly matches the incident sound field and the amplitude of the plate's motion

## 4.7. Conclusion

---

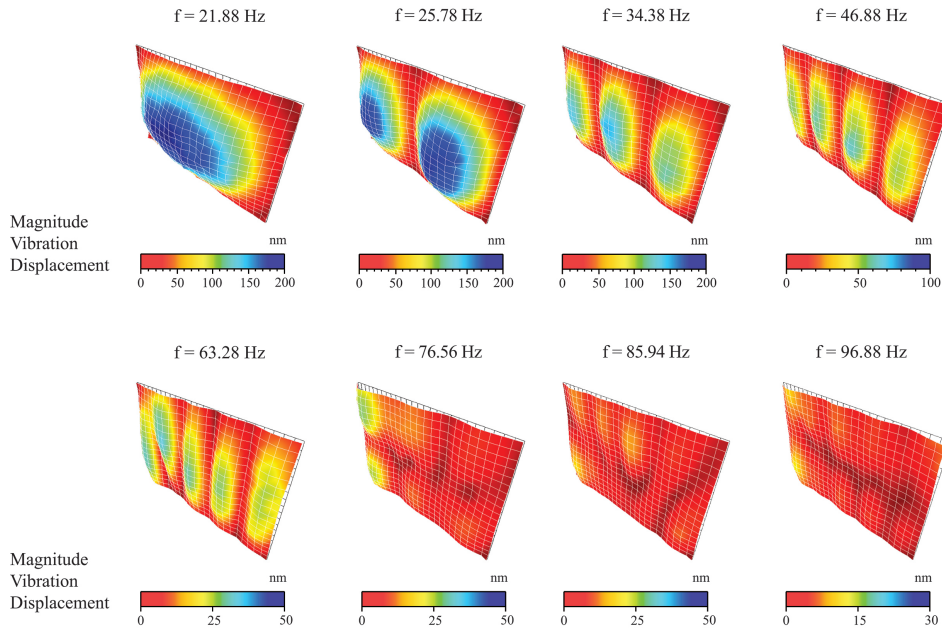


Figure 4.37: Plate measured displacements. Mechanical source  $S_1$

increases reaching its maximum, Figure 4.38. Around the critical condition the amplitude of the transverse displacement at the edges is of the same order of magnitude of the transverse displacement measured far from the boundaries, in the central area of the plate.

## 4.7 Conclusion

An experimental evaluation of the radiation efficiency has been presented on three three-ply CLT plates, since it represents an important descriptor and is often needed in building acoustic analysis as input data. CLT plates are known to be orthotropic elements, due to the layered structure. The CLT stiffness properties depend on the number of layers and the ratio of their thickness. The type of excitation strongly influences the plate radiation and the mechanisms that govern this process. When the plate is excited by a mechanical force, its response is governed by resonant modes, even though the vibrational near-field might give relevant a contribution below the critical frequency. Two of the investigated plates, CLT80\_a and CLT100, have different thickness and different surface mass, although, they exhibit a similar behaviour, with the critical condition falling within the 500 Hz frequency band. Orthotropic structures are characterised by two significant coincidence frequencies. In the plate CLT80\_b, these are shifted towards higher frequencies, in comparison to the other two structures. It means that

## 4.7. Conclusion

---

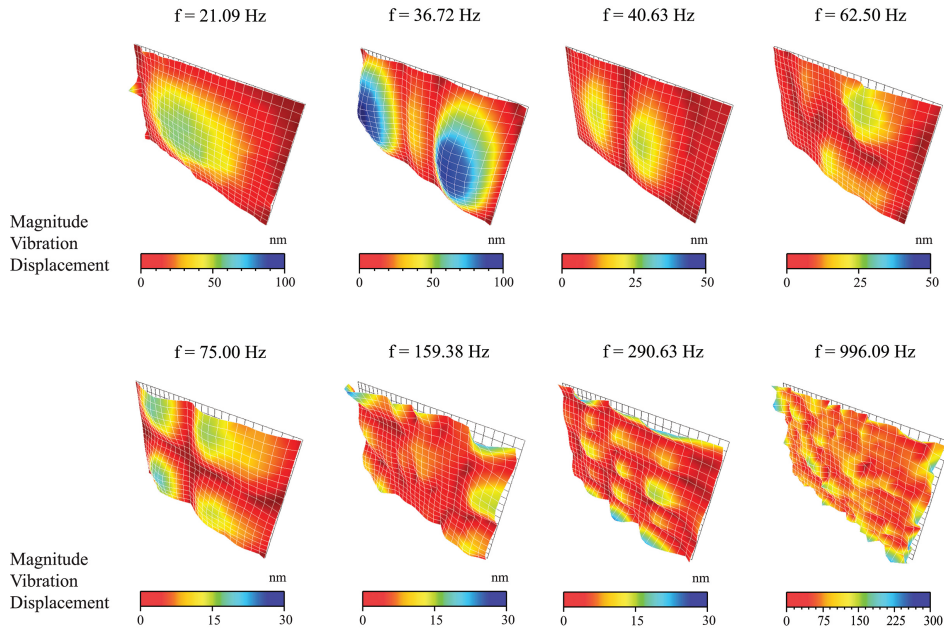


Figure 4.38: Plate measured displacements. Airborne excitation

this plate has a lower bending stiffness along both the principal directions. When a diffuse sound field is the exciting source, below the critical frequency the plates response is governed by a non-resonant field and similar radiation efficiency has been found for all the three structures. Above the critical condition the radiation efficiency tends to unity, both with mechanical, and airborne excitation. Two different methods to evaluate the radiated sound power have been compared, obtaining consistent results. The diffuse field approach estimates the sound power from the measured sound pressure, assuming a perfectly diffuse sound field in the receiving room. The discrete calculation method can be applied down to lower frequencies, since it requires only the complex vibration velocity measured on a grid of points on the plate surface. It assumes radiation into a free-field, thus influences due to the room are neglected. However, it might be time consuming when a large surface is investigated. The grid spacing between measurement positions determines the highest frequency limit for the applicability of the DCM. A comparison between grids with a different number of points and average spacing shows that when the distance between adjacent points is larger than half the wavelength at the coincidence, the discretisation of velocity field is not enough accurate. The average spacing should be smaller than half wavelength at the critical frequency, as stated by Hashimoto, otherwise the sound radiated by each single piston-like source will appear as uncorrelated. However, discrepancies in the results have been found also for a grid spacing

equal to one-quarter of the acoustic wavelength. This might represent a more restrictive limit of this method, that needs to be further investigated. Very often the mean square velocity of a vibrating plate is averaged over a certain number of measurement positions, randomly distributed on the surface, especially when accelerometers are used instead of a scanning laser vibrometer. To investigate the influence of the number of points and their distribution on the surface, a parametric analysis on the same set of data has been performed. As long as the number of measured positions is fairly high in relationship with the investigated surface, either a uniform grid, or a random distribution, provides a reliable spectrum of the mean square velocity. A first analysis, undertaken considering the absolute number of transducers randomly distributed on the plate with no regards for their reciprocal distance, shows that for a surface of approximately  $12.2 \text{ m}^2$  at least 100 measurement positions are necessary in order to reduce the differences with the data obtained from a narrow grid of 513 points. This represent an average radius distance between the measurement positions of approximately 38 cm. However, when a random distribution is used, the local position of each single transducer also plays an important role in the evaluation of the mean square velocity. Investigating different random distributions of measurement points, fulfilling the distances requirements given in the standard EN 10848-1, an underestimation of the mean square velocity was always found.

An experimental characterisation of the stiffness properties of an orthotropic CLT plate, based on flexural wave analysis, has been proposed. The wave velocity was evaluated using two different approaches. The phase difference method gives more accurate results in the low frequency range, while at high frequencies it is more convenient to determine the velocity from the time of flight difference, evaluated between neighbouring transducers. Using a non-linear fitting algorithm, the elastic and the shear moduli have been derived from the flexural wave velocities, measured along the plate's principal directions. Results show that the  $y$ -direction, associated with the vertically oriented outer layers fibres, is stiffer than the orthogonal  $x$ -direction. Moreover, the elastic modulus  $E_y$  is two orders of magnitude higher than the shear modulus  $G_{yz}$ , while along the  $x$ -direction the elastic and the shear moduli have a comparable order of magnitude. Furthermore, the bending stiffness along the principle directions of an equivalent thin plate has been determined from the experimental bending wavenumbers, by using Kirchhoff's dispersion relation. A frequency dependent apparent bending stiffness compensates the fact that, in thin plate theory, rotational inertia and shear deformation are neglected. The plate's apparent elastic properties decrease as the frequency increases. The frequency dependence is much more emphasised along the vertical direction, due to the greater difference between the elastic and the shear moduli. The orthotropic bending stiffness, approximated by an elliptic interpolation, is in good agreement

with the experimental data measured for different propagation angles. The stiffness properties of the equivalent thin plate has been used as input data to investigate the vibro-acoustic behaviour of a CLT panel.

The experimental radiation efficiency of the plate CLT80\_b was used to validate the prediction models. The analytical approach proved to give reliable results, approximating the radiation efficiency with a satisfying accuracy even below the critical frequency. Due to the different boundaries of the experimental setup from the simply supported condition assumed in the models, the analytical approach overestimates the radiation efficiency below the critical frequency, particularly when a diffuse sound field excitation is considered. This is in line with the findings of several studies regarding the boundary conditions influence on the plate response and sound radiation. In fact, the radiation efficiency increases due to an increase of the restraint degree at the edges. The accuracy provided by the analytical model is comparable with the one provided by the modal summation approach, already applied to orthotropic structures. Besides, the analytical model offers the possibility to consider specific positions for the mechanical force, and acoustic excitation. Moreover, it is possible to take into account the fluid loading effect, even if it does not have a significant influence on CLT panels. Approximating the radiation impedance with the self radiation resistance the computational effort required by the analytical model can be drastically reduced. Finally the modal-average radiation efficiency, computed considering only resonant modes, was compared to the experimental data providing a good approximation of the radiation trend. The modes are considered only at their resonance, therefore this model can be applied only for mechanically excited plates, neglecting the near-field contribution and the fluid loading effects. Moreover, the model assumes an high modal density in the entire frequency range. When this assumption it is not verified, especially in the low frequency range, the results accuracy is reduced. Although, the modal-average model represents an useful tool to perform preliminary analysis on orthotropic plates during the design process.

## Chapter 5

# Sound transmission through building elements

### 5.1 Introduction

Structures excited by an incident sound field, either an acoustic plane wave impinging with a certain angle  $\theta$  on the surface, or a random incidence acoustic field, can be regarded in terms of sound transmission. In this Chapter sound transmission through complex building partitions is investigated by means of a wave based approach. The transfer matrix method (TMM) represents one of the most efficient and powerful tools used to model the acoustic wave propagation through layered structures [132, 133], considering media of different nature. This method can be easily applied to investigate the sound insulation provided by multilayer structures, such as double leaf or lined walls, largely used in buildings. The background theory of the TMM is given in the next section, together with the fundamental equations necessary to implement a model to investigate structures with an arbitrary number of layers. The method has been applied to model the sound wave transmission through a CLT plate excited by a diffuse sound field. The results are validated with experimental data.

The influence of the different radiation mechanisms on sound transmission has been investigated in particular multilayer structures commonly used in buildings, known as External Thermal Insulation Composite System (*ETICS*). These systems are commonly used to achieve high thermal insulation performance in buildings. The external walls are lined with insulating slabs on which different finishings can be applied. The slabs are fixed to the fabric of the building by using both mortar or special resins, and mechanical fixings distributed over the surface of the basic wall. Furthermore, when a proper material is used, such as mineral wool, the *ETICS* system can also provide the acoustic performance required in buildings to meet the regulation requirements [134]. While great attention has been paid to the thermal



performance over the last ten years, thanks to the EU policy for energy efficiency of buildings, only a few acoustic experimental investigations have been done [135]. Moreover, the development of proper tools to perform an accurate acoustic analysis of such systems is still lacking. These multilayer systems can be treated as double panel structures with mechanical point connections. The structural bridges link the building wall to the thin finishing layer through the insulating material. Therefore, the theoretical sound insulation that would be provided by the element without mechanical fixings would be reduced, due to the structure-borne sound transmission via the mechanical connections. Despite the huge variety of models that can be found in the literature, none of them seems to be suitable for the *ETICS*, since they have been developed for lightweight structures. Moreover, they consider only thin plates and the cavity being either empty or filled with low-density porous or fibrous material, which can be modelled with good approximation using simplified theories. On the contrary, the *ETICS* is mounted on walls that need to be modelled as thick plates and high-density fibrous materials are involved, which cannot be simply approximated as equivalent fluids, but need to be modelled as poroelastic media using Biot's theory. A more general method, based on the TMM framework, has been developed in order to evaluate sound transmission through multilayer elements, constituted either by thin or thick plates, and poroelastic materials, also considering the presence of structural bridges. It is described in detail and verified with experimental results in section 5.4.

## 5.2 Transfer matrix method

The TMM solves a two-dimensional problem of a plane acoustic wave impinging on the surface ( $S_1$ ) of a layered element, as sketched in Figure 5.1. The general formalism of TMM can be expressed as:

$$V_{(S_1)} = [T] V_{(S_2)}. \quad (5.1)$$

The vector  $V_{(S_1)}$  represents all the variables needed to define the acoustic field on the surface ( $S_1$ ), such as pressure, particle velocity and stresses depending on the nature of the medium; while the vector  $V_{(S_2)}$  contains the descriptors related to each single layer and all the variables that define the acoustic fields on the surface ( $S_2$ ). The transfer matrix  $\mathbf{T}$  describes wave propagation through the stratified structure. The size of this matrix depends on the nature of each layer, such as fluid, thin plate, elastic solid, or poroelastic. In sound transmission analysis, the multilayer element is assumed to be extended by a semi-infinite fluid on both sides. It is possible to express the global transfer matrix  $\mathbf{D}$  to model the  $n$ -layers structure, having

## 5.2. Transfer matrix method

---

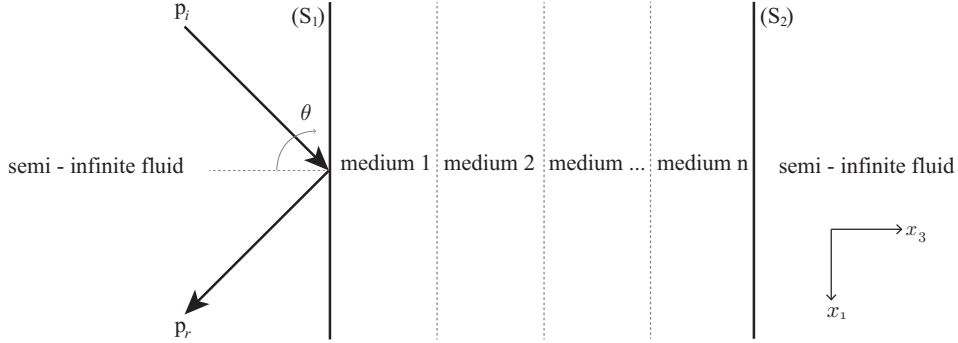


Figure 5.1: An acoustic wave impinging on a stratified structure with an incidence angle  $\theta$ . The multilayer element is surrounded by a semi-infinite fluid on both sides.

$(N + 1)$  rows and  $(N + 2)$  columns, as:

$$[D] = \begin{bmatrix} I_{fm_1} & J_{fm_1} T_{m_1} & & & [0] \\ [0] & I_{m_1 m_2} & J_{m_1 m_2} T_{m_2} & & [0] \\ & & \vdots & & \\ & [0] & & I_{m_{n-1} m_n} & J_{m_{n-1} m_n} T_{m_n} & [0] \\ & & [0] & & I_{m_n f} & J_{m_n f} \\ & & & [0] & & [-1 \quad Z_0 \cos^{-1} \theta] \end{bmatrix}, \quad (5.2)$$

where  $Z_0 = \rho_0 c_0$  represent the characteristic impedance of the fluid termination, which is a function of its density  $\rho_0$  and the speed of sound  $c_0$ . The coupling matrices  $\mathbf{I}_{ij}$  and  $\mathbf{J}_{ij}$ , describing the interface conditions between different layers, and the transfer matrices  $\mathbf{T}_{m_i}$  that describes the sound propagation through each different media, are reported in Annex D. The relationship between the acoustic pressure and the particle velocity of a sound wave impinging on a multilayer structure can be expressed by the surface impedance of the medium  $Z_S$ , which, as derived in Chapter 11 of Ref. [133], can be computed as:

$$Z_S = -\frac{\det[D_1]}{\det[D_2]}. \quad (5.3)$$

The matrices  $\mathbf{D}_1$  and  $\mathbf{D}_2$  are obtained by eliminating from  $\mathbf{D}$  the first and the second column respectively. For each incidence angle  $\theta$ , the complex reflection coefficient can be determined as:

$$\mathcal{R} = \frac{Z_S \cos \theta - Z_0}{Z_S \cos \theta + Z_0}. \quad (5.4)$$

### 5.3. Orthotropic elastic medium

---

Similarly, the complex transmission coefficient  $\mathcal{T}$  is given by:

$$\mathcal{T} = -(1 + \mathcal{R}) \frac{\det [D_{N+1}]}{\det [D_1]}. \quad (5.5)$$

The matrix  $\mathbf{D}_{N+1}$ , analogous to  $\mathbf{D}_1$  and  $\mathbf{D}_2$ , is obtained by the  $(N+1)^{th}$  column from the matrix  $\mathbf{D}$ , given in equation (5.2). For a given propagation angle  $\theta$  of the incident sound wave, the transmission coefficient is defined as:

$$\tau_\infty(\theta) = |\mathcal{T}(\theta)|^2. \quad (5.6)$$

The media in the TMM basic formulation are assumed to be laterally infinite, therefore discrepancies between measured and predicted results might be significant, especially in the low frequency range, due to the presence of structural modes in real structures, and due to the scattering and diffraction effect, caused by the finite dimension of the tested panel. The so-called finite size transfer matrix method (FTMM) takes into account this diffraction effect by introducing the geometrical radiation efficiency  $\sigma_{finite}$ , described in section 3.6. The finite size transmission coefficient  $\tau_{finite}$  can thus be determined as:

$$\tau_{finite}(\theta) = \tau_\infty(\theta) \sigma_{finite}(\theta) \cos \theta. \quad (5.7)$$

For a homogeneous isotropic layer the transmission coefficient depends upon the angle of incidence of the impinging wave, but not on the propagation angle of structural waves  $\phi$ . Therefore, the finite size radiation efficiency  $\sigma_{finite}$ , given in equation (3.71) and (3.72), needs to be further integrated in the interval  $0 < \phi < \pi/2$ .

### 5.3 Orthotropic elastic medium

The transfer matrix describing wave propagation in a thin orthotropic plate  $T_{top}$  can be expressed as [136]:

$$T_{top} = \begin{bmatrix} 1 & -Z(\omega, \phi) \\ 0 & 1 \end{bmatrix}, \quad (5.8)$$

the direction-dependent mechanical impedance of the plate  $Z(\omega, \phi)$  is given by:

$$Z(\omega, \phi) = i\omega\rho h \left( 1 - \frac{D(\phi)k_t^4}{\omega^2\rho h} \right), \quad (5.9)$$

where  $D(\phi)$  is the direction-dependent bending stiffness given in equation (3.64). The global transfer matrix  $\mathbf{D}$  that describes sound propagation through thin orthotropic plates can be written as:

$$[D] = \begin{bmatrix} I_{f,top} & J_{f,top}T_{top} & [0] \\ [0] & I_{top,f} & I_{top,f} \\ [0] & [0] & [-1 \quad Z_0 \cos^{-1} \theta] \end{bmatrix}. \quad (5.10)$$

### 5.3. Orthotropic elastic medium

---

the matrices to couple the thin orthotropic plate layer with the fluid medium are given by:

$$\begin{aligned} I_{f,top} &= \begin{bmatrix} 1 & 0 \\ 0 & 1 \end{bmatrix}; & J_{f,top} &= \begin{bmatrix} -1 & 0 \\ 0 & -1 \end{bmatrix}; \\ I_{top,f} &= J_{f,top}; & J_{top,f} &= I_{f,top}. \end{aligned} \quad (5.11)$$

For a given angular frequency  $\omega$ , the complex transmission coefficient  $\mathcal{T}(\theta, \phi)$  is computed for any incidence angle  $\theta$  and any structural propagation direction  $\phi$ , by using equations (5.5), (5.4), and (5.3). The plate's finite dimension is taken into account by the geometrical radiation efficiency, function of the incidence angle  $\theta$  and the azimuthal angle  $\phi$ .

$$\tau_{finite}(\theta, \phi) = \tau_{\infty}(\theta, \phi) \sigma_{finite}(\theta, \phi) \cos \theta. \quad (5.12)$$

Considering a diffuse incident sound field, the orthotropic plate's transmission loss TL is given by:

$$TL = -10 \log \frac{\int_0^{2\pi} \int_0^{\pi/2} \tau_{finite} \sin \theta \cos \theta \, d\theta d\phi}{\int_0^{2\pi} \int_0^{\pi/2} \sin \theta \cos \theta \, d\theta d\phi}. \quad (5.13)$$

This model has been used to evaluate the sound insulation provided by an orthotropic CLT plate. The FTMM results have been validated with the experimental transmission loss of the plate CLT80\_b, measured in Empa test facility for sound insulation, according to the standard EN 10140-2 [137]. The plate was placed and fixed in a steel-concrete composite frame within the testing rooms, as described in section 4.3.

The bending stiffness along the principle directions have been evaluated from the bending wavenumbers experimentally determined as illustrated in section 4.4.1, and given in Table 4.3. To calculate the orthotropic bending stiffness, the in-plane shear modulus  $G_{xy}$  must be known. It has been approximated as a function of the elastic moduli associated with the principle direction according to equation (A.7). In Figure 5.2, the FTMM results are compared with the experimental transmission loss. The FTMM provides a good approximation of the CLT plate TL. A dip associated with the first coincidence along the stiffest vertical direction is correctly computed between the 200 Hz and 315 Hz bands, although it is more emphasised than in the experimental results. The critical frequency, as much in the numerical data as in the experimental results, is marked by a change of slope between 800-1000 Hz bands, from which the TL curve become steeper. Even though the first coincidence and the critical frequency are slightly shifted towards lower bands, the model provides a quite accurate prediction of the CLT plate transmission loss.

## 5.4. Structural bridges

---

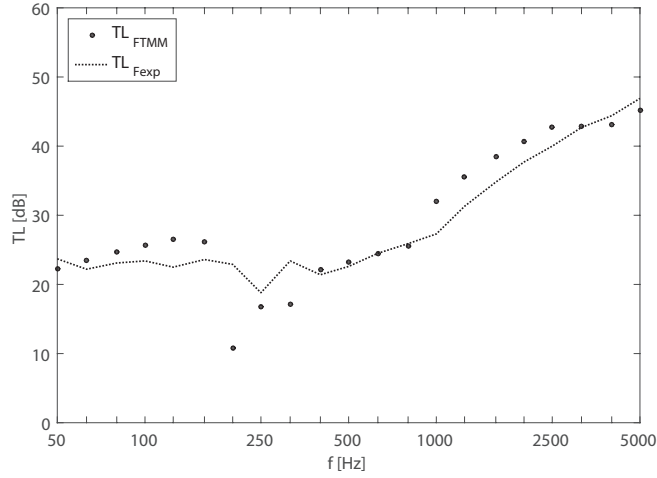


Figure 5.2: Sound transmission loss of the plate CLT80\_b, comparison between experimental data and FTMM results.

## 5.4 Structural bridges

### 5.4.1 Modelling structural connections within TMM

In section 5.2 the TMM was introduced to investigate sound transmission in multilayer structures, without mechanical bridges connecting the external surfaces. In order to take into account the structural connections in layered building elements, such as *ETICS* system, Vigran's model, based on the decoupled approach [42], was conveniently modified. The basic assumption of the decoupled approach is to consider the transmission through the different media, and the transmission through the bridges as two independent and additive paths. The total transmission loss  $TL_{tot}$  is determined by adding a correction term to the transmission coefficient  $\tau_{finite}$  obtained from the FTMM algorithm. The implementation of the global transfer matrix  $D$  to determine the transmission loss of the multilayer structure is provided in Annex D. The correction term is calculated as the ratio between the power radiated only due to the bridges action  $W_b$  over the sound power that would be radiated by the structure without mechanical connections  $W_a$ , due to the airborne excitation. For each propagation angle of the incident sound field, the total transmission coefficient  $\tau_{tot}$  is given by:

$$\tau_{tot} = \tau_{finite} \left( 1 + \frac{W_b}{W_a} \right). \quad (5.14)$$

#### 5.4. Structural bridges

---

By averaging  $\tau_{tot}$  over all the possible incidence directions, the diffuse field excitation transmission loss  $TL_{tot,d}$  is determined as:

$$TL_{tot,d} = -10 \log \frac{\int_{\theta_{min}}^{\theta_{max}} \tau_{tot}(\theta) \cos \theta \sin \theta \, d\theta}{\int_{\theta_{min}}^{\theta_{max}} \cos \theta \sin \theta \, d\theta}, \quad (5.15)$$

where the angles  $\theta_{min}$  and  $\theta_{max}$  represent the propagation limits of the incident sound wave. In the implemented algorithm the finite range of angles  $0 < \theta < \pi/2$  was used. The sound power ratio, introduced in equation (5.14) to take into account the transmission through structural bridges, can be computed as:

$$\frac{W_b}{W_a} = \frac{\sigma_b}{\sigma_a} \left\langle \left| \frac{v_{S_2,b}}{v_{S_1,F}} \right|^2 \right\rangle \left\langle \left| \frac{v_{S_1,F}}{v_{S_1}} \right|^2 \right\rangle \left\langle \left| \frac{v_{S_1}}{v_{S_2}} \right|^2 \right\rangle. \quad (5.16)$$

The first factor in the right-hand side of equation (5.16), is the ratio between the radiation efficiency of the plaster layer driven by one of the bridges  $\sigma_b$ , over the airborne radiation efficiency of the same element excited by an acoustic sound field  $\sigma_a$ . Analogously,  $v_{S_2,b}$  is the mean square vibration velocity of the surface  $S_2$  driven by the mechanical bridge, while  $v_{S_1}$  and  $v_{S_2}$  are the mean square velocities averaged over the surface ( $S_1$ ) and ( $S_2$ ) respectively, without the structural connections. The force exerted by the bridges depends on the vibration velocity of the surface they are connected with, represented in this model by  $v_{S_1,F}$ , as shown in Figure 5.6. While it is a perfectly reasonable approximation to consider an equal mean square velocity over the two opposite surfaces of a thin plate, in thick plates this is not always verified thus  $v_{S_1,F} \neq v_{S_1}$ .

The radiation efficiency  $\sigma_b$  has been defined, in Vigran's model, as the link between the sound power radiated due to the action of one bridge and the surface mean square velocity of the restricted area over which the bridge is acting. However, a different approach was followed in the proposed model, assuming that the bridge-driving action has a global influence on the velocity over the thin finishing layer surface. In fact, it has been experimentally proved that in some structures the presence of structural connections does not increase the velocity only locally, over a restricted area the bridge acts on, but it affects the entire radiating surface. In Figure 5.3 the measured velocity levels are mapped over a one-square-metre sample of a masonry wall lined with an *ETICS* system, described in the section 5.4.3. Although, the structural connections are well detectable in Figure 5.3(a), their action affects the vibration velocity over the entire surface compared to the element without mechanical connections in Figure 5.3(b). The radiation efficiency  $\sigma_b$  of the mechanically excited plate is determined according to equations (3.67). The radiation efficiency due to airborne excitation  $\sigma_a$  is otherwise computed

## 5.4. Structural bridges

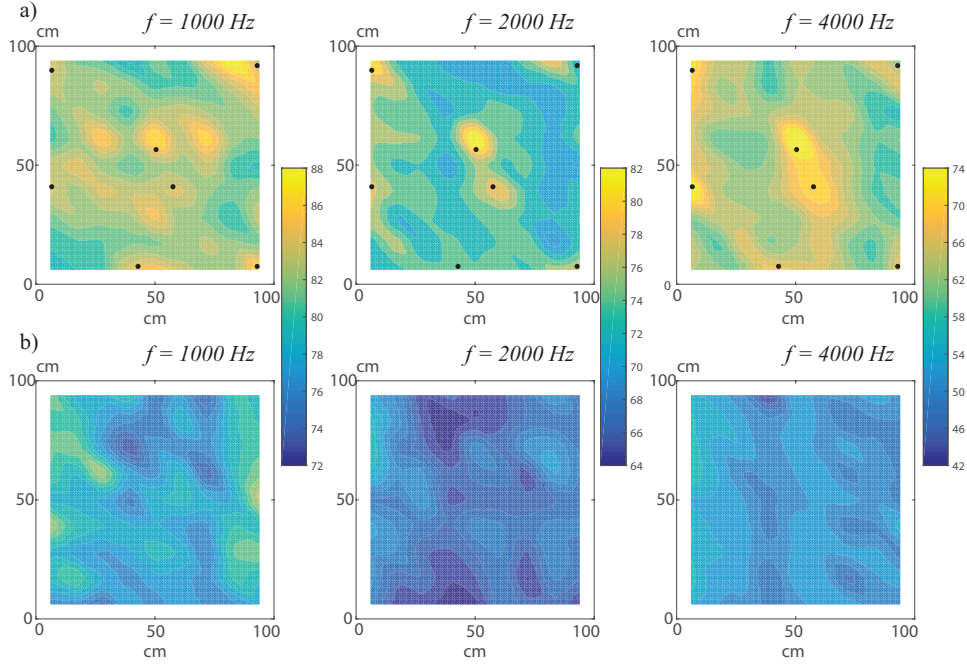


Figure 5.3: Mapping of the vibration velocity levels distribution on a 1 square metre sample of the finishing layer of the *ETICS* system. (a) Mechanical connection mounting condition:  $\bullet$  7 bridges per square metre represents the standard in real conditions. (b) Mounting condition without mechanical connections.

using equation (3.70). Both the equations are function of the ratio  $r$  of the power radiated by the resonant vibrational field to the power radiated by the vibrational near field for the point-excited panel, or to the non-resonant vibrational energy for the panel acoustically excited by a diffuse sound field, given in equation (3.68).

The mean square velocity of the radiating surface, mechanically excited by a number  $n_S$  of point-bridges per square metre, or line-connection per unit of length, can be computed according to Ref.[47] as:

$$\langle |v_{S_2,b}|^2 \rangle = n_S \frac{|F_b|^2}{\omega \eta_{S_2} m_{S_2}} \text{Re} \{ Y_{S_2} \}, \quad (5.17)$$

where  $m_{S_2} = \rho_{S_2} h_{S_2}$  is the mass per unit area of the plaster layer and  $Y_{S_2}$  is the point-drive mobility for a thin plate, given by:

$$Y_{S_i} = \frac{\omega_{c,S_i}}{8m_{S_i}c_0^2}, \quad (5.18)$$

#### 5.4. Structural bridges

---

while in case of line connections, the line drive mobility can be computed as:

$$Y_{S_i} = \frac{1 - i}{4m_{S_i}c_0} \sqrt{\frac{\omega_{c,S_i}}{\omega}}. \quad (5.19)$$

The exciting force  $F_b$  is determined as a function of the vibration velocity of the basic wall excited by the diffuse sound field as:

$$|F_b|^2 = \frac{\langle |v_{S_1,F}|^2 \rangle}{|Y_{S_1} + Y_{S_2}|^2} Q. \quad (5.20)$$

Under the thin plate theory the vibration velocity on the opposite surfaces of a plate is assumed to be equal. However, as the thin plate theory is limited in frequency range, for a massive structure such as the basic wall in the *ETCIS* system, this might not be verified in the entire frequency range. Therefore, it is more rigorous to derive the exciting force from the vibration velocity of the surface the bridges are connected with,  $v_{S_1,F}$ , namely the velocity of the inner side surface of the basic wall, on the interface with the mineral wool layer, as shown in Figure 5.6. In the literature different criteria for the thin plate theory limit can be found: for example the bending wavelength should be 6 times greater than the plate thickness. In the frequency range where the thin plate theory is not valid, the point mobility of the basic plate  $Y_{S_1}$  should be derived from the equation developed for thick plates in [41]. On the other hand when such point mobility is very small compared to the mobility  $Y_{S_2}$  of the lightweight surface of the lining system it can be approximated as  $Y_{S_1} = 0$ . From equations (5.17) and (5.20), the second factor of equation (5.16) can be expressed as:

$$\left\langle \left| \frac{v_{S_2,b}}{v_{S_1,F}} \right|^2 \right\rangle = \frac{n_S \text{Re} \{Y_{S_2}\}}{\omega \eta_{S_2} m_{S_2} |Y_{S_1} + Y_{S_2}|} Q. \quad (5.21)$$

Since within the TMM the layers are infinitely extended, the reflections of the transverse wave velocity at the edges are not included, Therefore, below half the critical frequency of the basic wall, the velocity derived from the TMM represents the forced vibrational response rather than the resonant one. For this reason, below the coincidence, a factor  $Q$ , needs to be included in the numerator of equation (5.21). As described in Ref. [47]  $Q$  can be computed as a function of the ratio between the resonant and the forced vibrational energy of the first wall as:

$$Q = \begin{cases} 1 + \frac{\pi f_{c,S_1} \sigma_{S_1}}{4f \eta_{S_1}} & \text{if } f < f_{c,S_1}; \\ 1 & \text{if } f \geq f_{c,S_1}. \end{cases} \quad (5.22)$$

However, considering massive walls the factor  $Q$  can generally be neglected, since the critical frequency usually falls within the lowest frequency bands, where the bridges' action is not significant.



The surfaces velocity ratio  $|v_{S_1}/v_{S_2}|^2$ , like in Vigran's model, is derived from the transfer matrix computed for the multilayer structure in absence of mechanical bridges. The main differences from Vigran's approach is the possibility to consider many kinds of layers, and matrices of any size. Vigran's model was developed only for thin plates and low-density fibrous/porous materials, which can be described with good approximation as an equivalent fluid by using the laws of Delany and Bazley, depending only on their air flow resistivity and thickness. In other words, only a  $[2 \times 2]$  transfer matrix is allowed and no coupling matrices are needed. However, when thick plates or poroelastic layers are modelled, matrices of different size are involved, thus coupling matrices are needed. In this case, the derivation of the ratio between surfaces' mean square velocities as provided in Vigran's model, cannot be applied, due to the increased size of the global transfer matrix. Therefore, a new procedure to numerically determine  $v_{S_1}$  and  $v_{S_2}$  is proposed. As already mentioned when equation (5.1) was introduced, the column vector  $V_{(S_1)}$  contains all the variables to completely define the acoustic field in the fluid medium adjoining the surface ( $S_1$ ): the sound pressure and the particle velocity along the  $x_3$ -direction:

$$V_{(S_1)} = [p_f(S_1), v_{f,x_3}(S_1)]. \quad (5.23)$$

Since the exciting acoustic pressure is arbitrary, it is possible to delete the first column of the transfer matrix  $\mathbf{D}$ , given in equation (5.2), obtaining a square matrix, indicated as  $\mathbf{D}_1$ . The column vector  $\bar{V}_{(S_2)}$ , containing all the variables that describe the acoustic field in the fluid domain adjoining the surface ( $S_2$ ), other than the variables that define the transmission through the different layers, can be computed by solving the algebraic system:

$$[D_1] \bar{V}_{(S_2)} = P, \quad (5.24)$$

where the vector  $P$  is the first column deleted from the matrix  $\mathbf{D}$  multiplied by  $-1$ . Due to the continuity condition, the vibration velocity over the external surfaces is equal to the particle velocity of the adjoining fluid media. Thus, for each incidence angle  $\theta$  the complex velocities  $v_{S_1,\theta}$  and  $v_{S_2,\theta}$  are determined from the vector  $\bar{V}_{(S_2)}$  as the first and last element respectively:

$$\bar{V}_{(S_2)} = \left\{ \begin{array}{c} v_{S_1,\theta} \\ \vdots \\ v_{S_1,F,\theta} \\ \vdots \\ v_{S_2,\theta} \end{array} \right\}. \quad (5.25)$$

The same procedure also allows one to obtain the velocity  $v_{S_1,F}$ , that the mechanical force  $F_b$  depends upon. Its position in the vector  $\bar{V}_{(S_2)}$  depends

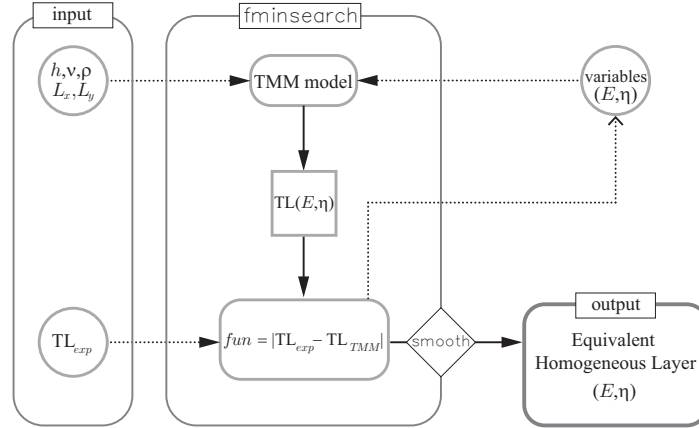


Figure 5.4: Outline of the minimisation algorithm to determine the apparent elastic properties of the equivalent homogeneous layer.

on the nature of the layers and their arrangement. In the TMM model applied to a masonry wall lined with an *ETICS* system, presented in section 5.4.3,  $v_{S_1, F}$  is the transverse velocity of basic wall, defined as a solid elastic layer and is the third element of the column vector  $\bar{V}_{(S_2)}$ . The derivation of  $v_{S_1, F}$  is computationally costless. In the case that the thin plate theory is valid over the entire frequency range  $v_{S_1, F} = v_{S_1}$  and the third ratio on the right-hand side of equation (5.16) would be equal to 1.

#### 5.4.2 Characterisation of equivalent homogeneous walls

Masonry building partitions are highly non-homogeneous structures, consisting of hollow clay or concrete bricks, and layers of mortar to join different blocks. The TMM requires the mechanical properties of each layer as input data, but the definition of parameters such as the elastic modulus,  $E$ , and the loss factor,  $\eta$ , of a brick wall is not straightforward, neither numerically, nor experimentally. Previous works tried to deal with this problem using different approaches. Maysenholder and Haberkern in [138] calculated the sound transmission through a periodically inhomogeneous infinite plate under general conditions, but this method is not easily applicable because of the required computation capacities. Another homogenization method described by Dijkmans in [139] calculates the equivalent material parameters from the measurements of the thickness resonance frequency. Jacques et al. [140] presented a homogenised vibratory model to predict the acoustic properties of hollow brick walls starting from the elastic tensor of the brick material measured using an ultrasonic technique. The presented method does not

consider the single brick, but deals with the entire wall, because the presence of mortar joints, or plaster layers, highly influences the wall behaviour.

The general numerical method to be proposed, based on the TMM framework, has been developed in order to estimate the elastic and damping apparent properties  $E$  and  $\eta$  of an equivalent homogeneous wall, from the experimental transmission loss. The massive wall, constituted by bricks jointed with mortar and the possible layers of plaster, is considered as a single equivalent homogeneous layer. A set of equivalent mechanical parameters is determined by using a minimization procedure. In this process the equivalent layer is modelled within FTMM, in which the geometric parameters, and the measured TL are the input data, whereas  $E$  and  $\eta$  represent the variables. A non-linear unconstrained optimization algorithm, based on the Matlab R2014b function `fminsearchbnd` [141] is used to estimate best values for  $E$  and  $\eta$ . It minimizes the sum square of the differences between the experimental TL and the results of the FTMM model computed for each frequency band as:

$$\Delta_{TL} = \sum_{i=1}^{n_{band}} |TL_{i,exp} - TL_{i,TMM}| \quad (5.26)$$

where  $n_{band}$  is the total number of frequency bands considered. The algorithm is outlined in Figure 5.4. The result of this process represents just one of the possible mathematical solutions, and might not have a strong physical meaning in itself. In order to preserve as much as possible physical significance of the apparent elastic modulus and the loss factor, the choice of the limits in which the algorithm works to optimize the parameters is very important. The upper and lower limits should define a realistic range of values for the investigated element. Moreover, this also increase the robustness of the algorithm, since no significant differences in the resulting elastic properties are shown when the initial guess values are changed within such a interval. Since  $\eta$  does not vary much in frequency for massive masonry walls, its mean value has been kept constant all over the frequency range. In this way the resulting curve of  $E$  is less fluctuating and tends to level off to a constant value as the frequency increases, as shown in Figure 5.5. The results obtained for each analysed frequency are finally iteratively smoothed using the Matlab moving average filter `smooth` to further reduce the numerical fluctuation. The procedure was validated with the experimental data of different masonry walls, with attached layers of fibrous or porous linings connected with adhesive mortar and screws.

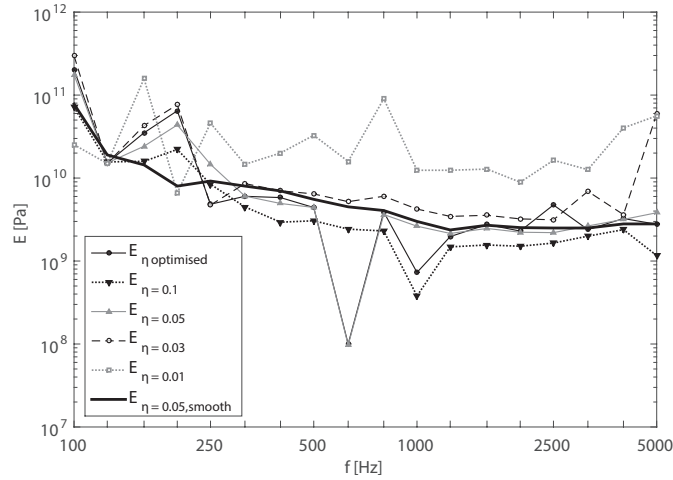


Figure 5.5: Estimated values of  $E$  associated to different values of  $\eta$  of the equivalent homogeneous layer.

### 5.4.3 Experimental validation

#### Experimental setup and measurements

Experimental measurements have been performed into the wall sound insulation test facility of the University of Ferrara in order to investigate the reliability of the model and validate the assumptions made for its derivation. The studied structure is a massive wall clad with *ETICS* system. The basic partition is a masonry wall plastered on both sides, its total thickness is 150 mm. It was modelled as an equivalent homogeneous solid layer, described by frequency dependent elastic properties, instead of elastic constants, as it is common using homogenization techniques [57]. The frequency dependent elastic modulus, reported in Table 5.1 was derived from the measured transmission loss, using the minimization algorithm described in section 5.4.2, by assuming the Poisson's ratio  $\nu = 0.33$  as typical values for this kind of partitions. Moreover, the plate loss factor was assumed to be constant  $\eta = 0.045$ , since only a small variation in frequency was found, with no significant influence on the Young's modulus resulting from the algorithm.

The basic wall was clad with mineral wool slabs 100 mm thick, finished with 5 mm of reinforced cement plaster. The high density mineral wool layer is modelled as a poroelastic medium to considering both its fluid phase and its solid frame. The five parameters related to the fluid phase, namely: airflow resistivity  $\sigma$ , open porosity  $\phi$ , tortuosity  $\alpha$ , viscous and thermal characteristic lengths  $\Lambda$  and  $\Lambda'$ , were experimentally determined using laboratory measurements combined with an inversion procedure algorithm [142]. The mechanical parameters of the solid frame were determined from

## 5.4. Structural bridges

Table 5.1: Elastic properties of the equivalent homogeneous plate used as input data for the basic wall in the FTMM model

$f$ [Hz]	$E$ [Pa]	$f$ [Hz]	$E$ [Pa]	$f$ [Hz]	$E$ [Pa]
100	$2.13 \cdot 10^{10}$	400	$6.68 \cdot 10^9$	1600	$2.58 \cdot 10^9$
125	$1.77 \cdot 10^{10}$	500	$5.54 \cdot 10^9$	2000	$2.58 \cdot 10^9$
160	$1.44 \cdot 10^{10}$	630	$4.57 \cdot 10^9$	2500	$2.58 \cdot 10^9$
200	$1.19 \cdot 10^{10}$	800	$3.74 \cdot 10^9$	3150	$2.58 \cdot 10^9$
250	$9.89 \cdot 10^9$	1000	$3.10 \cdot 10^9$	4000	$2.58 \cdot 10^9$
315	$8.15 \cdot 10^9$	1250	$2.58 \cdot 10^9$	5000	$2.58 \cdot 10^9$

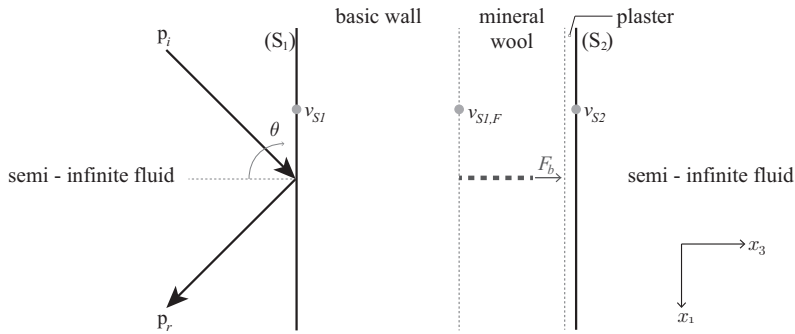


Figure 5.6: Diagram of the multilayer *ETICS* system modelled using FTMM. In order to consider the transmission contribution due to the bridges action, which is neglected by the FTMM, the mechanical force  $F_b$  is determined as a function of the velocity  $v_{S1,F}$ .

quasi-static measurements [143]. The cement plaster layer, like the basic wall, was modelled as an elastic solid medium using input values found in the literature. A diagram of the TMM model implemented to investigate this multilayer structure is shown in Figure 5.6, and the input data of each single medium are given in Table 5.2. In the first configuration the mineral wool slabs were fixed to the basic wall only using adhesive mortar, applied over approximately 40% of the surface. It was necessary to implement this configuration in order to determine experimentally the transmission loss provided by the *ETICS* system, without the additional structure-borne transmission path via the mechanical bridges. However due to static reasons, in the practical situation the adhesive fixing is not enough. It is necessary to also provide mechanical connections. In this second configuration, the structure was mounted by applying 7 mechanical bridges per square meter, in order to reproduce the in-situ conditions. A diagram of the different layers that constitute the investigated structure is given in Figure 5.7, for the two

#### 5.4. Structural bridges

---

Table 5.2: Mechanical, geometrical and acoustic descriptors used as input data in the FTMM model

	Eq. homogeneous plate	Mineral wool slabs	Reinforced plaster
$h$ [mm]	150	100	5
$\rho$ [kg/m <sup>3</sup> ]	1770	78	1500
$E$ [Pa]	freq. dependent Tab. 5.1	$5.7 \cdot 10^5$	$5 \cdot 10^9$
$\eta$ [-]	0.045	0.05	0.01
$\nu$ [-]	0.33	0.01	0.3
$\sigma$ [sPa/m <sup>2</sup> ]	-	59100	-
$\phi$ [-]	-	0.90	-
$\alpha$ [-]	-	1.00	-
$\Lambda$ [ $\mu$ m]	-	18.0	-
$\Lambda'$ [ $\mu$ m]	-	36.0	-

mounting conditions.

The sound insulation provided by the structure was determined according to the standard EN 10140-2 [137]. The influence of the mechanical connections on the transmission loss provided by the multilayer element was thus experimentally investigated by comparing the values measured with the two different mounting conditions. This comparison, given in Figure 5.8, shows clearly that they have a significant influence in the frequency range above the 630 Hz band, where the two experimental curves start to split up, and a reduction of more than 10 dB can be found. In the same Figure, the transmission loss provided by the basic wall is also plotted, to highlight the contribution of the lining. The suitability of the FTMM to predict the transmission loss of these stratified building elements was proved by comparing the numerical results with experimental data measured on the structure without mechanical connections. As shown in Figure 5.9, the FTMM gives a good approximation of the transmission loss provided by the element. The predicted curve matches reasonably well with the measured transmission loss over the entire frequency range. At low frequency the mass-spring-mass resonance is detected within the 125 Hz band. In order to investigate the reliability of the model presented here and validate the assumptions made, each term defining the correction factor, given in equation (5.16), has been validated experimentally and the global reliability of the model has been verified in terms of TL.

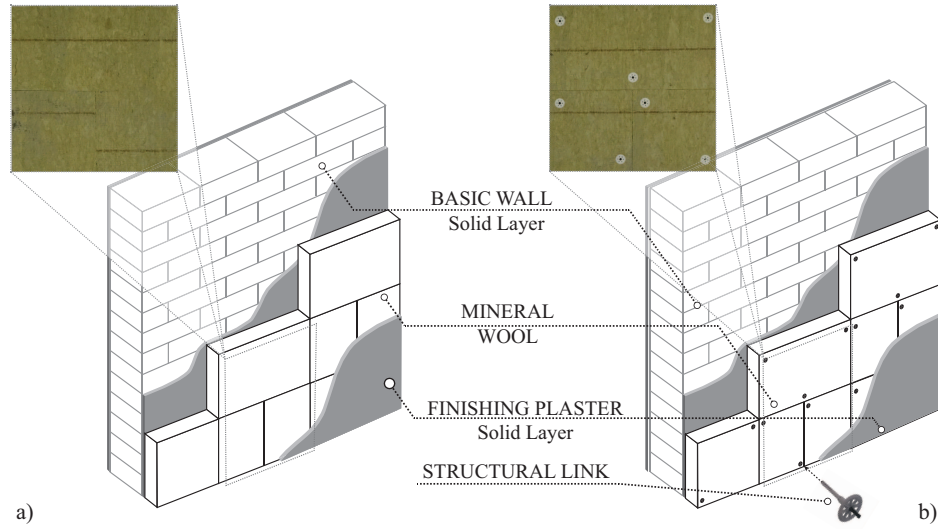


Figure 5.7: Diagram of the *ETICS* system mounted on the basic masonry wall and the definition of TMM media. (a) The mounting condition involves only adhesive mortar without mechanical connections; (b) Both mortar and mechanical fixings are used to mount the cladding system on the basic wall. For each condition, a picture of the system before the finishing layer was applied is shown.

### Validation of FTMM model for structural connections

In order to determine experimentally the velocity ratio in absence of structural bridges, the surface vibration velocity was measured, both on the source  $v_{S_1,exp}$  and the receiving side  $v_{S_2,exp}$ , using PCB accelerometers with a sufficiently low mass ( $m \leq 10$  g), to avoid any possible influence on the dynamic response of the finishing layer. The vibration velocity over the basic wall surface was averaged over a random distribution of accelerometer positions according to the standard ISO 10848-1 [112]. The velocity on the reinforced plaster surface, which in the experimental configuration was on the receiving side, was averaged over a grid of accelerometer positions, with an equal spacing of 100 mm. This procedure was extremely time consuming but allowed the investigation of the regions over which the structural bridges were acting. In Figure 5.10, the ratio between the average velocity on the surfaces ( $S_1$ ) and ( $S_2$ ), evaluated numerically from the TMM, is compared with the data measured on the structure without connections. While a very good agreement is found in the low frequency range, the model seems to overestimate this ratio at higher frequencies. However, since the same model provided accurate results in terms of transmission loss, as shown in Figure 5.9, the discrepancies might be due to experimental uncertainties. In

## 5.4. Structural bridges

---

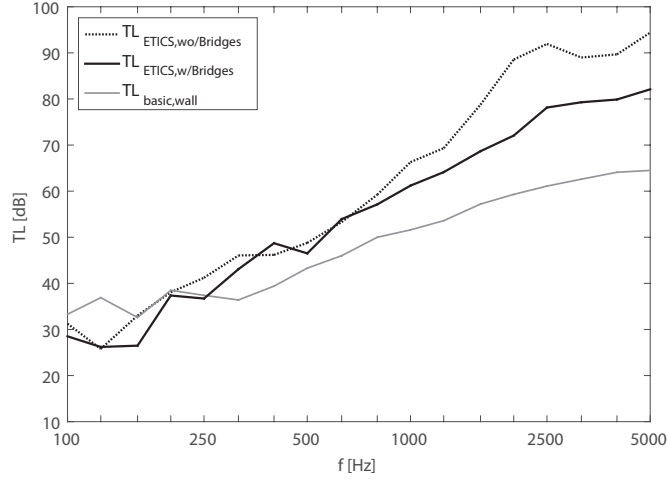


Figure 5.8: Transmission loss experimentally evaluated on the basic wall and on the multilayer structure, with and without the mechanical fixing.

all probability the number of points used to measure the vibration velocity over the surface on the exciting side ( $S_1$ ), chosen in order to fulfil the distance requirements of the standard EN 10848-1, was not enough to obtain an accurate spatial sampling. Therefore, the mean velocity  $v_{S_1}$  might represent an underestimation of the mean velocity of the surface ( $S_1$ ), as it has been discussed for CLT plates in section 4.3.

Due to practical reasons it was not possible to measure the mean square velocity on the thin finishing layer driven only by the bridges actions. This is because the reinforced plaster layer cannot be mounted detached from the mineral wool. Under the decoupled approach the total radiated power is assumed to be the sum of the airborne radiated sound power and the sound power radiated due to the bridges' action. This relationship can be expressed in terms of radiation efficiencies and mean square velocity as:

$$\left\langle \left| \frac{v_{2,tot}}{v_{S_1}} \right|^2 \right\rangle \sigma_{tot} = \left\langle \left| \frac{v_{S_2,b}}{v_{S_1}} \right|^2 \right\rangle \sigma_b + \left\langle \left| \frac{v_{S_2}}{v_{S_1}} \right|^2 \right\rangle \sigma_a \quad (5.27)$$

In order to validate the approach used to calculate the surface velocities ratio of the structure with mechanical connections, the left-hand side of equation (5.27) was experimentally determined with the sum on the right-hand side of the equation numerically computed. This comparison, given in Figure 5.11, shows a rather good agreement between the experimental total velocity ratio and the numerical results, which means that the model well approximates the trend of the vibration velocity of the finishing layer driven by the structural bridges.



## 5.4. Structural bridges

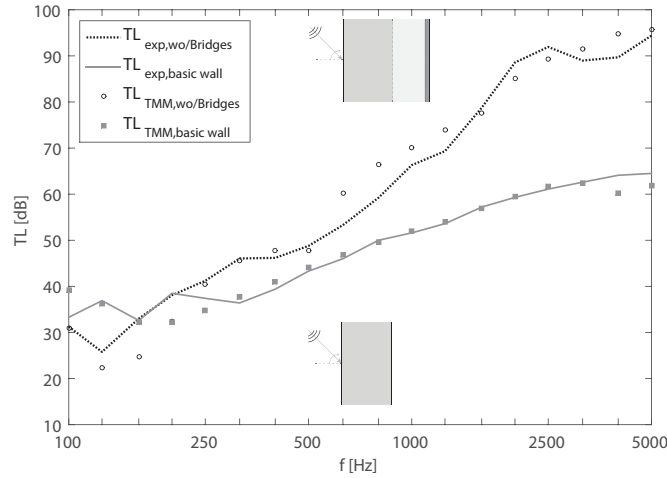


Figure 5.9: Transmission loss of the *ETICS* system without structural connection. Comparison between the FTMM results and experimental data.

The same practical issue determined also the impossibility to experimentally evaluate the ratio of the radiation efficiencies. Nevertheless, some considerations on the radiated sound power can be made in order to validate the hypothesis of the model. The sound power radiated by the finishing thin plate, in both the mounting conditions, was determined through sound intensity measurements, performed according to the standard ISO 9614-3 [144]. The lateral walls and the floor were shielded with absorbing material, to reduce the interference given by the reverberant sound field. In Figure 5.12, the sound power levels radiated from the structure with  $W_{tot,bridges}$  and without mechanical connections  $W_{wo/bridges}$  are compared. Below the 630 Hz band, no significant differences are shown, while the two curves progressively split apart as the frequency increases. At low frequencies transmission via the mineral wool frame and the air that fills the voids is dominant. However, as the frequency increase, sound transmission due to the bridges' driving action becomes more and more significant. This is particularly in line with the assumption made in the model, since at low frequency there is no difference between the layered element with or without bridges. However, at higher frequencies, approaching the critical condition of the plaster layer, the resonant and the near field radiation, due to the mechanical excitation, becomes the dominant component.

The global reliability of the model was finally verified by comparing the transmission loss obtained from the TMM with the experimental results in Figure 5.13. The numerical results provided by the proposed model are in rather good agreement with the experimental data and the sound insulation reduction in the high frequency region is well approximated. In the mid-

## 5.4. Structural bridges

---

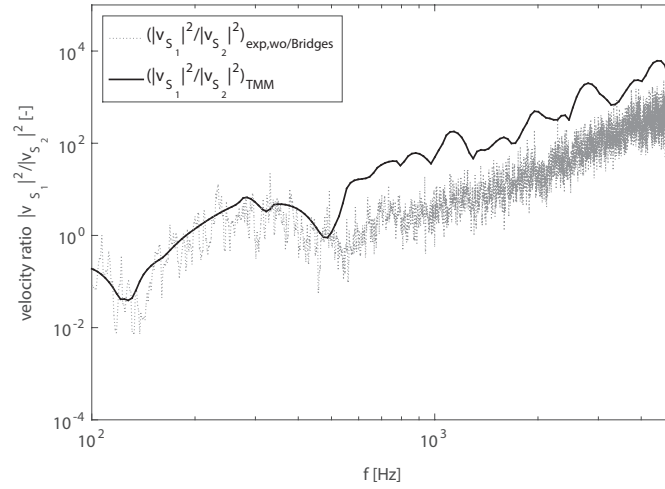


Figure 5.10: Ratio between the mean square velocities on the external surfaces of the multilayer structure. The experimental results, measured on the sample without mechanical bridges, are compared with numerical data obtained from the TMM

frequency range a slightly higher transmission loss is computed with the FTMM, while above 2000 Hz the reduction caused by the bridges' action is overestimated, due to the assumption of infinite stiff structural connections, as already proved in [145]. However, for this kind of structures the effect of the assumption of bridges with infinite stiffness seems to be less significant, than in lightweight frame-based partitions. In the same Figure the transmission loss obtained from Vigran's formulation is plotted as a further proof that the different assumptions made in this model are correct and necessary to consider double wall system consisting of two plates with incomparable thickness and mass, or when the cavity is filled with high density fibrous material that cannot be modelled as an equivalent fluid. Vigran's model proved to work very well with double leaf lightweight structures, but it clearly fails in the prediction of the reduction of the *ETICS* transmission loss, caused by the presence of point-bridges, providing an underestimated reduction.

The model was also successfully applied to other massive partitions. The FTMM results of a clay brick wall plastered on one side, with a total surface mass of  $150.5 \text{ kgm}^{-2}$ , and lined with an *ETICS* system involving a double density mineral wool  $150/95 \text{ kgm}^{-3}$ , are compared with the experimental results in Figure 5.14, showing a remarkable agreement.

The more general applicability of this model was further verified by modelling lightweight structures presented in some of the previously cited papers. The model has been applied to predict the TL of the double wall system presented by Legault and Atalla in Ref. [32]. It consists of two

## 5.4. Structural bridges

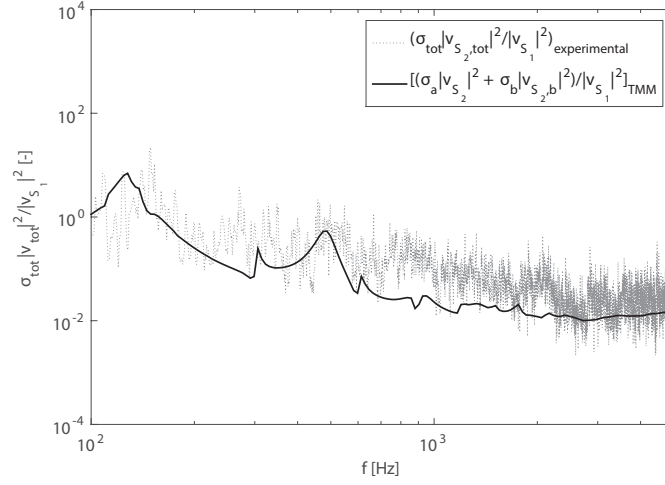


Figure 5.11: Comparison between the total vibration velocity measured on the plaster layer surface, on the structure with mechanical connections multiplied by the radiation efficiency experimentally evaluated, and numerical surface velocity ratios with and without bridges multiplied respectively by the airborne and point-driven radiation efficiency.

aluminium plates separated by a 50.8 mm thick cavity filled with fibrous material. The two panels are connected by line aluminium junctions that in the FTMM model are assumed to be massless, and infinite stiff. In Figure 5.15 the FTMM results both for the uncoupled, and coupled structures, are compared with the experimental data extrapolated from Figures 3, and 4 of Legault’s paper. The FTMM model allows for a rather good approximation of the structure’s TL, either considering only the fluid-borne transmission, or the coupled system. The results for the coupled structures are in very good agreement with the curve obtained by Legault et al. implementing Davy’s model for massless structural connections, which is presented in Figure 4 of their paper.

Finally the possibility to extend the FTMM model to allow for structural connections with a finite stiffness was investigated. Following Davy’s approach [47] it is possible to introduce the bridge’s compliance. The force exerted on the radiating panel given in equation (5.20) for infinite stiff connections, can be reformulated for elastic connections as:

$$|F_b|^2 = \frac{\langle |v_{S_1, F}|^2 \rangle}{|i\omega C + Y_{S_1} + Y_{S_2}|^2} Q \quad (5.28)$$

To validate this approach, a double-leaf gypsum walls with steel studs, described in Ref. [146] and numerically investigated by Vigran in [42], has

## 5.5. Conclusion

---

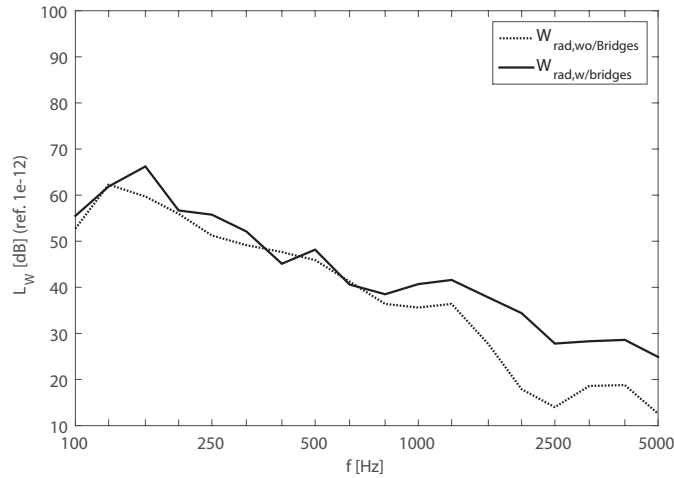


Figure 5.12: Sound power levels radiated by the building element, experimentally determined from sound intensity measurements.

been modelled. The mechanical compliance has been determined by inverting the studs' stiffness, experimentally measured by Poblet-Puig et al. [147] and provided in Vigran's papers. The FTMM transmission loss, is given in Figure 5.16 for the structure with and without mechanical connections. A good agreement is found between FTMM and experimental data. Moreover the results related to infinitely stiff bridges are given to highlight the influence of this simplifying assumption on the transmission loss of lightweight structures. The FTMM results are consistent with the data presented by Vigran in Figure 6 of Ref. [42].

## 5.5 Conclusion

In this Chapter the transfer matrix method has been applied to complex elements commonly used as building partition. The complexity is represented either by their sub-structure, which provides a direction-dependent stiffness, like CLT plates, or by the presence of different layered media. The FTMM, which also considers a correction term to take the finite dimension of the structures into account, has been firstly applied to model predict the transmission loss of a CLT plate. The panel has been described as a thin orthotropic plate, characterised by the orthotropic bending stiffness computed from the structural wavenumbers associated with the principal directions, approximating the in plane shear modulus as a function of the elastic moduli. The transmission loss obtained from FTMM model has been compared with the experimental laboratory results. The model allows to accurately predict the sound transmission loss provided by the CLT panel.

## 5.5. Conclusion

---

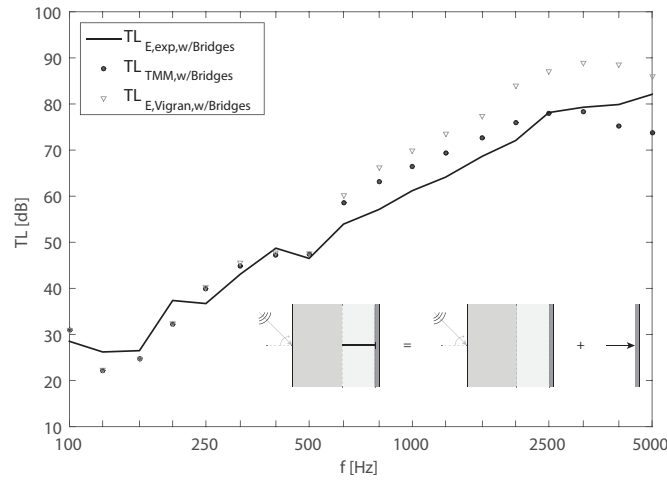


Figure 5.13: Transmission loss of the *ETICS* system with structural connection. Comparison between the FTMM results and experimental data.

A prediction model to investigate the transmission loss provided by a cladding system for building partitions has been developed. The basic building wall and the cladding system can be seen as a multilayer structure; therefore, the TMM is a particularly useful tool to describe sound propagation through the different media. Due to static reasons it is necessary to attach the lining slabs using mechanical connections other than an adhesive layer. Although many prediction models can be found in the literature to model structural links in stratified elements or double panel systems, a more general model, based on the decoupled approach, has been proposed in order to consider also thick plates and high-density porous and fibrous materials, taking inspiration from an existing formulation developed within the TMM framework. The structure-borne sound transmission through mechanical fixings is considered by means of a correction factor added to the transmission coefficient obtained from the TMM model. All the parameters necessary to determine the correction term have been accurately described, defining all the assumptions made in their derivation. The validation of each parameter and the global reliability of the model has been investigated with experimental data, measured on a masonry clay brick wall, lined with high-density mineral wool, and a reinforced plaster finishing. At first the influence of mechanical connections on sound insulation provided by the element was investigated. Due to the structure-borne transmission, a clear reduction of sound insulation is shown above the 630 Hz frequency band. Comparing the transmission loss, measured on the tested element without structural links, with the numerical results obtained from TMM a very good agreement has been found, proving that this is a suitable tool for such elements. The validation shows that

## 5.5. Conclusion

---

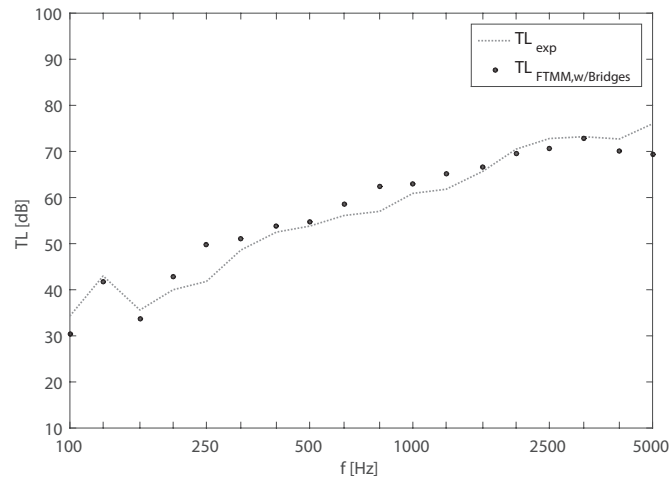


Figure 5.14: Transmission loss of a clay brick wall lined with an *ETICS* system using a double density mineral wall. Comparison between the FTMM results and experimental data.

all the assumptions of the model are quite reasonable and the numerical parameters approximate very well the experimental data. The proposed method considers the ratio between the radiation efficiency of the plate, on the receiving side, mechanically and acoustically excited. The power radiated due to the structural connection is thus computed by taking into account the mean square velocity averaged over the entire plate surface, instead of considering only a restricted area over which the mechanical force is exerted, since the bridges' action influences the dynamic response of the whole surface, as was experimentally proven. The numerical evaluation of the surface velocities ratios matches very well the experimental results both for the case with sound bridges and in absence of structural links. Comparing the radiated sound power measured in the two different mounting configurations, a similar radiation behaviour has been found at low frequencies, governed by transmission via the mineral wool. However, at high frequencies the radiation due to the bridges' action becomes more and more significant. A very good agreement between the FTMM results and the experimental transmission loss has been found. The model can accurately predict the frequency region where the sound insulation of the building element is reduced due to the bridges' actions. The applicability of the model to lightweight structures was further investigated, predicting with a good accuracy the TL of double-leaf frame-based systems with aluminium plates, and gypsum boards. Finally, since the assumption of infinite stiff connections leads to an underestimation of the TL, the possibility to consider elastic structural bridges was introduced into the model and successfully verified.

## 5.5. Conclusion

---

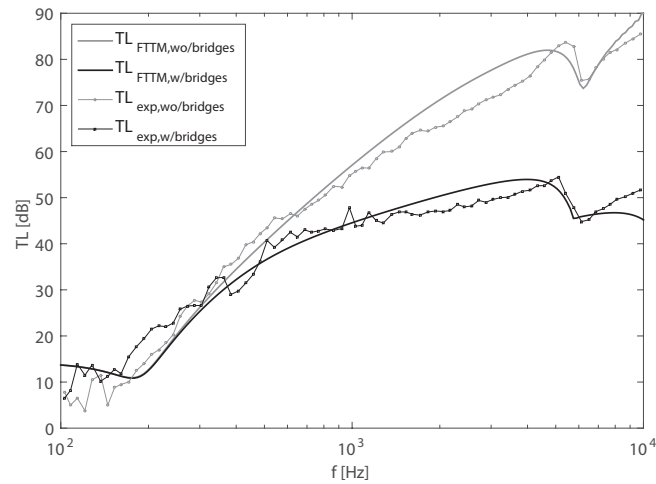


Figure 5.15: Transmission loss of a double leaf aluminium plate with structural line connections. Comparison with Figure 3, and 4 of Ref. [32].

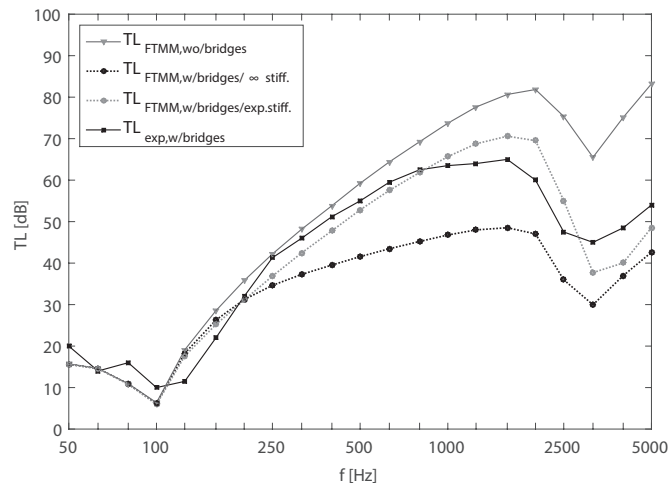


Figure 5.16: Transmission loss of a double leaf gypsum board with metal studs. Comparison with Figure 6 of Ref. [42].

# Chapter 6

## Conclusion

### 6.1 Overview

In this dissertation, the issue of predicting sound radiation and sound transmission in building structures, which cannot be treated as homogeneous isotropic elements, has been addressed. In order to investigate the radiation efficiency of orthotropic plates, excited either by a mechanical point force, or by an incident sound field, an analytic model has been developed based on Hamilton's variational principle, extending an existing model derived for isotropic plates. The plate dynamic response and the radiated sound power are computed for each single mode, either resonant or non-resonant, considering both airborne excitation, and mechanical point forces. The average radiation efficiency is evaluated from the total radiated power and the surface mean square vibration velocity. This approach allows one to take into account the influence of fluid loading on the plate's dynamic response. The model was validated by comparing the results with the experimental radiation efficiency evaluated for a three-ply CLT plate, which, due to the layered structure, exhibits an orthotropic behaviour. The comparison highlighted a rather good agreement between numerical and experimental data, especially for the plate mechanically excited. Although the analytic model provides reliable results, detecting with a satisfying accuracy both the critical frequency and the first coincidence associated with the stiffest direction, the predicted radiation efficiency is slightly overestimated below the critical frequency. The discrepancy is mostly associated with the assumption of simply-supported boundary conditions, which do not truly represent the experimental fixing condition. In fact, it has been found that, along the edges, the out of plane motion of the plate was not completely prevented by the experimental mounting condition. Many studies investigated the influence of boundary conditions on sound radiation, finding that the radiation efficiency increases due to an increase of the constraint degree at the edges. This effect seems to be more accentuated when a diffuse incident sound field is considered as the external exciting



force. The influence of fluid loading on the plate response has been examined, which is usually considered negligible when the fluid inertia is much lower than the inertia of the structure. No relevant influence has been found in the radiation efficiency of a CLT plate by neglecting the fluid loading and approximating the radiation impedance with the self-radiation resistance, except small differences in the very low frequencies. Moreover, when the fluid loading is neglected, the computational cost of the analytical model is drastically reduced to 1.5–2% of the time that would be necessary to compute the radiation impedance matrix. The results obtained from the approximated analytical model have been compared with the average radiation efficiency computed from a modal summation approach, since this model had already been applied to orthotropic elements, providing a satisfying accuracy. The two approaches gave consistent results and an almost identical computational performance. However, the analytical approach, unlike the modal summation approach, allows to also consider either external sources of different nature and specific positions for a mechanical excitation.

A modal-average model has been proposed to compute the radiation efficiency when the orthotropic plate vibration response is characterised by high modal density within the investigated frequency range. Each mode is considered only at its resonance, therefore this model can be applied only to mechanically excited structures by a broadband force, since in this case the multi-mode response is generally governed by the resonant vibrational field. The model has been implemented in such a way that, by means of an elliptic interpolation, the bending wavenumbers along the two principle directions represent the plate's stiffness characteristics required as input. Once again the results have been validated by comparison with the experimental radiation efficiency of a CLT plate. The model provide reliable results, even if the average radiation efficiency is not very detailed in the low frequency range, where the plate's vibrational field is governed by modal response. However, it is still a helpful tool that provides an accurate trend of the radiation efficiency of an orthotropic plate, which requires only 2% the computational time necessary to run the analytical model by neglecting the fluid loading.

The stiffness properties necessary as input data in the models are obtained through an experimental characterisation based on flexural wave analysis. The phase difference method has been used to determine the bending wave velocity propagating in the CLT plate at low frequencies, while at high frequencies the time of flight difference was found to be more accurate. The values obtained at each tested frequency were interpolated, in the entire range of interest, by means of a non-linear fitting algorithm, based on Mindlin's dispersion relation. The bending stiffness along the principle directions of the equivalent CLT thin plate has been determined from the experimental bending wavenumbers, by using Kirchhoff's dispersion relation. The equivalent thin plate exhibits a frequency dependent apparent bending stiffness, which compensates the fact that rotational inertia, and the shear deformation

effects are neglected in thin plate theory. The orthotropic bending stiffness, approximated by an elliptic interpolation, is in good agreement with the experimental data measured for different propagation angles.

The issues associated with the experimental evaluation of the radiation efficiency have been investigated on three different three-ply CLT plates. Two distinct approaches to determine radiated sound power, based on different assumptions and with different limitations, have been compared. Although some small discrepancies between the results have been found, these approaches provide consistent results. The radiation efficiency is also influenced by the number of measurement positions, and their distribution, over which the mean square velocity is spatially averaged. Significant differences have been found when the surface vibration velocity is averaged over a random distribution of measurements positions. A parametric analysis, undertaken on the same set of measured data, shown that for a surface of approximately  $12.2 \text{ m}^2$  at least 100 measurement positions are necessary to obtain a good spatial sampling. Moreover it has been found that a random distribution of transducers, fulfilling the distances requirements given in the standard EN 10848-1, provides an underestimated mean square velocity compared to spectrum obtained by the complete data set. In order to experimentally show how sound radiation is highly influenced by the type of excitation, the plates were excited both by a mechanical force, using a shaker rigidly connected to the wood panel, and by a diffuse sound field, generated by a dodecahedron sound source. When the plate is excited by a mechanical force its response, below the critical frequency, is mainly governed by resonant modes and sound radiation mostly depends on the plate's stiffness. The experimental radiation efficiency, evaluated for the different CLT plates, shown how the ratio of the outer layers thickness to the thickness of the inner core plays an important role on the stiffness properties of this kind of structures. However, below the critical frequency, when the plates are excited by a diffuse sound field, their response is governed by the forced non-resonant field, and the three structures exhibit a similar radiation behaviour, although they have very different stiffness properties. Above the critical condition, both with mechanical, and airborne excitation, the radiation efficiency tends to unity, and it is not possible to distinguish between resonant and forced field.

Orthotropic structures excited by an incident sound field have also been analysed in terms of sound transmission. The transmission loss of orthotropic elements, such as CLT plates, has been predicted using the TMM, which is one of the most efficient tools to model sound propagation through media of different nature. To have a better agreement with experimental results, a geometric radiation efficiency needs to be introduced in the TMM model to account for the finite dimension of the element. The transmission loss of a CLT panel, described as a thin orthotropic plate, was accurately predicted using FTMM. The direction-dependent bending stiffness was computed approximating the in plane shear modulus as a function of the elastic moduli

along the principal directions. In order to take into account the structure-borne transmission through the rigid connections of lined walls, or double leaf panels, a model based on the FTMM framework has been developed. Differently from other models, developed by several authors specifically for thin plates, a more general approach has been proposed. This model allows to consider either thin and thick plates, and poroelastic materials, by taking into account both the transmission through the fluid that fills the pores, and the transmission through the solid frame. The model has been validated with the experimental transmission loss, measured on an *ETICS* system, constituted by a masonry clay brick wall, lined with slabs of high-density mineral wool, finished with a layer of reinforced plaster. A very good agreement between the FTMM results and the experimental transmission loss has been found. The model can accurately predict the frequency region where the sound insulation of the building element is reduced due to the bridges' actions. To investigate whether the model might be applied also to lightweight frame-based structures, a double leaf aluminium plate, and gypsum board double-wall system, have been modelled with good accuracy. Finally, Davy's approach to take into account a finite value of the stiffness of structural bridges was introduced into the model, and successfully verified.

## 6.2 Future developments

The radiation models have been developed under the simplifying assumption of simply supported boundary conditions. This allows for an analytical, or approximated, solution of the governing equations, and thus a faster computation. Many studies have been undertaken, proving how different boundaries influence the radiation behaviour. However in the literature, both polynomial and trigonometric trial functions can be found, in order to consider different boundary conditions. Therefore, it might be useful to investigate the possibility to derive the analytical model for a fully clamped orthotropic plate, to thoroughly investigate the boundary influence on the dynamics of such structures and to provide a more versatile prediction tool.

One of the limits of the modal-average radiation efficiency is represented by the fact that only the contribution of resonant modes is taken into account. However for homogeneous isotropic plates, a correction factor, based on the ratio between resonant and force response, can be applied to overcome this limitation. Extending this approach also to orthotropic structures would provide more accurate results, and would give the chance to apply this model also to airborne excitation.

Sound transmission through orthotropic panels has been modelled by means of the FTMM. The problem has been simplified assuming the structure as an equivalent thin orthotropic plate, described by frequency dependent elastic properties. To provide a handy tool for the design and the acoustic

optimisation of CLT panels, an alternative approach to apply the TMM should be investigated. Each single layer of a CLT structure could be modelled as a solid homogeneous medium, described by the elastic dynamic properties of the lumber beams. However, the determination of the elastic properties is a delicate aspect that presents some difficulties, since each layer, made out of beams, exhibits an orthotropic behaviour in itself. Hence for a complete characterisation of each single layer the wood elastic properties might not be enough, but it would be necessary to implement additional simulations, evaluating its orthotropic behaviour.

From the experimental point of view, the influence of the measurement points spacing, either on a grid or on a random distribution will be further investigated. From the complex vibration velocity measured on a grid distribution it is possible to compute the radiated sound power, by means of hybrid methods, such as DCM. A great advantage of these approaches is their applicability at low frequencies. However, to be extended up to high frequencies a small grid spacing it is required, and the time necessary for the experimental test might increase significantly. The intention is to examine in the near future the possibility to implement hybrid methods combined with interpolating functions in order to reduce the time required to perform experimental measurements. Moreover, the wave analysis to investigate the stiffness properties of a structures might be extended in order to evaluate both the real and imaginary part of the complex flexural velocity, obtaining information about the structural damping.

# Appendix A

## Stiffness Matrix Coefficients

In this Annex a simpler formulation of the integral equation derived in Chapter 3, to compute the stiffness matrix coefficients of a thin orthotropic plate, is provide for the case of simply-supported boundary conditions. Using the dimensionless coordinates:

$$\begin{cases} u = \frac{x}{L_x} \\ v = \frac{y}{L_y} \end{cases}, \quad (\text{A.1})$$

The mode shape functions for simply-supported boundaries are given in the new coordinate system as:

$$\begin{cases} \phi_{mn}(u, v) = \sin(m\pi u) \sin(n\pi v); \\ \phi_{pq}(u, v) = \sin(p\pi u) \sin(q\pi v). \end{cases} \quad (\text{A.2})$$

The chain rule for a second order derivative can be applied obtaining:

$$\begin{cases} \frac{\partial^2}{\partial x^2} \phi_{ij}(x, y) = \frac{\partial^2}{\partial u^2} \phi_{ij}(u, v) \left( \frac{du}{dx} \right)^2; \\ \frac{\partial^2}{\partial y^2} \phi_{ij}(x, y) = \frac{\partial^2}{\partial v^2} \phi_{ij}(u, v) \left( \frac{dv}{dy} \right)^2; \\ \frac{\partial^2}{\partial x \partial y} \phi_{ij}(x, y) = \frac{\partial^2}{\partial u \partial v} \phi_{ij}(u, v) \frac{du}{dx} \frac{dv}{dy}. \end{cases} \quad (\text{A.3})$$

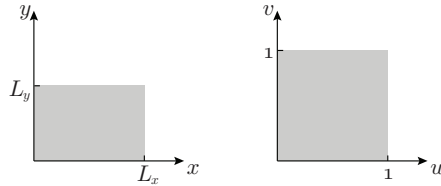


Figure A.1: Coordinates transform given in equation (A.1)

---

Moreover, due to this change of variable within the double integral, the new integrands  $du$  and  $dv$  have to be multiplied by the absolute value of the Jacobian  $L_x L_y$ . Equation (3.32) can thus be rewritten in terms of the new spatial coordinates  $u$  and  $v$  as:

$$\begin{aligned}
K_{mnpq} = & L_x L_y \int_0^1 \int_0^1 \left[ D_x \left( \frac{1}{L_x^2} \right)^2 \frac{\partial^2}{\partial u^2} \phi_{mn}(u, v) \frac{\partial^2}{\partial u^2} \phi_{pq}(u, v) \right. \\
& + D_y \left( \frac{1}{L_y^2} \right)^2 \frac{\partial^2}{\partial v^2} \phi_{mn}(u, v) \frac{\partial^2}{\partial v^2} \phi_{pq}(u, v) \\
& + \nu_{yx} D_x \left( \frac{1}{L_y L_x} \right)^2 \frac{\partial^2}{\partial u^2} \phi_{mn}(u, v) \frac{\partial^2}{\partial v^2} \phi_{pq}(u, v) \\
& + \nu_{xy} D_y \left( \frac{1}{L_y L_x} \right)^2 \frac{\partial^2}{\partial v^2} \phi_{mn}(u, v) \frac{\partial^2}{\partial u^2} \phi_{pq}(u, v) \\
& \left. + 4G_{xy} \frac{h^3}{12} \left( \frac{1}{L_y L_x} \right)^2 \frac{\partial^2}{\partial u \partial v} \phi_{mn}(u, v) \frac{\partial^2}{\partial u \partial v} \phi_{pq}(u, v) \right] dv du
\end{aligned} \quad (A.4)$$

Due to the orthogonal property of the mode shape functions, discussed in Chapter 2, equation (A.4) can be rewritten as:

- if  $m = p$  and  $n = q$

$$K_{mnmn} = \frac{L_x L_y}{4} \left[ D_x \frac{m^4 \pi^4}{L_x^4} + D_y \frac{n^4 \pi^4}{L_y^4} + 2B \frac{m^2 n^2 \pi^4}{L_x^2 L_y^2} \right]; \quad (A.5)$$

- if  $m \neq p$  or  $n \neq q$

$$K_{mnpq} = 0. \quad (A.6)$$

The stiffness matrix  $K_{mnpq}$  of a simply-supported orthotropic plate is diagonal and can be computed by means of a simple algebraic equation, reducing the computational time significantly. The bending stiffness along each principle direction is obtained, according to equation (3.13), from the experimental wavenumbers given in Table 4.3. The in-plane shear modulus  $G_{xy}$  of the orthotropic plate, necessary to compute the effective torsional stiffness  $B$ , given in equation (3.14), has been approximated as a function of the elastic moduli associated with the principal directions [64] as:

$$G_{xy} = \frac{\sqrt{E_x E_y}}{2(1 + \sqrt{\nu_{xy} \nu_{yx}})}. \quad (A.7)$$

The value of the elastic properties  $\nu_{xy}$  and  $\nu_{yx}$  has been determined from equation (3.15) assuming the plate Poisson's ratio  $\nu = \sqrt{\nu_{xy} \nu_{yx}} = 0.3$  as typical for wood materials.

## Appendix B

# Radiation Impedance Matrix Coefficients

The four-fold integral equation to compute the radiation impedance, given in equation (3.34), is approximated to a two-fold integral following the approach proposed by Sandman [13] and Nellisse [16]. A first coordinate transform is applied:

$$\begin{cases} \alpha = \frac{x}{L_x} \\ \beta = \frac{y}{L_y} \end{cases}; \quad \begin{cases} \bar{\alpha} = \frac{x_0}{L_x} \\ \bar{\beta} = \frac{y_0}{L_y} \end{cases}; \quad r = \frac{L_x}{L_y}. \quad (\text{B.1})$$

By mixing the modes, one can express the plate's radiation impedance as:

$$Z_{mnpq} = i\omega\rho_0 S^2 \int_0^1 \int_0^1 \int_0^1 \int_0^1 [\psi_{mp}(\alpha, \bar{\alpha}) G(\alpha, \beta, 0, \bar{\alpha}, \bar{\beta}, 0) \psi_{nq}(\beta, \bar{\beta})] d\bar{\alpha} d\bar{\beta} d\alpha d\beta. \quad (\text{B.2})$$

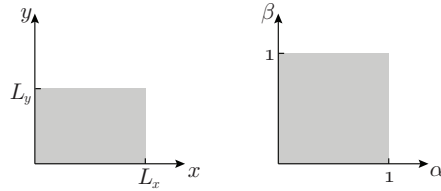


Figure B.1: Coordinates transform given in equation (B.1)

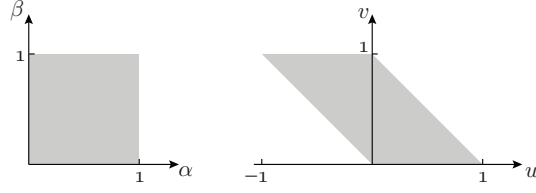


Figure B.2: Coordinates transform given in equation (B.3)

A further change of variable is needed:

$$\begin{cases} u = \alpha - \bar{\alpha}; \\ v = \bar{\alpha}; \end{cases} \quad \begin{cases} \bar{u} = \beta - \bar{\beta}; \\ \bar{v} = \bar{\beta}. \end{cases} \quad (\text{B.3})$$

Considering the symmetry of the mode shape functions, the radiation impedance can be expressed in the new coordinate system as:

$$Z_{mnpq} = 4i\omega\rho_0 S^2 \int_0^1 \int_0^1 \Phi_{mp}(u) G(u, 0, \bar{u}, 0) \Phi_{nq}(\bar{u}) d\bar{u}du, \quad (\text{B.4})$$

where:

$$\begin{aligned} \Phi_{mp}(u) &= \int_0^{1-u} \sin(m\pi(u+v)) \sin(p\pi v) dv; \\ \Phi_{nq}(\bar{u}) &= \int_0^{1-\bar{u}} \sin(n\pi(\bar{u}+\bar{v})) \sin(q\pi\bar{v}) d\bar{v}; \end{aligned} \quad (\text{B.5})$$

$$G(u, 0, \bar{u}, 0) = \frac{\exp\left(-ik_0 L_x \sqrt{u^2 - r^{-2}(\bar{u})^2}\right)}{2\pi L_x \sqrt{u^2 - r^{-2}(\bar{u})^2}}.$$

If  $m \neq p$  and  $n \neq q$  the integral functions  $\Phi_{mp}(u)$  and  $\Phi_{nq}(\bar{u})$  are given by:

$$\begin{aligned} \Phi_{mp}(u) &= \frac{\sin(\pi(m-p+pu))}{2\pi(m-p)} - \frac{\sin(\pi mu)}{2\pi(m-p)} \\ &\quad - \frac{\sin(\pi(m+p-pu))}{2\pi(m+p)} + \frac{\sin(\pi mu)}{2\pi(m+p)}; \\ \Phi_{nq}(\bar{u}) &= \frac{\sin(\pi(n-q+q\bar{u}))}{2\pi(n-q)} - \frac{\sin(\pi n\bar{u})}{2\pi(n-q)} \\ &\quad - \frac{\sin(\pi(n+q-q\bar{u}))}{2\pi(n+q)} + \frac{\sin(\pi n\bar{u})}{2\pi(n+q)}; \end{aligned} \quad (\text{B.6})$$



---

while if  $m = p$  and  $n = q$ , the integral functions are given by:

$$\begin{aligned}\Phi_{mp}(u) &= \frac{\sin(\pi m(u-2))}{4\pi m} + \frac{\sin(\pi m u)}{4\pi m} \\ &\quad + \cos(\pi m u) \left( \frac{1-u}{2} \right); \\ \Phi_{nq}(\bar{u}) &= \frac{\sin(\pi n(\bar{u}-2))}{4\pi n} + \frac{\sin(\pi n \bar{u})}{4\pi n} \\ &\quad + \cos(\pi n \bar{u}) \left( \frac{1-\bar{u}}{2} \right),\end{aligned}\tag{B.7}$$

Applying Prosthapheresis' sum to product formulas, these equations can be rewritten as:

if  $m \neq p$  and  $n \neq q$ :

$$\begin{aligned}\Phi_{mp}(u) &= \frac{1}{\pi} \left\{ \frac{\cos\left(\frac{\pi(m-p)}{2} + \frac{\pi(m+p)u}{2}\right) \sin\left(\frac{\pi(m-p)}{2} - \frac{\pi(m-p)u}{2}\right)}{m-p} \right. \\ &\quad \left. - \frac{\cos\left(\frac{\pi(m+p)}{2} + \frac{\pi(m-p)u}{2}\right) \sin\left(\frac{\pi(m+p)}{2} - \frac{\pi(m+p)u}{2}\right)}{m+p} \right\}; \\ \Phi_{nq}(\bar{u}) &= \frac{1}{\pi} \left\{ \frac{\cos\left(\frac{\pi(n-q)}{2} + \frac{\pi(n+q)\bar{u}}{2}\right) \sin\left(\frac{\pi(n-q)}{2} - \frac{\pi(n-q)\bar{u}}{2}\right)}{n-q} \right. \\ &\quad \left. - \frac{\cos\left(\frac{\pi(n+q)}{2} + \frac{\pi(n-q)\bar{u}}{2}\right) \sin\left(\frac{\pi(n+q)}{2} - \frac{\pi(n+q)\bar{u}}{2}\right)}{n+q} \right\};\end{aligned}\tag{B.8}$$

while, if  $m = p$  and  $n = q$ :

$$\begin{aligned}\Phi_{mp}(u) &= \frac{1}{2\pi m} [\sin(\pi m(u-1)) \cos(-\pi m)] \\ &\quad + \cos(\pi m u) \left( \frac{1-u}{2} \right); \\ \Phi_{nq}(\bar{u}) &= \frac{1}{2\pi n} [\sin(\pi n(\bar{u}-1)) \cos(-\pi n)] \\ &\quad + \cos(\pi n \bar{u}) \left( \frac{1-\bar{u}}{2} \right).\end{aligned}\tag{B.9}$$

However, it was found, that, at low frequencies, the fluid loading has a very small influence on sound radiated by a CLT plate, and it is almost negligible in the mid-high frequency range. Although CLT panels are lightweight elements compared to the traditional building partitions, their inertia is still several orders of magnitude larger than the one provided by the air, thus the load of the fluid does not affect significantly the plate dynamics. The radiation indices compute either considering and neglecting the this effect are

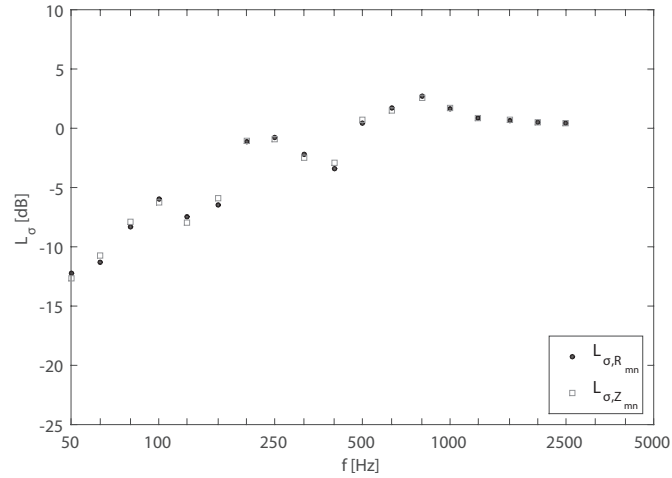


Figure B.3: Comparison between the CLT plate average radiation efficiency computed considering the radiation impedance coefficients  $Z_{mnpq}$  and its approximation with the self radiation resistance coefficients  $R_{mn}$ . Plate mechanically excited in the position  $S_1$ . Results given in one-third octave bands.

compared in one-third octave bands in Figures Figure B.3, Figure B.4 and Figure B.5, for two different position of the mechanical force and for airborne excitation respectively. Furthermore, for a more accurate investigation, the same results are compared in narrow band for each of the external source considered. When the plate is mechanically excited, above 100 Hz the influence of fluid loading is still negligible, as shown in Figures B.6 and B.7. However, at lower frequency some discrepancies can be seen; although, the influence of the fluid loading is very small. On the other hand with airborne excitation, the contribution given by the load of fluid is negligible within the entire frequency range, as shown in Figure B.8.

The radiation impedance  $Z_{mnpq}$  of CLT building structures can be definitely well approximated by the self radiation resistance  $R_{mnmn}$ . This approximation, which does not have a significant influence on the average radiation efficiency, allows to reduce the computational cost to approximately only 1.5 – 2% of the time. This huge difference is related to the computation effort that is required to evaluate the radiation impedance matrix, due to the large dimensions of the panel and to the number of modes that one should consider to extend the analysis up to reasonably high frequencies.

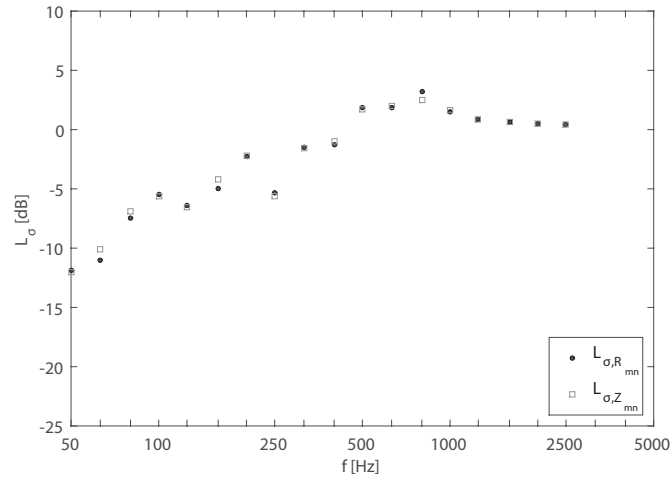


Figure B.4: Comparison between the CLT plate average radiation efficiency computed considering the radiation impedance coefficients  $Z_{mnpq}$  and its approximation with the self radiation resistance coefficients  $R_{mn}$ . Plate mechanically excited in the position  $S_2$ . Results given in one-third octave bands.

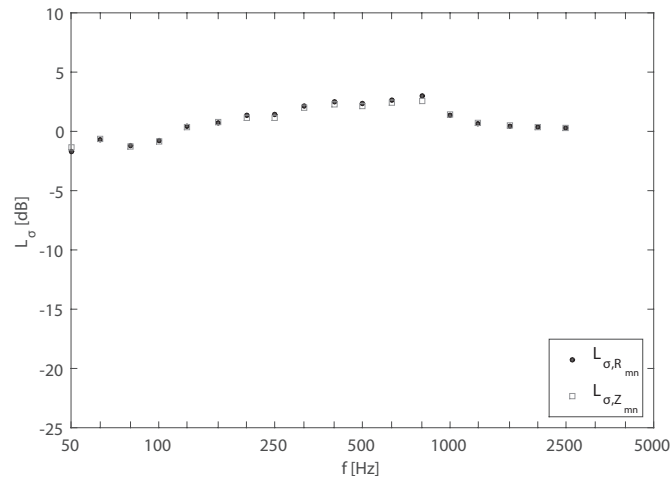


Figure B.5: Comparison between the CLT plate average radiation efficiency computed considering the radiation impedance coefficients  $Z_{mnpq}$  and its approximation with the self radiation resistance coefficients  $R_{mn}$ . Diffuse sound field excitation. Results given in one-third octave bands.

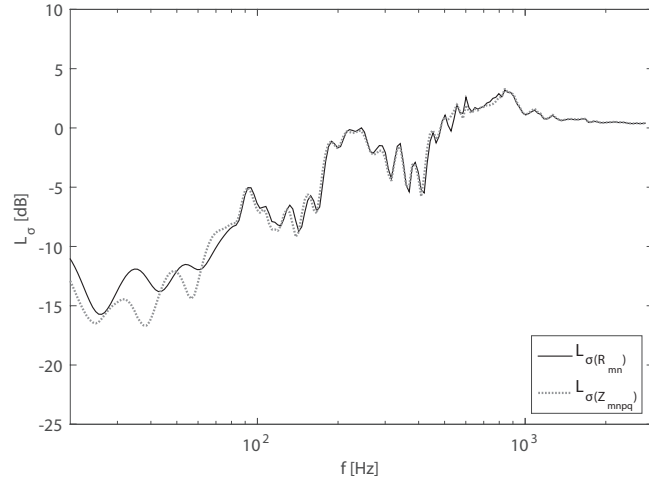


Figure B.6: Comparison between the CLT plate average radiation efficiency computed considering the radiation impedance coefficients  $Z_{mnpq}$  and its approximation with the self radiation resistance coefficients  $R_{mn}$ . Plate mechanically excited in the position  $S_1$ . Results given in narrow band.

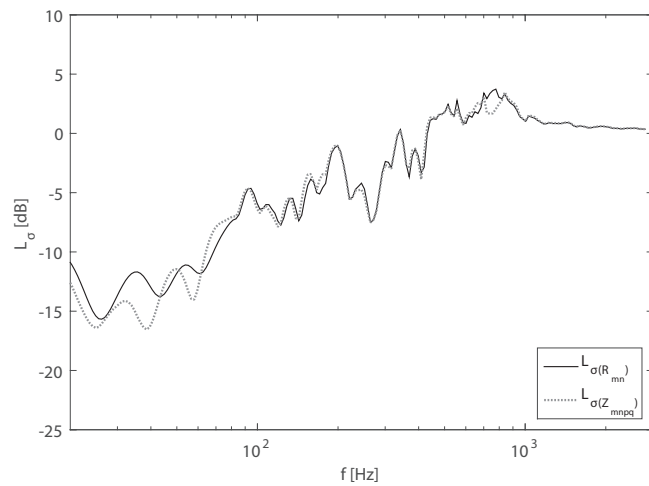


Figure B.7: Comparison between the CLT plate average radiation efficiency computed considering the radiation impedance coefficients  $Z_{mnpq}$ , and the approximation with the self radiation resistance coefficients  $R_{mn}$ . Plate mechanically excited in the position  $S_2$ . Results given in narrow band.

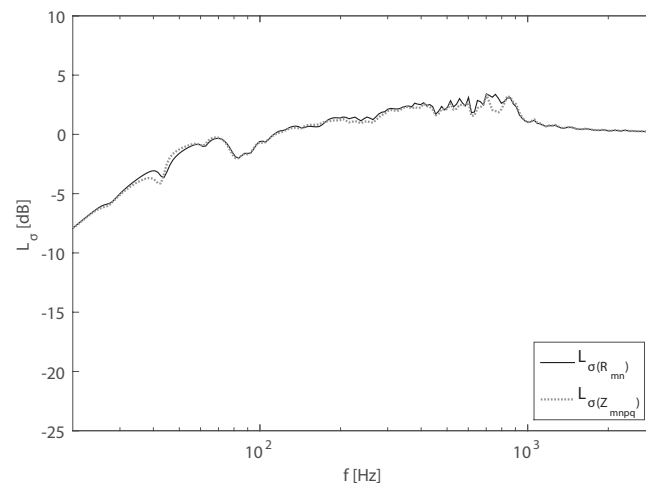


Figure B.8: Comparison between the CLT plate average radiation efficiency computed considering the radiation impedance coefficients  $Z_{mnpq}$ , and the approximation with the self radiation resistance coefficients  $R_{mn}$ . Diffuse sound field excitation. Results given in narrow band.

## Appendix C

# Leppington's asymptotic equations

The modal-average radiation efficiency is computed for each propagation angle by using Leppington's asymptotic equations:

$$\begin{aligned}\sigma &= (1 - \mu^2)^{-\frac{1}{2}} & \mu < 1 - \delta; \\ \sigma &= \frac{(L_x + L_y)(\mu^2 - 1)^{-\frac{1}{2}}}{\pi k_0 \mu L_x L_y} \left[ \ln \left( \frac{\mu + 1}{\mu - 1} \right) + \frac{2\mu}{\mu^2 - 1} \right] & \mu > 1 + \delta; \\ \sigma &= \mathcal{I}(L_x, L_y, 0) + \mathcal{I}(L_y, L_x, 0) & \mu = 1 \pm \delta;\end{aligned}\tag{C.1}$$

the function  $\mathcal{I}$  is given by:

$$\begin{aligned}\mathcal{I}(l_1, l_2, 0) &= \int_0^{\sec \phi_0} \mathcal{J}(i) \left[ -\phi_0 + i \operatorname{cosec} \phi_0 (\cos \phi_0 - \cos 2\phi_0) - \frac{1}{4} i^2 \sin 2\phi_0 \right] di \\ &+ \int_0^{\sec \phi_0} \mathcal{J}(i) \left[ \operatorname{arcsec} i - (i^2 - 1)^{\frac{1}{2}} + \frac{1}{2} (1 - i)^2 \cot \phi_0 \right] di,\end{aligned}\tag{C.2}$$

defining the function  $\mathcal{J}(i)$  as:

$$\mathcal{J}(i) = \frac{(2k_0 l_1)^{\frac{1}{2}}}{\pi^{\frac{3}{2}}} i^{-\frac{1}{2}} \sin \left( k_0 l_1 (\mu - 1) i - \frac{1}{4} \pi \right) e^{-\bar{\eta} i},\tag{C.3}$$

and the angle  $\phi_0$  as;

$$\phi_0 = \arctan \left( \frac{l_2}{l_1} \right).\tag{C.4}$$

The term  $\bar{\eta}$  can be set to zero in order to consider the undamped condition, or it can take into account the plate loss factor  $\eta$ :

$$\bar{\eta} = \frac{1}{4} k_B l_1 \eta.\tag{C.5}$$

---

In order to compute the modal-average radiation efficiency it is necessary to determine three frequency regions in which the equations (C.1) are valid. In the implemented algorithm the three different regions are not set a priori, instead all the three curves are computed for each investigated propagation direction  $\phi$ . The function defined in the *above-coincidence* range assumes

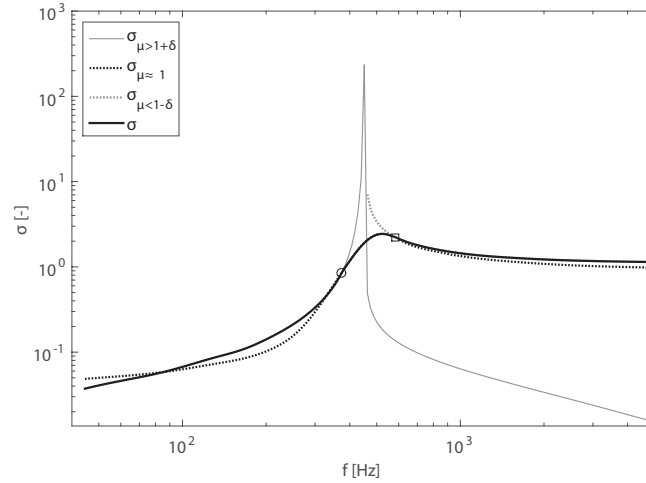


Figure C.1: Determination of the average radiation efficiency for a single propagation direction by combining the curves defined in each frequency region: below-coincidence, near-coincidence, above-coincidence;

negative values below the critical condition while it is positive and it tends asymptotically to unity above. The function defined in the *below-coincidence* region presents a discontinuity at the critical frequency, where  $\mu = 1$ . The first formulation presented by Leppington could not solve this singularity at  $\mu = 1$ , but some years later he proposed an integral formulation for a positive and continuous function valid within an interval around the coincidence frequency, the *near-coincidence* range. The cut off frequency between the *below-coincidence* and *near-coincidence* regions is identified by the intersection between these two functions which is closest to the discontinuity point. Above the coincidence frequency, the first intersection between the *near* and the *above* curves represents the limit between these two regions. It might happen that, due to numerical reasons, two curves do not intersect each other, even though the transition between two regions occurred. In this case the implemented algorithm evaluates the frequency at which the values of the two functions are closest to each other. Once those limits are defined the resulting radiation efficiency is determined, for each investigated angle, by combining the three curves within the frequency range in which they are respectively defined. In Figure C.2 the radiation index, from  $\phi = 0$  to  $\phi = \pi/2$ , is plotted at steps of  $\Delta\phi = \pi/90$ . The radiation

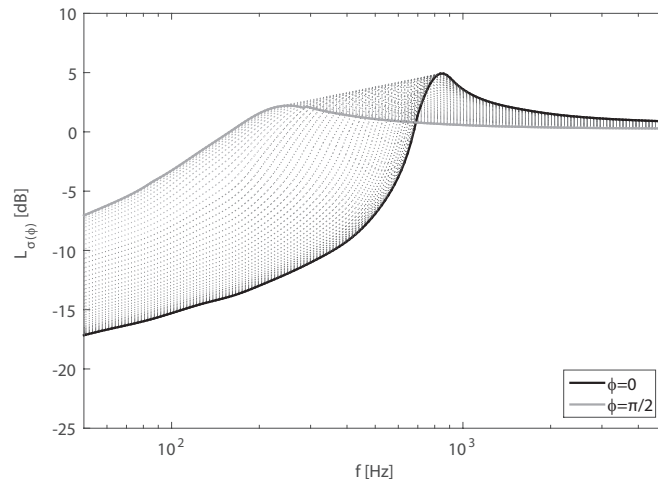


Figure C.2: Frequency dependent average radiation index for different propagation angles  $\phi$ .

efficiency with the lowest critical frequency is associated with the bending wave propagating along the stiffest direction, while the curve with the highest critical frequency is associated with the orthogonal direction. In other words the critical condition is shifted towards lower frequencies as the plate's stiffness increases.



## Appendix D

# Transfer and coupling matrices

In this annex the transfer and the coupling matrices necessary to implement a TMM model of an *ETICS* system are provided. The full derivation for elastic solid, fluid, and poroelastic medium can be found in [133].

### D.1 Fluid medium

The  $[2 \times 2]$  transfer matrix that describe a compressional wave propagating through a fluid medium is defined as:

$$[T_f] = \begin{bmatrix} \cos(k_{x_3} h) & i\omega\rho \sin(k_{x_3} h)k_{x_3}^{-1} \\ ik_{x_3} \sin(k_{x_3} h)(\omega\rho)^{-1} & \cos(k_{x_3} h) \end{bmatrix}, \quad (\text{D.1})$$

where  $h$  is the thickness of the layer and  $k_{x_3}$  is then wavenumber component along the direction  $x_3$ , according to figure Figure 5.1, of the wave propagating in the fluid medium. It is computed as a function of the acoustic wavenumber  $k_0 = \rho_0 c_0$  and the incidence angle  $\theta$  as  $k_{x_3} = \sqrt{k_0^2 - k_0^2 \sin^2 \theta}$ .

### D.2 Solid medium

The  $[4 \times 4]$  transfer matrix that describes the propagation of longitudinal and shear waves through an isotropic elastic solid material, used to model the basic massive wall and the reinforced concrete finishing thin layer of the *ETICS* system, is given by:

$$[T_s] = [\Gamma(-h)] [\Gamma(0)]^{-1}. \quad (\text{D.2})$$

The two wavenumbers components along the  $x_3$ -direction can be calculated as:

$$k_{l,x_3} = \sqrt{k_l^2 - k_t^2}; \quad k_{s,x_3} = \sqrt{k_s^2 - k_t^2}; \quad (\text{D.3})$$

### D.3. Poroelastic medium

---

where  $k_t = k_0 \sin \varphi$  is the trace wavenumber of the incident wave propagating in the fluid, while  $k_l^2$  and  $k_s^2$  are the longitudinal and shear square wavenumbers propagating in the solid medium. They can be derived from the Lamé coefficients  $\lambda$  and  $\mu$  as:

$$k_l^2 = \frac{\omega^2 \rho}{\lambda + 2\mu}; \quad k_s^2 = \frac{\omega^2 \rho}{\mu}. \quad (\text{D.4})$$

The matrix  $\Gamma$  evaluated in  $x_3 = -h$  is:

$$[\Gamma(-h)] = \begin{bmatrix} \omega k_t \cos(-k_{l,x_3} h) & -i\omega k_t \sin(-k_{l,x_3} h) \\ -i\omega k_{l,x_3} \sin(-k_{l,x_3} h) & \omega k_{l,x_3} \cos(-k_{l,x_3} h) \\ -A_1 \cos(-k_{l,x_3} h) & iA_1 \sin(-k_{l,x_3} h) \\ iA_2 k_{l,x_3} \sin(-k_{l,x_3} h) & -A_2 k_{l,x_3} \cos(-k_{l,x_3} h) \end{bmatrix}, \quad (\text{D.5})$$

$$\begin{bmatrix} i\omega k_{s,x_3} \sin(-k_{s,x_3} h) & -\omega k_{s,x_3} \cos(-k_{s,x_3} h) \\ \omega k_t \cos(-k_{s,x_3} h) & -i\omega k_t \sin(-k_{s,x_3} h) \\ iA_2 k_{s,x_3} \sin(-k_{s,x_3} h) & -A_2 k_{s,x_3} \cos(-k_{s,x_3} h) \\ A_1 \cos(-k_{s,x_3} h) & -iA_1 \sin(-k_{s,x_3} h) \end{bmatrix}$$

where the coefficients  $A_1$  and  $A_2$  are defined as:

$$A_1 = \mu \left( k_{l,x_3}^2 - k_0^2 \right); \quad A_2 = 2\mu k_0. \quad (\text{D.6})$$

In order to have a more stable algorithm, the inversion of the matrix  $\Gamma$ , evaluated in  $x_3 = 0$  was analytically computed as:

$$[\Gamma(0)]^{-1} = \begin{bmatrix} 2k_t(\omega k_s^2)^{-1} & 0 \\ 0 & (k_{s,x_3}^2 - k_t^2)(\omega k_{l,x_3} k_s^2)^{-1} \\ 0 & 2k_t(\omega k_s^2)^{-1} \\ (k_{s,x_3}^2 - k_t^2)(\omega k_{s,x_3} k_s^2)^{-1} & 0 \end{bmatrix} \quad (\text{D.7})$$

$$\begin{bmatrix} -(\mu k_s^2)^{-1} & 0 \\ 0 & -k_t(\mu k_{l,x_3} k_s^2)^{-1} \\ 0 & (\mu k_s^2)^{-1} \\ -k_t(\mu k_{s,x_3} k_s^2)^{-1} & 0 \end{bmatrix}$$

### D.3 Poroelastic medium

The poroelastic transfer matrix used to model the mineral wool layer has been derived from Biot's theory [148]. Three kinds of waves are considered propagating in the poroelastic medium: namely a longitudinal and a shear

---

### D.3. Poroelastic medium

---

wave propagating in the solid frame of the material, and a compressional wave propagating in the fluid medium that fills the pores. The  $[6 \times 6]$  poroelastic transfer matrix can be determined as:

$$[T_p] = [\Gamma(-h)] [\Gamma(0)]^{-1}. \quad (\text{D.8})$$

The matrix  $\Gamma$  evaluated in  $x_3$  is defined as:

$$[\Gamma(x_3)] = \begin{bmatrix} \omega k_t \cos(k_{l-s,x_3} x_3) & -i\omega k_t \sin(k_{l-s,x_3} x_3) \\ -i\omega k_{l-s,x_3} \sin(k_{l-s,x_3} x_3) & \omega k_{l-s,x_3} \cos(k_{l-s,x_3} x_3) \\ -i\omega \mu_{l-s} k_{l-s,x_3} \sin(k_{l-s,x_3} x_3) & \omega \mu_{l-s} k_{l-s,x_3} \cos(k_{l-s,x_3} x_3) \\ -D_s \cos(k_{l-s,x_3} x_3) & iD_s \sin(k_{l-s,x_3} x_3) \\ 2iGk_t k_{l-s,x_3} \sin(k_{l-s,x_3} x_3) & -2Gk_t k_{l-s,x_3} \cos(k_{l-s,x_3} x_3) \\ -E_s \cos(k_{l-s,x_3} x_3) & iE_s \sin(k_{l-s,x_3} x_3) \end{bmatrix} \cdot \begin{bmatrix} \omega k_t \cos(k_{l-f,x_3} x_3) & -i\omega k_t \sin(k_{l-f,x_3} x_3) \\ -i\omega k_{l-f,x_3} \sin(k_{l-f,x_3} x_3) & \omega k_{l-f,x_3} \cos(k_{l-f,x_3} x_3) \\ -i\omega \mu_{l-f} k_{l-f,x_3} \sin(k_{l-f,x_3} x_3) & \omega \mu_{l-f} k_{l-f,x_3} \cos(k_{l-f,x_3} x_3) \\ -D_f \cos(k_{l-f,x_3} x_3) & iD_f \sin(k_{l-f,x_3} x_3) \\ 2iGk_t k_{l-f,x_3} \sin(k_{l-f,x_3} x_3) & -2Gk_t k_{l-f,x_3} \cos(k_{l-f,x_3} x_3) \\ -E_f \cos(k_{l-f,x_3} x_3) & iE_f \sin(k_{l-f,x_3} x_3) \end{bmatrix}. \quad (\text{D.9})$$

$$\left. \begin{bmatrix} i\omega k_{s-s,x_3} \sin(k_{s-s,x_3} x_3) & -\omega k_{s-s,x_3} \cos(k_{s-s,x_3} x_3) \\ \omega k_t \cos(k_{s-s,x_3} x_3) & -i\omega k_t \sin(k_{s-s,x_3} x_3) \\ \omega \mu_{s-s} k_t \cos(k_{s-s,x_3} x_3) & -i\omega \mu_{s-s} k_t \sin(k_{s-s,x_3} x_3) \\ 2iGk_t k_{s-s,x_3} \sin(k_{s-s,x_3} x_3) & -2Gk_t k_{s-s,x_3} \cos(k_{s-s,x_3} x_3) \\ G(k_{s-s,x_3}^2 - k_t^2) \cos(k_{s-s,x_3} x_3) & -iG(k_{s-s,x_3}^2 - k_t^2) \sin(k_{s-s,x_3} x_3) \\ 0 & 0 \end{bmatrix} \right\}$$

The wavenumbers components of the two compressional waves and the shear wave along the  $x_3$ -direction are computed as:

$$k_{l-s,x_3} = \sqrt{k_{l-s}^2 - k_t^2}; \quad k_{l-f,x_3} = \sqrt{k_{l-f}^2 - k_t^2}; \quad k_{s-s,x_3} = \sqrt{k_{s-s}^2 - k_t^2}; \quad (\text{D.10})$$

where  $k_{l-s}^2$ ,  $k_{l-f}^2$  and  $k_{s-s}^2$  are the square wavenumbers of the three different waves:

$$\begin{aligned} k_{l-s}^2 &= \frac{\omega^2}{2PR - Q^2} (P\tilde{\rho}_{22} + R\tilde{\rho}_{11} - 2Q\tilde{\rho}_{12} - \sqrt{\Delta}); \\ k_{l-f}^2 &= \frac{\omega^2}{2PR - Q^2} (P\tilde{\rho}_{22} + R\tilde{\rho}_{11} - 2Q\tilde{\rho}_{12} + \sqrt{\Delta}); \\ k_{s-s}^2 &= \frac{\omega^2}{G} \left( \frac{\tilde{\rho}_{11}\tilde{\rho}_{22} - \tilde{\rho}_{12}^2}{\tilde{\rho}_{22}} \right); \end{aligned} \quad (\text{D.11})$$

#### D.4. Coupling matrices

---

where  $P, Q$  and  $R$  are Biot's elastic coefficients,  $G$  is the shear modulus of the material. The quantities  $D_m$  and  $E_m$ , where the subscript  $m$  indicates the solid frame  $m = s$ , or the fluid medium  $m = f$ , are given by:

$$\begin{aligned} D_m &= (P + Q\mu_{l,m}) \left( k_t^2 + k_{l,m,x_3}^2 \right) - 2Gk_t^2 \\ E_m &= (R\mu_{l,m} + Q) \left( k_t^2 + k_{l,m,x_3}^2 \right) \end{aligned} \quad (\text{D.12})$$

the term  $\Delta$  in equation D.11 is computed as:

$$\Delta = (P\tilde{\rho}_{22} + R\tilde{\rho}_{11} - 2Q\tilde{\rho}_{12})^2 - 4 \left( PR - Q^2 \right) \left( \tilde{\rho}_{11}\tilde{\rho}_{22} - \tilde{\rho}_{12}^2 \right) \quad (\text{D.13})$$

the parameters  $\tilde{\rho}_{ij}$  depend on the geometrical and mechanical characteristics of the porous material, considering both the rigid frame and the fluid phase. The velocity ratio  $\mu_{w,m}$  of the air velocity to the two longitudinal wave velocity, respectively  $\mu_{l_s}$  and  $\mu_{l_f}$ , and to the shear wave velocity,  $\mu_{s_s}$ , can be expressed as:

$$\begin{aligned} \mu_{w,m} &= \frac{Pk_{w,m}^2 - \omega^2\tilde{\rho}_{11}}{\omega^2\tilde{\rho}_{12} - Qk_{w,m}^2} & w = l; \quad m = s, f; \\ \mu_{w,m} &= -\frac{\tilde{\rho}_{11}}{\tilde{\rho}_{22}} & w = s; \quad m = s; \end{aligned} \quad (\text{D.14})$$

For the complete derivation of the parameters  $\tilde{\rho}_{ij}$  and the coefficients  $P, Q$  and  $R$  as a function of the poroelastic material properties, please refer to one among the various formalisms of Biot's theory that can be found in the literature, see for example Chapter 6 of [133].

## D.4 Coupling matrices

The interface between two layers of different nature is obtain using coupling matrices. In this section the matrices used to couple the differ layers of *ETICS* are provided:

- *fluid-solid*:

$$\begin{aligned} I_{fs} &= \begin{bmatrix} 0 & -1 \\ 1 & 0 \\ 0 & 0 \end{bmatrix}; & J_{fs} &= \begin{bmatrix} 0 & 1 & 0 & 0 \\ 0 & 0 & 1 & 0 \\ 0 & 0 & 0 & 1 \end{bmatrix}; \\ I_{sf} &= J_{fs}; & J_{sf} &= I_{fs}; \end{aligned} \quad (\text{D.15})$$

- *solid-porous*:

$$\begin{aligned}
I_{sp} &= \begin{bmatrix} 1 & 0 & 0 & 0 \\ 0 & 1 & 0 & 0 \\ 0 & 1 & 0 & 0 \\ 0 & 0 & 1 & 0 \\ 0 & 0 & 0 & 1 \end{bmatrix}; & J_{sp} &= \begin{bmatrix} 1 & 0 & 0 & 0 & 0 & 0 \\ 0 & 1 & 0 & 0 & 0 & 0 \\ 0 & 0 & 1 & 0 & 0 & 0 \\ 0 & 0 & 0 & 1 & 0 & 1 \\ 0 & 0 & 0 & 0 & 1 & 0 \end{bmatrix}; & (D.16) \\
I_{ps} &= J_{sp}; & J_{ps} &= I_{sp};
\end{aligned}$$

These represent the coupling matrices used in the models presented in Chapter 5. However, the coupling between any kind of layer can be derived from the interface conditions.

## D.5 *ETICS*: Global transfer matrix

Assuming the multilayer element to be extended by a semi-infinite fluid on both sides, in order to determine its transmission coefficient, the global transfer matrix is expressed as:

$$[D] = \begin{bmatrix} I_{fs} & J_{fs}T_s & [0] & [0] & [0] \\ [0] & I_{sp} & J_{sp}T_p & [0] & [0] \\ [0] & [0] & I_{ps} & J_{ps}T_s & [0] \\ [0] & [0] & [0] & I_{sf} & J_{sf} \\ [0] & [0] & [0] & [0] & [-1 \quad Z_0/\cos\theta] \end{bmatrix} \quad (D.17)$$

The transmission loss of the *ETICS* system, considering only the airborne transmission path, is determined from the matrix (D.17), as described in Chapter 5.

# Bibliography

- [1] D. Hendy, *Noise: A human history of sound and listening*. London, UK: Profile Books, 2013.
- [2] E. E. Agency, “Noise in Europe,” Tech. Rep. No 10/2014, Environmental European Agency, Luxembourg, 2014.
- [3] C. Hurtley, *Night noise guidelines for Europe*. WHO Regional Office Europe, 2009.
- [4] R. H. Lyon and R. G. DeJong, *Theory and application of statistical energy analysis*. Boston, MA, USA: Butterworth-Heinemann, second ed., 1995.
- [5] “EN 12354 – Building acoustics. Estimation of acoustic performance in buildings from the performance of elements.” standard, International Organization for Standardization, Geneva, CH, 2000 - 2009.
- [6] Lord Rayleigh, *The theory of sound*, vol. 2. New York, NY, USA: reprinted by Dover, 1896.
- [7] L. L. Beranek and I. L. Ver, *Noise and vibration control engineering - Principles and applications*. Hoboken, NJ, USA: John Wiley & Sons, Inc., 1992.
- [8] G. Maidanik, “Response of ribbed panels to reverberant acoustic fields,” *The Journal of the Acoustical Society of America*, vol. 34, no. 6, pp. 809–826, 1962.
- [9] R. Keltie and H. Peng, “The effects of modal coupling on the acoustic power radiation from panels,” *Journal of vibration, acoustics, stress, and reliability in design*, vol. 109, no. 1, pp. 48–54, 1987.
- [10] A. Berry, J. L. Guyader, and J. Nicolas, “A general formulation for the sound radiation from rectangular, baffled plates with arbitrary boundary conditions,” *The Journal of the Acoustical Society of America*, vol. 88, no. 6, pp. 2792–2802, 1990.

## Bibliography

---

- [11] H. Davies, “Low frequency random excitation of water-loaded rectangular plates,” *Journal of Sound and Vibration*, vol. 15, no. 1, pp. 107–126, 1971.
- [12] L. D. Pope and R. C. Leibowitz, “Intermodal coupling coefficients for a fluid-loaded rectangular plate,” *The Journal of the Acoustical Society of America*, vol. 56, no. 2, pp. 408–415, 1974.
- [13] B. E. Sandman, “Motion of a three-layered elastic–viscoelastic plate under fluid loading,” *The Journal of the Acoustical Society of America*, vol. 57, no. 5, pp. 1097–1107, 1975.
- [14] E. G. Williams and J. Maynard, “Numerical evaluation of the rayleigh integral for planar radiators using the fft,” *The Journal of the Acoustical Society of America*, vol. 72, no. 6, pp. 2020–2030, 1982.
- [15] N. Atalla and J. Nicolas, “A new tool for predicting rapidly and rigorously the radiation efficiency of plate-like structures,” *The Journal of the Acoustical Society of America*, vol. 95, no. 6, pp. 3369–3378, 1994.
- [16] H. Nelisse, O. Beslin, and J. Nicolas, “A generalized approach for the acoustic radiation from a baffled or unbaffled plate with arbitrary boundary conditions, immersed in a light or heavy fluid,” *Journal of Sound and Vibration*, vol. 211, no. 2, pp. 207–225, 1998.
- [17] O. Foin, J. Nicolas, and N. Atalla, “An efficient tool for predicting the structural acoustic and vibration response of sandwich plates in light or heavy fluid,” *Applied Acoustics*, vol. 57, no. 3, pp. 213–242, 1999.
- [18] O. Foin, *Outils de prédiction numérique pour l’optimisation des stratégies de contrôle du bruit à la source*. PhD thesis, Université de Sherbrooke, Canada, 1999.
- [19] G. Xie, D. Thompson, and C. Jones, “The radiation efficiency of baffled plates and strips,” *Journal of Sound and Vibration*, vol. 280, no. 1, pp. 181–209, 2005.
- [20] D. Rhazi and N. Atalla, “Transfer matrix modeling of the vibroacoustic response of multi-materials structures under mechanical excitation,” *Journal of Sound and Vibration*, vol. 329, no. 13, pp. 2532–2546, 2010.
- [21] J. L. Davy, “The forced radiation efficiency of finite size flat panels that are excited by incident sound,” *The Journal of the Acoustical Society of America*, vol. 126, no. 2, pp. 694–702, 2009.
- [22] J. L. Davy, D. J. Larner, R. R. Wareing, and J. R. Pearse, “The average specific forced radiation wave impedance of a finite rectangular

- panel,” *The Journal of the Acoustical Society of America*, vol. 136, no. 2, pp. 525–536, 2014.
- [23] J. L. Davy, D. J. Larner, R. R. Wareing, and J. R. Pearse, “The acoustic radiation impedance of a rectangular panel,” *Building and Environment*, vol. 92, pp. 743–755, 2015.
- [24] M. Heckl, “Untersuchungen an orthotropen platten,” *Acta Acustica united with Acustica*, vol. 10, no. 2, pp. 109–115, 1960.
- [25] P. Cordonnier-Cloarec, S. Pautin, D. Biron, M. Haddar, and M. Hamdi, “Contribution to the study of sound transmission and radiation of corrugated steel structures,” *Journal of Sound and Vibration*, vol. 157, no. 3, pp. 515–530, 1992.
- [26] R. Langley, J. Smith, and F. Fahy, “Statistical energy analysis of periodically stiffened damped plate structures,” *Journal of Sound and Vibration*, vol. 208, no. 3, pp. 407–426, 1997.
- [27] J. L. Guyader and C. Lesueur, “Acoustic transmission through orthotropic multilayered plates. Part I: vibration modes,” *Journal of Sound and Vibration*, vol. 58, no. 1, pp. 51–68, 1978.
- [28] V. D’Alessandro, G. Petrone, F. Franco, and S. De Rosa, “A review of the vibroacoustics of sandwich panels: Models and experiments,” *Journal of Sandwich Structures and Materials*, vol. 15, no. 5, pp. 541–582, 2013.
- [29] T. Hugin and M. Ohlrich, “Radiation efficiencies of orthotropic plates,” in *Proceedings of International Conference on Noise & Vibration Pre-design and Characterisation Using Energy Methods NOVEM*, (Lyon, France), 2000.
- [30] J. Anderson and M. Bratos-Anderson, “Radiation efficiency of rectangular orthotropic plates,” *Acta acustica united with Acustica*, vol. 91, no. 1, pp. 61–76, 2005.
- [31] A. Mejdji and N. Atalla, “Dynamic and acoustic response of bidirectionally stiffened plates with eccentric stiffeners subject to airborne and structure-borne excitations,” *Journal of Sound and Vibration*, vol. 329, no. 21, pp. 4422–4439, 2010.
- [32] J. Legault, A. Mejdji, and N. Atalla, “Vibro-acoustic response of orthogonally stiffened panels: The effects of finite dimensions,” *Journal of Sound and Vibration*, vol. 330, no. 24, pp. 5928–5948, 2011.
- [33] J. L. Guyader and C. Lesueur, “Acoustic transmission through orthotropic multilayered plates. Part II: transmission loss,” *Journal of Sound and Vibration*, vol. 58, no. 1, pp. 69–86, 1978.



- [34] J. L. Guyader and C. Lesueur, “Transmission of reverberant sound through orthotropic, viscoelastic multilayered plates,” *Journal of Sound and Vibration*, vol. 70, no. 3, pp. 319–332, 1980.
- [35] I. Bosmans, P. Mees, and G. Vermeir, “Structure-borne sound transmission between thin orthotropic plates: analytical solutions,” *Journal of Sound and Vibration*, vol. 191, no. 1, pp. 75–90, 1996.
- [36] R. R. Wareing, J. L. Davy, and J. R. Pearse, “The sound insulation of single leaf finite size rectangular plywood panels with orthotropic frequency dependent bending stiffness,” *The Journal of the Acoustical Society of America*, vol. 139, no. 1, pp. 520–528, 2016.
- [37] H. J. Lin, C. N. Wang, and Y. M. Kuo, “Sound transmission loss across specially orthotropic laminates,” *Applied Acoustics*, vol. 68, no. 10, pp. 1177–1191, 2007.
- [38] Y. M. Kuo, H. J. Lin, and C. N. Wang, “Sound transmission across orthotropic laminates with a 3d model,” *Applied Acoustics*, vol. 69, no. 11, pp. 951–959, 2008.
- [39] V. Hongisto, “Sound insulation of double panels-comparison of existing prediction models,” *Acta Acustica united with Acustica*, vol. 92, no. 1, pp. 61–78, 2006.
- [40] B. H. Sharp, “Prediction methods for the sound transmission of building elements,” *Noise Control Engineering*, vol. 11, no. 2, pp. 53–63, 1978.
- [41] L. Cremer, M. Heckl, and B. A. T. Petersson, *Structure-borne sound*. Berlin Heidelberg: Springer-Verlag, third ed., 2005.
- [42] T. E. Vigran, “Sound transmission in multilayered structures—introducing finite structural connections in the transfer matrix method,” *Applied Acoustics*, vol. 71, no. 1, pp. 39–44, 2010.
- [43] F. Fahy and P. Gardonio, *Sound and Structural Vibration. Radiation, Transmission and Response*. Oxford, UK: Academic Press in an imprinting of Elsevier, second ed., 2007.
- [44] Q. Gu and J. Wang, “Effect of resilient connection on sound transmission loss of metal stud double panel partitions,” *Chinese Journal of Acoustics*, vol. 2, no. 2, pp. 113–126, 1983.
- [45] J. L. Davy, “A model for predicting the sound transmission loss of walls,” in *Proceedings of the Australian Vibration and Noise Conference 1990*, (Melbourne, Australia), pp. 23–27, Institution of Engineers, 1990.

- [46] J. L. Davy, “Predicting the sound transmission loss of cavity walls,” in *Proceedings of Interior Noise Climates: National Conference of Australian Acoustical Society*, (Perth, Australia), pp. 1–16, Australian Acoustical Society, 1990.
- [47] J. L. Davy, “Sound transmission of cavity walls due to structure borne transmission via point and line connections,” *The Journal of the Acoustical Society of America*, vol. 132, no. 2, pp. 814–821, 2012.
- [48] R. Craik and R. Smith, “Sound transmission through lightweight parallel plates. Part II: Structure-borne sound,” *Applied Acoustics*, vol. 61, no. 2, pp. 247–269, 2000.
- [49] K. F. Graff, *Wave motion in elastic solids*. New York, USA: Dover Publications, Inc., 1991.
- [50] R. D. Mindlin, “Influence of rotary inertia and shear on flexural motions of isotropic elastic plates,” *Journal of Applied Mechanics*, vol. 18, no. 1, pp. 31–38, 1951.
- [51] S. S. Rao, *Vibration of continuous systems*. Hoboken, NJ, USA: John Wiley & Sons, Inc., 2007.
- [52] A. Nilsson and B. Liu, *Vibro-acoustics*, vol. 2. Berlin Heidelberg: Science Press, Beijing and Springer-Verlag, 2015.
- [53] S. P. Timoshenko, “X. on the transverse vibrations of bars of uniform cross-section,” *The London, Edinburgh, and Dublin Philosophical Magazine and Journal of Science*, vol. 43, no. 253, pp. 125–131, 1922.
- [54] I. A. Viktorov, *Rayleigh and Lamb waves: physical theory and applications*. New York, USA: Plenum Press, 1967.
- [55] S. Ljunggren, “Airborne sound insulation of thick walls,” *The Journal of the Acoustical Society of America*, vol. 89, no. 5, pp. 2338–2345, 1991.
- [56] C. Hopkins, *Sound insulation*. Oxford, UK: Butterworth-Heinemann, first ed., 2007.
- [57] D. Backström and A. C. Nilsson, “Modelling the vibration of sandwich beams using frequency-dependent parameters,” *Journal of Sound and Vibration*, vol. 300, no. 3, pp. 589–611, 2007.
- [58] A. W. Leissa, “Vibration of plates,” Tech. Rep. NASA SP-160, National Aeronautics and Space Administration, Washington, DC, 1969.
- [59] M. C. Junger and D. Feit, *Sound, structures, and their interaction*, vol. 225. Cambridge, MA, USA: MIT Press, 1986.

- [60] F. Fahy and P. Gardonio, *Sound and Structural Vibration—Radiation, Transmission and Response*. Oxford, UK: Academic Press in an imprinting of Elsevier, second ed., 2007.
- [61] J. Villar Venini, “Vibroacoustic modelling of orthotropic plates,” Master’s thesis, Politecnico di Milano, Italy, 2011.
- [62] H. Goldstein, C. Poole, and J. Safko, *Classical mechanics*. Boston, MA, USA: Addison-Wesley, third ed., 2002.
- [63] R. Szilard, *Theories and applications of plate analysis: classical numerical and engineering methods*. Hoboken, NJ, USA: John Wiley & Sons, Inc., 2004.
- [64] A. Nilsson and B. Liu, *Vibro-acoustics*, vol. 1. Berlin Heidelberg: Science Press, Beijing and Springer-Verlag, 2015.
- [65] N. Atalla and F. Sgard, *Finite Element and Boundary Methods in Structural Acoustics and Vibration*. Boca Raton, FL, USA: CRC Press, 2015.
- [66] A. D. Pierce, *Acoustics: an introduction to its principles and applications*. Woodbury, NY, USA: Acoustical Society of America, 1989.
- [67] A. Berry, “A new formulation for the vibrations and sound radiation of fluid-loaded plates with elastic boundary conditions,” *The Journal of the Acoustical Society of America*, vol. 96, no. 2, pp. 889–901, 1994.
- [68] O. Beslin and J. Nicolas, “A hierarchical functions set for predicting very high order plate bending modes with any boundary conditions,” *Journal of Sound and Vibration*, vol. 202, no. 5, pp. 633–655, 1997.
- [69] H. Nelisse, O. Beslin, and J. Nicolas, “Fluid–structure coupling for an unbaffled elastic panel immersed in a diffuse field,” *Journal of Sound and Vibration*, vol. 198, no. 4, pp. 485–506, 1996.
- [70] J. L. Guyader, “Sound radiation from structures and their response,” in *Handbook of noise and vibration control* (M. J. Crocker, ed.), ch. 6, pp. 79–98, Hoboken, NJ, USA: John Wiley & Sons, 2007.
- [71] G. Maidanik and E. Kerwin Jr, “Influence of fluid loading on the radiation from infinite plates below the critical frequency,” *The Journal of the Acoustical Society of America*, vol. 40, no. 5, pp. 1034–1038, 1966.
- [72] N. Lomas and S. Hayek, “Vibration and acoustic radiation of elastically supported rectangular plates,” *Journal of Sound and Vibration*, vol. 52, no. 1, pp. 1–25, 1977.

## Bibliography

---

- [73] D. Innes and D. Crighton, “Power radiated by an infinite plate subject to fluid loading and line drive,” *Journal of Sound and Vibration*, vol. 123, no. 3, pp. 437–450, 1988.
- [74] E. Magliula and J. G. McDaniel, “Flexural wave dispersion in orthotropic plates with heavy fluid loading,” *The Journal of the Acoustical Society of America*, vol. 123, no. 5, pp. EL116–EL120, 2008.
- [75] D. Crighton, “The 1988 rayleigh medal lecture: fluid loading—the interaction between sound and vibration,” *Journal of Sound and Vibration*, vol. 133, no. 1, pp. 1–27, 1989.
- [76] C. E. Wallace, “Radiation resistance of a rectangular panel,” *The Journal of the Acoustical Society of America*, vol. 51, no. 3B, pp. 946–952, 1972.
- [77] F. G. Leppington, E. G. Broadbent, and K. H. Heron, “The acoustic radiation efficiency of rectangular panels,” in *Proceedings of the Royal Society of London A: Mathematical, Physical and Engineering Sciences*, vol. 382, pp. 245–271, The Royal Society, 1982.
- [78] M. P. Norton and D. G. Karczub, *Fundamentals of noise and vibration analysis for engineers*. Cambridge, UK: Cambridge university press, 2003.
- [79] S. Ghinet and N. Atalla, “Vibro-acoustic behaviour of multi-layer orthotropic panels,” *Canadian Acoustics*, vol. 30, no. 3, pp. 72–73, 2002.
- [80] I. L. Bosmans, *Analytical modelling of structure-borne sound transmission and modal interaction at complex plate junctions*. PhD thesis, Katholieke Universiteit Leuven, Belgium, 1998.
- [81] R. Langley, “The modal density of anisotropic structural components,” *The Journal of the Acoustical Society of America*, vol. 99, no. 6, pp. 3481–3487, 1996.
- [82] F. G. Leppington, K. H. Heron, E. G. Broadbent, and S. M. Mead, “Resonant and non-resonant acoustic properties of elastic panels. I. The radiation problem,” in *Proceedings of the Royal Society of London A: Mathematical, Physical and Engineering Sciences*, vol. 406, pp. 139–171, The Royal Society, 1986.
- [83] E. Piana, P. Milani, and N. Granzotto, “Simple method to determine the transmission loss of gypsum panels,” in *Proceedings of the 21<sup>st</sup> International Congress on Sound and Vibration Proceedings*, vol. 21, (Beijing, China), International Institute of Acoustics and Vibration, 2015.

- [84] H. Sato, “On the mechanism of outdoor noise transmission through walls and windows—a modification of infinite wall theory with respect to radiation of transmitted wave,” *Journal of the Acoustical Society of Japan*, vol. 29, no. 9, pp. 509–516, 1973.
- [85] E. Sewell, “Transmission of reverberant sound through a single-leaf partition surrounded by an infinite rigid baffle,” *Journal of Sound and Vibration*, vol. 12, no. 1, pp. 21–32, 1970.
- [86] M. Villot, C. Guigou, and L. Gagliardini, “Predicting the acoustical radiation of finite size multi-layered structures by applying spatial windowing on infinite structures,” *Journal of Sound and Vibration*, vol. 245, no. 3, pp. 433–455, 2001.
- [87] T. E. Vigran, “Predicting the sound reduction index of finite size specimen by a simplified spatial windowing technique,” *Journal of Sound and Vibration*, vol. 325, no. 3, pp. 507–512, 2009.
- [88] D. Rhazi and N. Atalla, “A simple method to account for size effects in the transfer matrix method,” *The Journal of the Acoustical Society of America*, vol. 127, no. 2, pp. EL30–EL36, 2010.
- [89] P. Bonfiglio, F. Pompoli, and R. Lioni, “A reduced-order integral formulation to account for the finite size effect of isotropic square panels using the transfer matrix method,” *The Journal of the Acoustical Society of America*, vol. 139, no. 4, pp. 1773–1783, 2016.
- [90] J. L. Davy, J. P. Mahn, C. Guigou-Carter, and M. Villot, “The prediction of flanking sound transmission below the critical frequency,” *The Journal of the Acoustical Society of America*, vol. 132, no. 4, pp. 2359–2370, 2012.
- [91] S. Ghinet and N. Atalla, “Sound transmission loss of insulating complex structures,” *Canadian Acoustics*, vol. 29, no. 3, pp. 26–27, 2001.
- [92] “EN ISO 16351 – Timber structures. Cross laminated timber. Requirements,” standard, International Organization for Standardization, Geneva, CH, 2015.
- [93] E. Karacebeyli and B. Douglas, *CLT Handbook - US edition*. Pointe-Claire, Quebec, Canada: FPInnovations, 2013.
- [94] R. Öqvist, F. Ljunggren, and A. Ågren, “Variations in sound insulation in cross laminated timber housing construction,” in *Proceedings of Forum Acusticum 2011*, (Aalborg, Denmark), EAA, June 2011.
- [95] S. Schoenwald, B. Zeitler, I. Sabourin, and F. King, “Sound insulation performance of cross laminated timber building systems,” in

- Proceedings of the 42<sup>nd</sup> International Congress and Exposition on Noise Control Engineering*, (Innsbruck, Austria), Institute of Noise Control Engineering, September 2013.
- [96] B. Van Damme, S. Schoenwald, M. Alvarez Blanco, and A. Zemp, “Limitation to the use of homogenized material parameters of cross laminated timber plates for vibration and sound transmission modelling,” in *Proceedings of the 22<sup>nd</sup> International Congress on Sound and Vibration*, (Florence, Italy), International Institute of Acoustics and Vibration, July 2015.
- [97] A. Santoni and P. Fausti, “Case studies on the application of EN 12354-5 in Italy,” in *Proceedings of the 42<sup>nd</sup> International Congress and Exposition on Noise Control Engineering*, vol. 247, (Innsbruck, Austria), pp. 6211–6220, Institute of Noise Control Engineering, 2013.
- [98] P. Niemz and D. Mannes, “Non-destructive testing of wood and wood-based materials,” *Journal of Cultural Heritage*, vol. 13, no. 3, pp. S26–S34, 2012.
- [99] P. S. Frederiksen, “Experimental procedure and results for the identification of elastic constants of thick orthotropic plates,” *Journal of Composite Materials*, vol. 31, no. 4, pp. 360–382, 1997.
- [100] E. O. Ayorinde and L. Yu, “On the elastic characterization of composite plates with vibration data,” *Journal of Sound and Vibration*, vol. 283, no. 1, pp. 243–262, 2005.
- [101] V. Bucur and R. Archer, “Elastic constants for wood by an ultrasonic method,” *Wood Science and Technology*, vol. 18, no. 4, pp. 255–265, 1984.
- [102] D. Keunecke, W. Sonderegger, K. Pereteanu, T. Lüthi, and P. Niemz, “Determination of Young’s and shear moduli of common yew and Norway spruce by means of ultrasonic waves,” *Wood science and technology*, vol. 41, no. 4, pp. 309–327, 2007.
- [103] U. Dackermann, R. Elsener, J. Li, and K. Crews, “A comparative study of using static and ultrasonic material testing methods to determine the anisotropic material properties of wood,” *Construction and Building Materials*, vol. 102, pp. 963–976, 2016.
- [104] P. Bonfiglio and F. Pompoli, “Determination of the dynamic complex modulus of viscoelastic materials using a time domain approach,” *Polymer Testing*, vol. 48, pp. 89–96, 2015.

## Bibliography

---

- [105] J. Rindel, “Dispersion and absorption of structure-borne sound in acoustically thick plates,” *Applied Acoustics*, vol. 41, no. 2, pp. 97–111, 1994.
- [106] T. Nightingale, R. Halliwell, and G. Pernica, “Estimating in-situ material properties of a wood joist floor: Part 1-measurements of the real part of bending wavenumber and modulus of elasticity,” *Building Acoustics*, vol. 11, no. 3, pp. 1–27, 2004.
- [107] N. Clark and S. Thwaites, “Local phase velocity measurements in plates,” *Journal of Sound and Vibration*, vol. 187, no. 2, pp. 241–252, 1995.
- [108] S. Thwaites and N. Clark, “Non-destructive testing of honeycomb sandwich structures using elastic waves,” *Journal of Sound and Vibration*, vol. 187, no. 2, pp. 253–269, 1995.
- [109] “EN ISO 3382-2 – Acoustics: Measurement of room acoustic parameters –Part 2: Reverberation time in ordinary rooms,” standard, International Organization for Standardization, Geneva, CH, 2008.
- [110] “EN ISO 10140-5 – Acoustics: laboratory measurement of sound insulation of building elements–Part 5: requirements for test facilities and equipment,” standard, International Organization for Standardization, Geneva, CH, 2010.
- [111] N. Hashimoto, “Measurement of sound radiation efficiency by the discrete calculation method,” *Applied Acoustics*, vol. 62, no. 4, pp. 429–446, 2001.
- [112] “EN ISO 10848-1 – Acoustics: Laboratory Measurement of the flanking transmission of airborne and impact sound between adjoining rooms. Part 1: Frame Document,” standard, International Organization for Standardization, Geneva, CH, 2006.
- [113] A. Prato and A. Schiavi, “Sound insulation of building elements at low frequency: A modal approach,” *Energy Procedia*, vol. 78, pp. 128–133, 2015.
- [114] D. Gsell, G. Feltrin, S. Schubert, R. Steiger, and M. Motavalli, “Cross-laminated timber plates: evaluation and verification of homogenized elastic properties,” *Journal of Structural Engineering*, vol. 133, no. 1, pp. 132–138, 2007.
- [115] M. E. McIntyre and J. Woodhouse, “On measuring the elastic and damping constants of orthotropic sheet materials,” *Acta Metallurgica*, vol. 36, no. 6, pp. 1397–1416, 1988.

- [116] I. Roelens, F. Nuytten, I. Bosmans, and G. Vermeir, “In situ measurement of the stiffness properties of building components,” *Applied Acoustics*, vol. 52, no. 3, pp. 289–309, 1997.
- [117] J. Chung, T. Chung, and K. Kim, “Vibration analysis of orthotropic mindlin plates with edges elastically restrained against rotation,” *Journal of Sound and Vibration*, vol. 163, no. 1, pp. 151–163, 1993.
- [118] E. Nilsson and A. Nilsson, “Prediction and measurement of some dynamic properties of sandwich structures with honeycomb and foam cores,” *Journal of Sound and Vibration*, vol. 251, no. 3, pp. 409–430, 2002.
- [119] B. Van Damme, S. Schoenwald, and A. Zemp, “Modeling the bending vibration of cross-laminated timber beams,” *European Journal of Wood and Wood Products*, p. forthcoming, 2017.
- [120] J. Bodig and B. A. Jayne, *Mechanics of Wood and Wood Composites*. New York, USA: Van Nostrand Reinhold Company, 1982.
- [121] T. Pritz, “Frequency dependences of complex moduli and complex poisson’s ratio of real solid materials,” *Journal of Sound and Vibration*, vol. 214, no. 1, pp. 83–104, 1998.
- [122] D. Bies and S. Hamid, “In situ determination of loss and coupling loss factors by the power injection method,” *Journal of Sound and Vibration*, vol. 70, no. 2, pp. 187–204, 1980.
- [123] M. Carfagni and M. Pierini, “Determining the loss factor by the power input method (pim), part 1: numerical investigation,” *Journal of vibration and acoustics*, vol. 121, no. 3, pp. 417–421, 1999.
- [124] M. Carfagni and M. Pierini, “Determining the loss factor by the power input method (pim), part 2: experimental investigation with impact hammer excitation,” *Journal of vibration and acoustics*, vol. 121, no. 3, pp. 422–428, 1999.
- [125] B. C. Bloss and M. D. Rao, “Estimation of frequency-averaged loss factors by the power injection and the impulse response decay methods,” *The Journal of the Acoustical Society of America*, vol. 117, no. 1, pp. 240–249, 2005.
- [126] J. G. Richter, B. Zeitler, I. Sabourin, and S. Schoenwald, “Comparison of different methods to measure structural damping,” *Canadian Acoustics*, vol. 39, no. 3, pp. 54–55, 2011.
- [127] R. Cherif and N. Atalla, “Experimental investigation of the accuracy of a vibroacoustic model for sandwich-composite panels,” *The Journal*



- of the Acoustical Society of America*, vol. 137, no. 3, pp. 1541–1550, 2015.
- [128] M. Gomperts, “Radiation from rigid baffled, rectangular plates with general boundary conditions,” *Acta Acustica united with Acustica*, vol. 30, no. 6, pp. 320–327, 1974.
- [129] M. Gomperts, “Sound radiation from baffled, thin, rectangular plates,” *Acta Acustica united with Acustica*, vol. 37, no. 2, pp. 93–102, 1977.
- [130] F. Leppington, E. Broadbent, and K. Heron, “Acoustic radiation from rectangular panels with constrained edges,” in *Proceedings of the Royal Society of London A: Mathematical, Physical and Engineering Sciences*, vol. 393, pp. 67–84, The Royal Society, 1984.
- [131] G. Squicciarini, D. Thompson, and R. Corradi, “The effect of different combinations of boundary conditions on the average radiation efficiency of rectangular plates,” *Journal of Sound and Vibration*, vol. 333, no. 17, pp. 3931–3948, 2014.
- [132] M. Munjal, “Response of a multi-layered infinite plate to an oblique plane wave by means of transfer matrices,” *Journal of Sound and Vibration*, vol. 162, no. 2, pp. 333–343, 1993.
- [133] J. Allard and N. Atalla, *Propagation of sound in porous media: modelling sound absorbing materials*. Chichester, UK: John Wiley & Sons, Ltd, 2 ed., 2009.
- [134] L. Parati, B. P. Farbood, and M. Borghi, “May retrofit also include acoustics aspects?,” *Energy Procedia*, vol. 78, pp. 158–163, 2015.
- [135] L. Weber and D. Brandstetter, “Einheitliche schalltechnische Bemessung von Wärmedämm-Verbundsystemen (IBP-Bericht B-BA 6/2002),” tech. rep., Fraunhofer Institut für Bauphysik, Fraunhofer IRB-Verlag, Stuttgart, Germany, 2004.
- [136] N. Atalla, “Modeling the sound transmission through complex structures with attached noise control materials,” *Wave Motion*, vol. 51, no. 4, pp. 650–663, 2014.
- [137] “EN ISO 10140-2 – Acoustics: Laboratory measurement of sound insulation of building elements – Part 2: Measurement of airborne sound insulation,” standard, International Organization for Standardization, Geneva, CH, 2010.
- [138] W. Maysenhölder and R. Haberkern, “Sound transmission through periodically inhomogeneous plates: Solution of the general problem by a variational formulation,” *Acta Acustica united with Acustica*, vol. 89, no. 2, pp. 323–332, 2003.

- [139] A. Dijckmans, *Wave Based Calculation Methods for Sound-Structure Interaction. Application to Sound Insulation and Sound Radiation of Composite Walls and Floors*. PhD thesis, Katholieke Universiteit Leuven, Belgium, 2011.
- [140] G. Jacques, S. Berger, V. Gibiat, P. Jean, M. Villot, and S. Ciukaj, “A homogenised vibratory model for predicting the acoustic properties of hollow brick walls,” *Journal of Sound and Vibration*, vol. 330, no. 14, pp. 3400–3409, 2011.
- [141] J. D’Errico, “fminsearchbnd.” <https://it.mathworks.com/matlabcentral/fileexchange/8277-fminsearchbnd--fminsearchcon/>, 2005 (Retrieved February 6, 2012).
- [142] P. Bonfiglio and F. Pompoli, “Inversion problems for determining physical parameters of porous materials: Overview and comparison between different methods,” *Acta Acustica united with Acustica*, vol. 99, no. 3, pp. 341–351, 2013.
- [143] P. Bonfiglio, F. Pompoli, and P. Shrivage, “Quasi-static evaluation of mechanical properties of poroelastic materials: static and dynamic strain dependence and in vacuum tests,” in *Proceeding of the 10<sup>th</sup> European Congress and Exposition on Noise Control Engineering*, (Paris,France), EAA-ASA-SFA, 2008.
- [144] “ISO 9614-3 –Acoustics – Determination of sound power levels of noise sources using sound intensity–Part 3: Precision method for measurement by scanning,” standard, International Organization for Standardization, Geneva, CH, 2002.
- [145] T. E. Vigran, “Sound insulation of double-leaf walls–allowing for studs of finite stiffness in a transfer matrix scheme,” *Applied Acoustics*, vol. 71, no. 7, pp. 616–621, 2010.
- [146] R. Halliwell, T. Nightingale, A. Warnock, and J. Birta, “Gypsum board walls: Transmission loss data,” *National Research Council of Canada, Internal Report No.*, vol. 761, 1998.
- [147] J. Poblet-Puig, A. Rodríguez-Ferran, C. Guigou-Carter, and M. Villot, “The role of studs in the sound transmission of double walls,” *Acta Acustica united with Acustica*, vol. 95, no. 3, pp. 555–567, 2009.
- [148] M. Biot, “Generalized theory of acoustic propagation in porous dissipative media,” *The Journal of the Acoustical Society of America*, vol. 34, no. 9A, pp. 1254–1264, 1962.

# Acknowledgements

Finally, I would like to spend some words to thank all the people that supported me during this intense and stimulating period that, after three years, is about to end.

I would first like to express my sincere gratitude to my advisor Patrizio Fausti, who constantly supported my research, gave me a total freedom in developing my ideas and has always been open to interesting and inspiring talks. I would also like to thank Stefan Schoenwald, for inviting me at Empa, and being an outstanding mentor to me.

During the visiting time at *Empa – Swiss Federal Laboratories for Material Science and Technology; Laboratory for Acoustics/Noise Control in Dübendorf* – I had the chance to perform all the experimental measurements on cross-laminated structures and develop most of the models on sound radiation for orthotropic structures presented in this dissertation. Nine months spent in Switzerland, have been a period of intense but relaxed learning, also thanks to all the colleagues of the Acoustics and Noise Control Laboratory that made me feel very welcome. This period would have certainly been more solitary without Bart Van Damme whom I want to further thank for his priceless advices and for his patience in reading and commenting my thesis.

The final version of this thesis has been improved from its early stage also thanks to the valuable comments of other two referees, Ulrich Schanda and John Davy. Moreover, I would like to acknowledge the helpful collaboration with John that made me realise that I was just scratching the surface of some important concepts and pushed me to go into more depth with my study.

During these three years, I spent the largest amount of time at the Engineering Department of the University of Ferrara. Most of the activities have been undertaken within the Acoustic Research Group, where I found a lot of nice people willing to help and encourage me; thanks to Professor Pompoli, Andrea, Francesco and Nicola. Special thanks go to Paolo who, from the very beginning, stimulated my curiosity in different fields of acoustics and gave me precious advices. Within this nice research group I have also found a bunch of friends, who certainly made the office environment more enjoyable; so thank you Chiara, Cristina, Carmen and Nicolò.

My deep and sincere gratitude to my parents, Piero and Maria Assunta, and my brother Mattia, for their unconditional support. Thanks to Mauro

---

and Loretta and all the people that I might have forgotten and that will definitely pop in my mind as soon as I will look at the printed manuscript. A big hug to all my friends that somehow managed to let me live a very pleasant life.

The last but foremost thought is for Martina, the wonderful person I am so lucky to share my life with, thank you for everything.

# Andrea Santoni

## Curriculum Vitae

Engineering Department  
University of Ferrara  
☎ +39 349 6006379  
✉ andrea.santoni@unife.it



---

### Personal Information

*Date of Birth* 28<sup>th</sup> of February 1986  
*Place of Birth* Rimini (Italy)  
*Nationality* Italian

---

### Education

- 2014 - present **PhD Student**, *Engineering Department*, University of Ferrara.  
Thesis Title: *Sound Radiation and Sound Transmission in Building Structures: Numerical Modelling and Experimental Validation*  
Supervisor: Prof. P. Fausti  
Co-advisor: Prof. S. Schoenwald  
Scientific Sector: ING-IND/11
- 2009–2013 **Master's degree in Civil Engineering**, *University of Ferrara*, grade 108/110,  
Thesis Title: *Structure-borne sound: Metodologie di caratterizzazione delle sorgenti sonore strutturali e implementazione dei modelli UNI EN 12354 alle tipologie edilizie italiane.*  
Supervisor: Prof. P. Fausti
- 2005–2008 **Bachelor's degree in Architectural and Building Science Technology**, *University of Bologna*, grade 105/110, Thesis Title: *Evoluzione delle tecniche di misura dell'acustica architettonica. "Casa della musica di San Marino".*  
Supervisor: Prof. L. Tronchin
- 2005 **Secondary school diploma**, *Scientific Lyceum Marie Curie.*

---

### Qualification and Specialization Courses

- 2016 **Symposium on building acoustics**, *Towards a better understanding: ratings and predictions.*
- 2016 **3D Virtual Acoustics**, *EAA - Summer school in acoustics.*
- 2016 **Numerical methods in acoustics**, *EAA - Summer school in acoustics.*
- 2016 **Smart structures for vibro-acoustic control**, *CISM - Marie Curie Graduated School.*
- 2014 **Best engineering training in electric, lightweight and quiet driving**, *eLiquid - Marie Curie Public Technical course.*
- 2009 **Energy performance of buildings**, *Region: "Emilia Romagna".*

---

## Relevant Work & Research Experience

- May–Dec. 2015 **ACADEMIC GUEST (as PhD student)**, *Laboratory for Acoustics/Noise Control*, EMPA - Swiss Federal Laboratories for Material Science and Technology.  
Occupational skills:
  - experimental and numerical evaluation of the sound power radiated from CLT plates and material characterisation.
- Aug.–Dec. 2013 **POST-GRAD INTERNSHIP**, *Engineering Department*, University of Ferrara.  
Occupational skills:
  - environmental acoustic monitoring of noise emissions related to the MOse construction activities in the lagoon of Venice.
- 2009–2013 **JUNIOR ENGINEER**, *Studio Tecnico Massari*, [www.studiotecnicomassari.it](http://www.studiotecnicomassari.it).  
Occupational skills:
  - Building and environmental acoustics: experimental in-field measurements and numerical simulations.

---

## Conference and Seminar Presentations

- 2017 **AIA Symposium**, *Bolzen, Italy*, International Symposium on Advanced Research in Timber Construction: Acoustics Quality, Environment and Safety.  
Presentation title: *Sound radiation model for CLT plates*
- 2016 **Rothschool**, *Bolzen, Italy*, Corso per l'Ordine degli Ingegneri di Bolzano, La progettazione acustica di edifici con struttura in legno: Modelli teorici e applicazioni costruttive.  
Presentation title: *Proprietà acustiche dei materiali lignei da costruzioni innovativi*.
- 2016 **INTERNOISE**, *International Congress*, Hamburg, Germany.  
Presentation title: *Sound radiation efficiency measurements on cross laminated timber plates*.
- 2016 **EUROREGIO**, *International Congress*, Porto, Portugal.  
Presentation title: *Average sound radiation model for orthotropic cross laminated timber plates*.
- 2015 **EURONOISE**, *International Congress*, Maastricht, Netherlands.  
Presentation title: *Sound insulation of heavyweight walls with linings and additional layers: Numerical investigation*.
- 2014 **FORUM ACUSTICUM**, *International Congress*, Krakow, Poland.  
Presentation title: *Field measurements to analyse flanking transmission in buildings*.
- 2014 **AIA NATIONAL CONGRESS**, *National Congress*, Florence, Italy.  
Presentation title: *Analisi della trasmissione strutturale attraverso misurazioni in opera*.
- 2013 **INTERNOISE**, *International Congress*, Innsbruck, Austria.  
Presentation title: *Case studies on the application of EN 12354-5 in Italy*.

---

## Tutoring Activity

- 2014 **University of Ferrara**, *Civil Engineering*.  
Course: *Building and environmental acoustics*
- 2014–2016 **Scuola di Acustica (Acoustics School)**.  
*Tecnico Competente in Acustica Ambientale (TCAA)*

---

## List of Publications

**Santoni, Andrea**, S. Schoenwald, B. Van Damme, and P. Fausti. Determination of the elastic and stiffness characteristics of cross-laminated timber plates from flexural wave velocity measurements. *Journal of Sound and Vibration*, forthcoming, 2017.

**Santoni, Andrea**, P. Bonfiglio, J. L. Davy, P. Fausti, F. Pompoli, and L. Pagnoncelli. Sound transmission loss of *ETICS* cladding systems considering the structure-borne transmission via the mechanical fixings: Numerical prediction model and experimental evaluation. *Applied Acoustics*, 122:88–97, 2017.

P. Fausti, P. Campostrini, C. Dabalà, M. Caniato, M. C. Guerra, **A. Santoni**, and N. Zuccherini Martello. Noise generated from large construction sites: Measurements and possible mitigations. In *Proceedings of the 22<sup>nd</sup> International Congress on Acoustics*, Buenos Aires, Argentina, September 2016. ICA.

**A. Santoni**, S. Schoenwald, B. Van Damme, H. M. Tröbs, and P. Fausti. Average sound radiation model for orthotropic cross laminated timber plates. In *Proceedings of Euroregio 2016*, Porto, Portugal, June 2016. EAA-SPA-SEA.

**A. Santoni**, P. Bonfiglio, P. Fausti, S. Schoenwald, and H. M. Tröbs. Sound radiation efficiency measurements on cross laminated timber plates. In *Proceedings of the 45<sup>th</sup> International Congress and Exposition on Noise Control Engineering*, pages 3697–3707, Hamburg, Germany, 2016. Institute of Noise Control Engineering.

P. Bonfiglio, F. Pompoli, **A. Santoni**, P. Fausti, and L. Pagnoncelli. Indagine sperimentale dell'influenza delle connessioni sulle prestazioni acustiche di sistemi di isolamento a cappotto. In *Atti del 43<sup>o</sup> Convegno Nazionale Associazione Italiana Acustica*, Alghero, Italy, 2016. Associazione Italiana di acustica.

N. Zuccherini Martello, S. Secchi, P. Fausti, G. Cellai, and **A. Santoni**. Analysis of direct and flanking sound transmission between rooms with curtain wall facades. *Energy Procedia*, (78):164–169, 2015.

N. Zuccherini Martello, P. Fausti, **A. Santoni**, and S. Secchi. The use of sound absorbing shading systems for the attenuation of noise on building façades. An experimental investigation. *Buildings*, 5(4):1346–1360, 2015.

N. Zuccherini Martello, P. Fausti, and **A. Santoni**. Experimental analysis of sound absorbing shading systems for the acoustic protection of facades. In *Proceedings of the 22<sup>nd</sup> International Congress on Sound and Vibration Proceedings*, Florence, Italy, 2015. International Institute of Acoustics and Vibration.

**A. Santoni**, P. Bonfiglio, P. Fausti, and N. Zuccherini Martello. Sound insulation of heavyweight walls with linings and additional layers: Numerical investigation. In *Proceeding of the 10<sup>th</sup> European Congress and Exposition on Noise Control Engineering*, Maastricht, Netherlands, 2015. EAA-NAG-ABAV.

S. Secchi, G. Cellai, P. Fausti, **A. Santoni**, and N. Zuccherini Martello. Sound transmission between rooms with curtain wall facades. A case study. *Building Acoustics*, 3-4(22):193–207, 2015.

P. Bonfiglio, F. Pompoli, **A. Santoni**, and C. Marescotti. Determination of dynamic storage modulus of viscoelastic and poroelastic materials using a simplified time of flight approach. In *Proceedings of the 22<sup>nd</sup> International Congress on Sound and Vibration Proceedings*, Florence, Italy, 2015. International Institute of Acoustics and Vibration.

**A. Santoni** and P. Fausti. Field measurements to analyse flanking transmission in buildings. In *Proceedings of Forum Acusticum 2014*, Krakow, Poland, 2014. EAA.

**A. Santoni** and P. Fausti. Analisi della trasmissione strutturale attraverso misurazioni in opera. In *Atti del 41<sup>o</sup> Convegno Nazionale Associazione Italiana Acustica*, Pisa, Italy, 2014. Associazione Italiana di acustica.

S. Secchi, P. Fausti, T. Carrascal Garcia, M. Machimbarrena, C. Monteiro, and **A. Santoni**. How building technology in Italy and Spain can be improved after the experience of COST Action TU0901 and the discussion on going on the new descriptors. In *Proceedings of Forum Acusticum 2014*, Krakow, Poland, 2014.

P. Fausti, T. Carrascal García, B. Ingelaere, M. Machimbarrena, C. Monteiro, B. Rasmussen, **Santoni, A.**, S. Secchi, and S. Smith. e-book: Building acoustics throughout Europe. COST Action TU0901. Volume 1: Towards a common framework in building acoustics throughout Europe. 2014.

E. Baldaccini, P. Campostrini, F. Coccon, C. Dabalà, P. Fausti, **A. Santoni**, and C. Soldatini. Birds and noise: The MOse yards case (Lagoon of Venice, Italy). In *Proceedings of the 5<sup>th</sup> International Symposium: Monitoring of Mediterranean coastal areas: problems and measurements techniques*, pages 807–816, Livorno, Italy, 2014.

**A. Santoni** and P. Fausti. Case studies on the application of EN 12354-5 in Italy. In *Proceedings of the 42<sup>nd</sup> International Congress and Exposition on Noise Control Engineering*, volume 247, pages 6211–6220, Innsbruck, Austria, 2013. Institute of Noise Control Engineering.